From DEPARTMENT OF CLINICAL SCIENCES, DANDERYD HOSPITAL
Karolinska Institutet, Stockholm, Sweden

MAGNETIC RESONANCE IMAGING FOR THE ASSESSMENT OF LIVER FUNCTION

Henrik Nilsson

Karolinska Institutet

Stockholm 2011

Published by Karolinska Institutet.

ISBN 978-91-7457-360-2

Printed by
REPROPRINT AB
Stockholm 2011
www.reproprint.se
Gårdsvägen 4, 169 70 Solna

“Traveller, there is no path.
The path is made by walking”

—Antonio Machado

“There are known knowns; there are things we know we know.
We also know there are known unknowns; that is to say we know there are some things we do not know.
But there are also unknown unknowns – the ones we don't know we don't know.”

—Former United States Secretary of Defence Donald Rumsfeld

ABSTRACT

This thesis presents dynamic hepatocyte-specific contrast-enhanced magnetic resonance imaging (DHCE-MRI) as a new method for total and segmental liver function assessment. The method is based on the hepatocyte-specific properties of Gd-EOB-DTPA, which is actively taken up into functioning hepatocytes. The presence of this substance in a tissue will induce an increase in signal intensity in magnetic resonance imaging (MRI). The underlying hypothesis in this work is that if the liver uptake of Gd-EOB-DTPA could be quantified, this would then reflect liver function. All studies were approved by the Stockholm Regional Ethical Review Board. The first study was performed on 20 healthy volunteers and showed that quantification of tracer uptake and liver perfusion was feasible on a segmental level using deconvolutional analysis (DA). In the second study, quantification of tracer uptake was done in 12 patients with primary biliary cirrhosis (PBC) as well as in the 20 healthy controls examined in the first study. Both quantitative parameters derived from DA and traditional semi-quantitative parameters (C_{max}, t_{max}, $t_{1/2}$) were assessed. There were significant differences in the DA-derived parameters regarding uptake capacity and tracer transfer time between PBC patients and controls, but the traditional semi-quantitative parameters were not able to separate the groups. Furthermore, there was a significant association between established prognostic scoring-models and the quantitative parameters. In the third study the healthy volunteers from the first study were again used as controls, but this time compared to 12 patients with primary sclerosing cholangitis (PSC). Total and segmental liver function as well as volume was assessed using DA-derived quantitative parameters, but no significant differences between the groups were found. A significantly more heterogeneous distribution of liver function was found in the PSC group, and the degree of bile duct stricturing so typical of PSC was found to correlate with the DA-derived liver function parameters. In the fourth study total and segmental liver function was assessed in 10 patients with varying degrees of alcohol- and/or viral-induced cirrhosis, and compared to the controls of the first study. Also in this patient group a significantly more heterogeneous distribution of liver function was found, as well as significant differences between the groups regarding the outcome of the functional parameters. In a simulation of a left hemihepatectomy, the possible implication of this heterogeneous distribution of function on liver resection was assessed, showing how uncertain the prediction of postoperative liver function can be when regional differences in liver function are not accounted for. In a receiver operator characteristic (ROC) analysis, the DHCE-MRI derived parameters showed good to excellent capacity in separating groups with normal or adequate liver function from patients with more severely affected liver parenchyma. In conclusion, DHCE-MRI can be used to assess total and segmental liver volume and function. Functional parameters indicative of parenchymal tracer extraction capacity, liver perfusion and tracer transit times can also be assessed on a global and segmental level. The outcome of these parameters differs significantly between patients with liver cirrhosis and healthy controls, and also correlates with established clinical scoring models. DHCE-MRI is a new and promising tool for total and segmental liver function assessment and deserves further studies.

Key-words: DHCE-MRI, liver function, Gd-EOB-DTPA, deconvolutional analysis

LIST OF PUBLICATIONS

I. Nilsson H, Nordell A, Vargas R, Douglas L, Jonas E, Blomqvist L. Assessment of hepatic extraction fraction and input relative blood flow using dynamic hepatocyte-specific contrast-enhanced MRI. J Magn Reson Imaging. 2009 Jun;29(6):1323-31.

II. Nilsson H, Blomqvist L, Douglas L, Nordell A, Jonas E. Assessment of liver function in primary biliary cirrhosis using Gd-EOB-DTPA-enhanced liver MRI. HPB (Oxford). 2010 Oct;12(8):567-76.

III. Nilsson H, Blomqvist L, Douglas L, Nordell A, Jacobsson H, Hagen K, Bergquist A, Jonas E. Dynamic gadoxetate-enhanced MRI for the assessment of total and segmental liver function and volume in primary sclerosing cholangitis *(submitted manuscript).*

IV. Nilsson H, Blomqvist L, Douglas L, Nordell A, Janczewska I, Näslund E, Jonas E. MRI for the assessment of liver function and volume in liver cirrhosis *(submitted manuscript).*

CONTENTS

LIST OF ABBREVIATIONS

3D	Three-dimensional
A_{diff}%	Absolute difference in percent
AIH	Autoimmune hepatitis
ALP	Alkaline phosphatase
ALT	Alanine (amino)transferase
AMA	Anti-mitochondrial antibodies
ASGP	Asialoglycoprotein receptor
AST	Aspartate (amino)transferase
ATP	Adenosine triphosphate
AUC	Area under the curve
AUROC	Area under receiver operator characteristic curve
CASH	Chemotherapy-associated steatohepatitis
CBD	Common bile duct
CHD	Common hepatic duct
C_{max}	Maximum concentration
CPC	Child-Pugh class
CPS	Child-Pugh score
CT	Computed tomography
CTPS	Child-Turcotte-Pugh score
CV	Coefficient of variation
DA	Deconvolutional analysis
DCE-MRI	Dynamic contrast-enhanced magnetic resonance imaging
DHCE-MRI	Dynamic hepatocyte-specific contrast-enhanced magnetic resonance imaging
EF	Extraction fraction
ELEFANT	Easy LivEr Function ANalysis Toolkit
ERC	Endoscopic retrograde cholangiography
FA	Fourier analysis
FOV	Field-of-view
FT	Fourier transform
Gd-BOPTA	Gadobenate dimeglumine
Gd-DTPA	Gadopentetic acid
Gd-EOB-DTPA	Gadolinium ethoxybenzyl diethylenetriaminepentaacetic acid, gadoxetate, gadoxetic acid
GEC	Galactose elimination capacity
GGT	γ-glutamyl transferase
GI	Gastrointestinal
GSA	Galactosyl human serum albumin
HBS	Hepatobiliary scintigraphy
HBV	Hepatitis B virus
HCC	Hepatocellular cancer
HCV	Hepatitis C virus
HE	Hepatic extraction
HEF	Hepatic extraction fraction

HEFml	Total hepatic extraction capacity
HRC	Hepatic retention curve
ICG	Indocyanine green
ICG CL	Indocyanine green clearance (ml kg^{-1} min^{-1})
ICG PDR	Indocyanine green plasma disappearance rate (%/min)
ICG R15	Indocyanine green retention at 15 minutes (%)
IDA	Iminodiacetic acid
IHPBA	International Hepato-Pancreato-Biliary Association
irBF	Input-relative blood flow
IVC	Inferior vena cava
LFTs	Liver function tests
LSER	Liver-spleen enhancement ratio
MEGX	Monoethylglycinexylidide
MELD	Model for End-stage Liver Disease
MHz	Megahertz
Mn-DPDP	Mangafodipir trisodium
MR	Magnetic resonance
MRC	Magnetic resonance cholangiography
MRI	Magnetic resonance imaging
MRP	Multidrug resistance protein
MTT	Mean transit time
NAFLD	Non-alcoholic fatty liver disease
NASH	Non-alcoholic steatohepatitis
NTCP	Na^+/taurocholate cotransporting polypeptide
OATP	Organic anion transporting polypeptide
PBC	Primary biliary cirrhosis
PK-INR	Prothrombin complex – international normalized ratio
PSC	Primary sclerosing cholangitis
r_1	Longitudinal relaxivity ($s^{-1}mM^{-1}$)
R_1	Longitudinal relaxation rate (s^{-1})
R_{diff}	Relative difference
RE/time	Relative enhancement over time
RES	Reticulo-endothelial system
RF	Radiofrequency
RLF	Remnant liver function
RLV	Remnant liver volume
ROC	Receiver operator characteristic
ROI	Region of interest
SD	Standard deviation
SENSE	Sensitivity encoding
SI/time	Signal intensity over time
SI_r	Relative signal intensity
SI_r/time	Relative signal intensity over time
S_{max}	Maximum signal intensity
SNR	Signal-to-noise ratio
SOS	Sinusoidal obstruction syndrome
SPECT	Single photon emission computed tomography
SVD	Singular value decomposition

T	Tesla
T1	Longitudinal relaxation time (s)
$t_{1/2}$	Half-time
T2	Transversal relaxation time (s)
TE	Echo-time
THRIVE	T1-weighted high-resolution isotropic volume examination
TIPS	Transjugular intrahepatic porto-systemic shunt
t_{max}	Time of maximum concentration/enhancement/signal intensity
TR	Repetition time
TSVD	Truncated singular value decomposition

1 INTRODUCTION

1.1 THE EVOLUTION OF LIVER SURGERY

In ancient Babylonian times the appearance of the liver was used to foretell the future, an art known as hepatoscopy. In the Bible for example, there is a passage about the coming Babylonian attack on Jerusalem:

> *"For the king of Babylon will stop at the fork in the road, at the junction of the two roads, to seek an omen: He will cast lots with arrows, he will consult his idols, and he will examine the liver"*
> (Ezekiel 21:20-22).

In Greek mythology, two fundamentals of liver surgery are described, the first being the propensity of the liver parenchyma to bleed and secondly, the astonishing regenerative capability of the liver. As an example of the first, Homer writes in the Iliad:

> *"Achilles stabbed with his sword at the liver, the liver was torn from its place, and from it the dark blood drenched the fold of his tunic and Troy's eyes were shrouded in darkness and the light went out"*

Secondly, in the myth of the titan Prometheus, who was chained to Mount Caucasus by Zeus for giving away the knowledge of fire to the mortals, it was said that every morning, a giant eagle would come down to feast on his liver, only to come back for a new treat the next day when the liver had regenerated.

In the long-lived teachings of Hippocrates and Galen, the body was thought of as a product of four basic substances, called the four humours. These were blood, white phlegm and black and yellow bile. The liver was thought of as the source of blood and sanguification and the yellow bile was thought of as a product of the gallbladder. It was not until well into the 16th century that these teachings were seriously challenged and replaced by the embryo of science as we know it today. In 1654 Francis Glisson published his works on intrahepatic vascular anatomy and the liver capsule and its extensions, known today as the Glissonian sheath[1]. During the following centuries there were reports of debridement of liver tissues protruding from war wounds of different appearances and aetiologies. Formal liver surgery was not performed until the latter part of the 19th century, when general anaesthesia and the understanding of aseptic techniques had set the stage for surgery as we know it today. The first liver resection with a patient surviving is attributed to Langenbuch in 1887, five years after he had performed the first successful cholecystectomy. He performed an operation where a large pedunculated tumour of the left lobe was removed [2]. Liver surgery techniques improved during the 20th century with increasing patient survival and indications for surgery broadened. In 1963 Thomas Starzl performed the first human liver transplantation.

The last few decades have seen tremendous development in the field of liver surgery. From being a rarely performed procedure, liver resection has become one of the most

frequently performed interventions in the field of surgical oncology of the upper gastrointestinal (GI) tract. Furthermore, surgery for primary and secondary malignancies in the liver nowadays probably has the best overall long-term outcome of all malignancies of the upper GI tract. The expansion of liver surgery is illustrated by Figure 1, where the number of liver resections in Sweden during the last decade is shown. In 1998, a total of 155 liver resections were performed in the whole country, a number that had risen to a total of 715 in 2009[3].

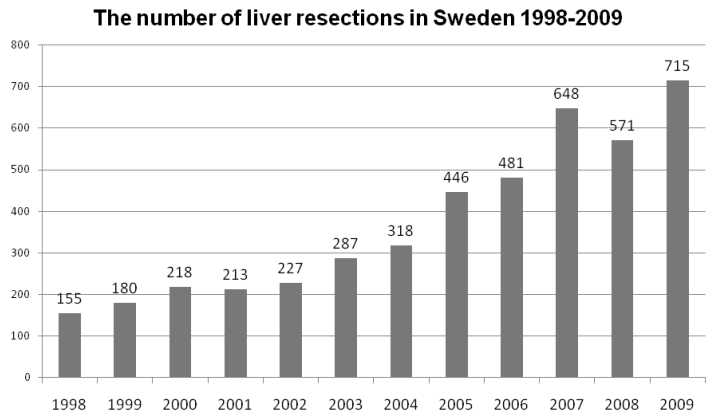

Figure 1: The increasing number of liver surgery procedures being performed in Sweden in the years 1998-2009.

Many factors have influenced the expansion of liver surgery, including developments in anaesthesia, imaging, hepatology and extended insight in liver anatomy and physiology. Also, better tools for surgical transection of the well-vascularized liver parenchyma and low central venous pressure during the parenchymal transection have led to less intraoperative haemorrhage, and mortality in liver resection for colorectal cancer liver metastases is now below 1% in specialized units[4, 5]. The key factor behind this unparalleled expansion is undoubtedly the insight that long-term survival and even cure can be achieved by the complete surgical removal of liver metastases from colorectal cancer, and to some extent, even from metastases of other origin. In parts of the world, the effects of endemic hepatitis B and C in the population are reflected in the high prevalence of liver cirrhosis and hepatocellular carcinoma (HCC), making this disease the fifth most common cancer in the world. Only surgical intervention or transplantation offer a chance of cure for HCC.

Today the art of hepatoscopy has been largely abandoned and the source of disease is seldom attributed to dyscrasia of the four humours, but the liver parenchyma continues to challenge scientists, hepatologists and surgeons with its multitude of functions, its remarkable regenerative capacity and the technical challenges it poses for the surgeon who dares enter its realm.

1.2 CURRENT ISSUES IN LIVER SURGERY AND HEPATOLOGY

The fields of hepatology and liver surgery are developing rapidly. There are, however, some issues of particular interest seen in the context of this thesis.

Despite the tremendous advances regarding the understanding of liver function and physiology together with an almost unforeseen development in the field of medical imaging, postoperative liver failure remains a serious problem. It significantly contributes to postoperative morbidity and is the major cause of mortality after liver resection [6, 7].

Liver surgery in the cirrhotic liver poses its particular challenges regarding the selection of patients suitable for surgical treatment. The challenge is to not submit patients to surgery that will succumb to liver failure, nor denying patients the chance of cure just from the notion that their liver function is not sufficient to survive the surgery.

In hepatology, dealing with autoimmune and cholestatic diseases such as primary biliary cirrhosis (PBC) and primary sclerosing cholangitis (PSC) poses its particular challenges. Staging of disease, sampling error in liver biopsy, predicting outcome for the individual patient, choosing the right time for endoscopic intervention, evaluation of the effects of medical or endoscopic treatments and finding the optimal time point for liver transplantation are just some of the problems facing the hepatologists dealing with these diseases.

1.3 LIVER ANATOMY AND PHYSIOLOGY

1.3.1 Embryology

Embryologically, the liver originates as a bud of cells in the ventral mesentery of the foregut, invading the left and right vitelline veins. The bud develops into the liver and portions of the vitelline veins later become the vena cava, the right hepatic vein and the portal vein. The middle and left hepatic veins do not originate directly from the original vitelline veins, but from consolidation of small veins formed in the liver as it grows. In foetal life, placental blood is shunted through the liver by the left umbilical vein to a portion of the left portal vein wherefrom it proceeds via the ductus venosus to the inferior vena cava (IVC) just inferior to the heart. After birth the foetal circulation changes and the ductus venosus involutes to a fibrotic band, the ligamentum venosum. It stretches between the portion of the left portal vein known as the umbilical part of the portal vein and the IVC. The umbilical vein becomes the round ligament, or ligamentum teres, in the falciform ligament. These embryological characteristics are important for the understanding of the intrinsic right and left division of the liver, as well as of the non-symmetric branching of the left portal vein.

1.3.2 A brief history of the understanding of hepatic anatomy

Already in ancient times, liver anatomy was described by the lobular arrangement of the parenchyma, using surface markings and obvious external landmarks, for example the falciform ligament, the umbilical fissure and the ligamentum venosum for the traditional division of the liver into the right and left lobes. The quadrate lobe and the caudate lobe were also described according to their anatomical landmarks. Historically

this was the prevailing system to describe the liver for centuries, and is still used for morphologic description of liver anatomy. It was not until the end of the 19th century with the works of Cantlie and Rex that the internal arrangement of the hepatic structures was used to describe the complex functional liver anatomy[8, 9]. Using injection die-casts they discovered the portal vascular watershed that divides the liver into the right and left sides. This watershed follows what is today known as the Cantlie line, which is actually a three-dimensional plane going from the gallbladder fossa down to the IVC, dividing the liver into the left and right hemilivers. This seminal work was followed by several important studies, for example by the Swedish anatomist Hjortsjö who contributed significantly to the understanding of intrahepatic biliary anatomy [10]. The works of Healey and Schroy further broadened the understanding of the intrahepatic biliary and arterial vascular anatomy, and they suggested a subdivision of the liver on three levels based on the arterial and biliary anatomy[11, 12]. The French surgeon-anatomist Couinaud suggested a similar three-levelled subdivision of the liver based on the portal vein divisions[13]. He introduced the segmental division of the liver as we know it today, numbering the segments after the arrangements of the *arrondissements* of Paris, with a total of 8 liver segments as illustrated in Figure 2b.

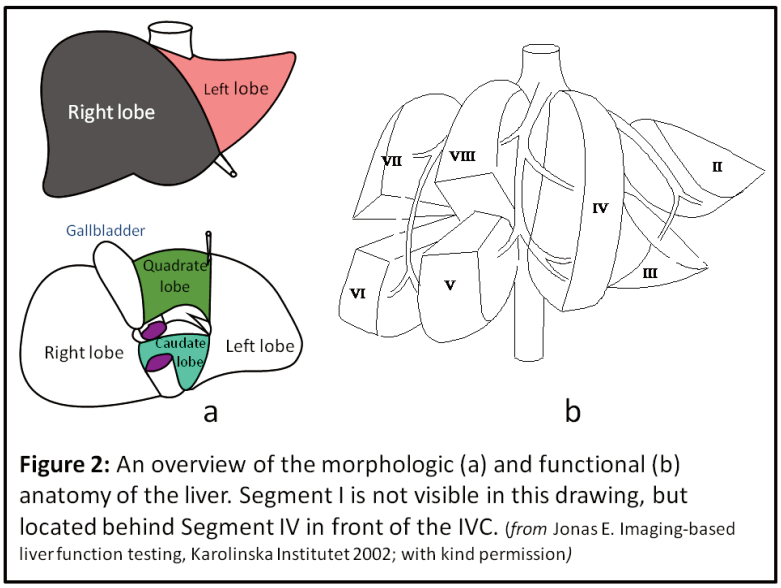

Figure 2: An overview of the morphologic (a) and functional (b) anatomy of the liver. Segment I is not visible in this drawing, but located behind Segment IV in front of the IVC. (*from* Jonas E. Imaging-based liver function testing, Karolinska Institutet 2002; with kind permission*)*

The many ways of dividing the liver into lobes, sectors, areas, segments, sections etc. based on different anatomical structures led to a significant confusion regarding the nomenclature of hepatic anatomy and also hepatic resections [14]. In an effort to overcome this "hepatic babel", the Brisbane 2000 system of nomenclature of hepatic anatomy and resection was introduced by the International Hepato-Pancreato-Biliary Association (IHPBA) [15]. In this system, the first order of division is into the left and right hemilivers, the second order divides the right hemiliver into the right anterior and posterior sections, and the left hemiliver into the left medial and left lateral sections. The third order division is into the segments that are similar to the ones described and numbered by Couinaud. In the left hemiliver the lateral section consists of segments 2 and 3, and the medial section consists of segment 4 (often subdivided into segment 4a

and 4b). In the right hemiliver the anterior section consists of segments 5 and 8, and the posterior section consists of segments 6 and 7. Segment 1 corresponds to the caudate lobe and is not part of the three-levelled division described above due to the separate and unique vascular supply, biliary drainage and vascular outflow of this segment [16]. An overview of the morphologic and functional division of liver anatomy is presented in Figure 2.

1.3.3 Anatomy

1.3.3.1 Surface anatomy

The liver is one of the largest organs of the body, located in the right upper quadrant of the abdomen contributing about 2-3% to the total body weight[17]. The lobular morphologic arrangement is described above in Figure 2a. The liver is partially covered by peritoneum and attached to the abdominal wall and diaphragm by reflections of these peritoneal coverings. At the cranio-dorsal aspect of the liver along the diaphragmatic surface, there is an area devoid of peritoneal covering referred to as the bare area or area nuda. The peritoneal reflections, somewhat erroneously referred to as ligaments, are divided into the left and right coronary and triangular ligaments. The falciform ligament originates close to the umbilicus and stretches towards the liver, going down to the exit point of the hepatic veins. The falciform ligament contains in its dorsal part the ligamentum teres previously mentioned. In liver surgery the liver often has to be mobilized by division of these peritoneal avascular folds. The liver is closely related to several organs in the upper abdominal cavity. The lesser curvature of the stomach is attached to the left liver by the lesser omentum, in the cranial part known as the gastrohepatic ligament, and in its caudal part it becomes the hepatoduodenal ligament that connects the pyloric region of the stomach and proximal part of the duodenum to the liver hilum. The ligament contains structures of utmost importance to liver surgery: the common bile duct, the hepatic artery and the main trunc of the portal vein. The right colonic flexure has a close relationship with the right liver, as does the right kidney and adrenal gland.

1.3.3.2 Vascular anatomy

The liver has a unique dual vascular supply with the portal vein contributing approximately 75% of the inflow and the hepatic artery with branches approximately 25%[18, 19]. The arterial anatomy of the liver is variable, but most commonly the hepatic artery originates from the celiac trunc together with the splenic and left gastric arteries, a pattern recognized in about 90% of patients studied [20]. The common hepatic artery usually has a suprapancreatic course as it traverses towards the hepatoduodenal ligament where it divides into the proper hepatic artery and the gastroduodenal artery. The proper hepatic artery then continues towards the liver in the antero-medial aspect of the hepatoduodenal ligament where it, usually close to the liver hilum, divides into the right and left hepatic arteries. Most commonly, the cystic artery arises from the right hepatic artery. Common variations to this pattern is a right hepatic artery branching from the superior mesenteric artery (approximately 10%) and an accessory or replaced left hepatic artery branching off from the left gastric artery (approximately 10%), running through the lesser omentum to supply the left part of the liver. More

uncommon variations (1-2%) include a completely replaced hepatic artery originating from the superior mesenteric artery or directly from the aorta[21].

The portal vein is formed by the confluence of the superior mesenteric vein and the splenic vein behind the neck of the pancreas. Other tributaries to the portal vein include the coronary or left gastric vein and the cystic veins from the gallbladder. The common trunc of the portal vein is located in the posterior aspect of the hepatoduodenal ligament and close to the liver hilum divides into the left and right portal veins. Often there is a branch to the caudate lobe from the portal vein at the hilar level. The right portal vein has a short intrahepatic course before it divides into the anterior and posterior branches to segments 5, 8 and 6, 7 respectively. Due to the embryologic origin of the left portal vein, it is somewhat different in its distribution. It often has a relatively long extrahepatic, transverse portion and enters the parenchyma as it approaches the umbilical fissure as the umbilical portion of the left portal vein[14, 22]. The venous drainage of liver blood is mainly from the three hepatic veins that drain into the IVC just below the diaphragm. The three hepatic veins are of different embryologic origin as previously mentioned. Often the left and middle hepatic veins coalesce into a common trunc before draining into the IVC. The right hepatic vein is usually of a larger diameter with a short extrahepatic course. In addition to the three main hepatic veins there is sometimes an accessory hepatic vein on the right side draining into the IVC inferior to the main trunc of the right hepatic vein. There are also regularly several bridging veins from the right-sided segments and segment 1 that drain directly into the IVC [22]. These bridging veins need to be handled carefully when mobilizing the liver to avoid profuse haemorrhage.

1.3.3.3 Bile duct anatomy

The bile is transported out of the liver by ducts that are formed by the successive joining of small bile canaliculi and ducts into consecutively larger structures, culminating in the common bile duct. Typically, the ducts from the anterior and posterior section of the right hemiliver join to form the right hepatic duct that after a short extrahepatic course joins with the left hepatic duct. There are significant anatomical variations regarding the branching of the right duct that are of great importance in liver and biliary surgery [23]. The left hepatic duct drains the left hemiliver and has less anatomical variations, as it runs along with the transverse part of the left portal vein. The left and right hepatic ducts join in the hilar part of the hepatoduodenal ligament to form the common hepatic duct (CHD). The CHD is located in the anterolateral part of the hepatoduodenal ligament where it is joined by the cystic duct. After the cystic duct junction, the CHD becomes the common bile duct (CBD). There are also significant variations in the way the cystic duct and the CHD junction, and knowledge of and respect for the complexity of the biliary anatomy is prudent when performing any hepatobiliary surgery, even cholecystectomies.

1.3.4 Liver physiology

In 1855, the famous French physiologist and scientist Claude Bernard stated: “The liver is too large to produce only bile” [24]. Time would prove him right, and today we know that the liver is an organ responsible for a multitude of complex cellular activities, some of them being storage of glycogen, synthesis of amino acids, albumin and coagulation

factors, detoxification of drugs and endotoxins as well as excretion of bile. The liver also plays a major role in glucose homeostasis through gluconeogenesis and glycogenolysis. These cellular activities are dependent on an adequate blood supply and venous drainage, but also on the integrity of the bile ducts ensuring adequate outflow of the bile.

The liver consists mainly of specialized liver cells, hepatocytes, which comprise about 60% of the liver mass. Other cells found in the liver are the endothelial cells lining the sinusoids of the liver, the epithelial cells of the bile ducts known as cholangiocytes, the phagocytic Kupffer-cells of the reticulo-endothelial system (RES) and the hepatic stellate cells, also known as Ito-cells or lipocytes [25]. The basic cellular architecture of the liver is often referred to as the hepatic lobule shown in Figure 3. The lobule is usually described as a hexagonal structure with a central vein in the middle. The central veins of the lobules eventually coalesce into the draining hepatic veins. The central vein is connected to the portal inflow by liver sinusoidal veins lined by endothelial cells with hepatocytes arranged in a columnar fashion. The space between the sinusoidal cells and the hepatocytes is known as the space of Disse. This is where the hepatic stellate cells are usually found, as shown in Figure 4. The terminal portions of the portal vein together with hepatic artery branches, arterioles, and bile ducts form the portal triads, also known as portal tracts. The hepatic arterioles are the main supplier of oxygenated blood to the bile ducts. A portion of the arterial oxygenated blood also blends with portal blood in the terminal portal branches draining into the sinusoidal veins illustrated in Figure 3[26]. The functional arrangement of the liver parenchyma is perhaps better described by the hepatic acinus also shown in Figure 3[27]. The acinus is oriented around the afferent vessels of the liver, and roughly divided into three zones with increasing distance from the oxygen- and nutrient-rich afferent vessels. The more peripheral hepatocytes receive less oxygenated blood, and the more centrally located cells are the first to be exposed to blood-borne toxins. This arrangement leads to certain disease-specific pathological processes that will affect the different zones in specific ways, and functionally, the hepatocytes of the three zones have slightly different function and different expression of enzymes[28].

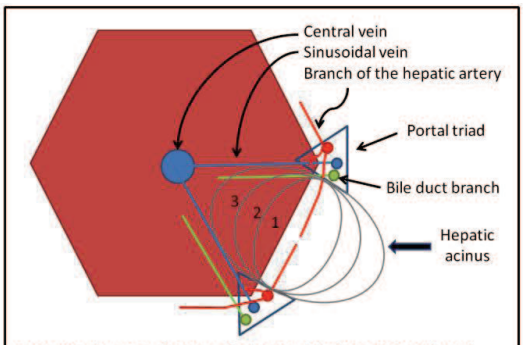

Figure 3: Schematic drawing of a hepatic lobule, portal triads and hepatic acinus with the three zones marked (1,2,3).

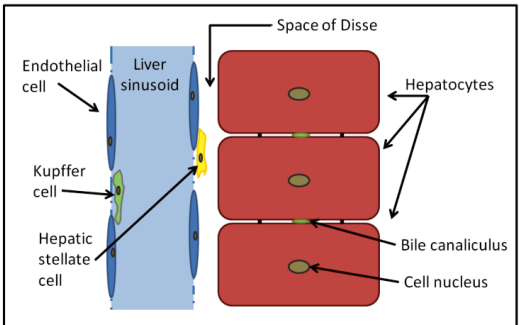

Figure 4: The main cell types that constitute the liver parenchyma.

1.4 LIVER DISEASE

Liver cirrhosis is not a distinct disease entity, but rather the result of longstanding parenchymal injury, with a wide range of possible aetiologies. For example, the injury could be due to chronic toxic exposure of the liver, such as in excessive alcohol intake, chronic inflammation as seen in chronic viral hepatitis or chronic cholestatic diseases, such as primary biliary cirrhosis (PBC) and primary sclerosing cholangitis (PSC). Other forms of chronic liver disease are the non-alcoholic fatty liver disease (NAFLD) and non-alcoholic steatohepatitis (NASH), closely related to the metabolic syndrome and seen in increasing numbers in the Western world[29]. The hepatic stellate cells are proposed to play a key role in the process from inflammation to fibrosis and ultimately to liver cirrhosis. The stellate cell is activated by inflammatory cytokines and in its activated state produces collagen that is deposited in the space of Disse, thereby increasing portal pressure, and the production of matrix degrading proteins is diminished, thereby tipping the balance of collagen formation and degradation towards increasing matrix buildup[30]. As fibrosis continues, functioning hepatic parenchyma is replaced by connective tissue, and the functional capacity of the liver is gradually impaired. The degree of fibrosis is often scored according to the system proposed by Batts and Ludwig as outlined in Table 1[31]. Other systems, such as the Metavir score, also assess the disease activity in chronic hepatitis for grading of liver disease[32]. The degree of fibrosis and cirrhosis is often not uniformly distributed within the liver and significantly differing results can be obtained from random liver biopsies. In a study of 124 patients with chronic hepatitis C, laparoscopic biopsies from the left and right liver were obtained simultaneously and in 14.5% cirrhosis was diagnosed in one side but not the other[33]. In another study on patients with fatty liver disease undergoing paired biopsies, 35% of the patients had bridging fibrosis in one biopsy, but no or only mild fibrosis in the other[34]. This uneven distribution of disease leads to significant sampling error and possible under-staging of disease grade when liver biopsies are used to grade or stage chronic liver disease[35]. Liver fibrosis has been shown to be a reversible condition, whereas cirrhosis is not.

Table 1: Fibrosis scoring system according to Batts and Ludwig[31]

Stage 0	No fibrosis
Stage 1	Portal fibrosis (fibrosis in the portal triads, but not outside of these)
Stage 2	Periportal fibrosis (fibrosis extending into the periportal space)
Stage 3	Septal or bridging fibrosis (portal triads linked by fibrotic septa)
Stage 4	Cirrhosis

In its late stages, liver cirrhosis is characterized by progressive and sometimes rapid liver failure with portal hypertension, ascites, hepatic encephalopathy and significantly increased mortality. In addition, liver cirrhosis is also identified as a major risk factor for the development of HCC. Liver cirrhosis is also known to induce changes in the relative distribution of liver volume between the right and left hemilivers. Often a relative hypotrophy of the right liver is noted with a simultaneous relative hypertrophy of the caudate lobe and left hemiliver[36-39].

1.4.1 Primary biliary cirrhosis

Primary biliary cirrhosis (PBC) is an autoimmune chronic inflammatory disease characterized by progressive destruction of intrahepatic bile ducts, resulting in cholestasis, portal inflammation and fibrosis which eventually may lead to cirrhosis and liver failure[40]. The exact aetiology is unknown, but the disease seems to affect patients with a genetic predisposition and as in many other autoimmune diseases, there is a female predominance. In PBC, 9 out of 10 patients are female with the typical patient being a woman in her fifties[40-42]. PBC is a fairly uncommon disease with prevalence rates ranging from 0.7 to 40/100 000 in epidemiological studies[43, 44]. The disease usually presents with pruritus followed by jaundice and hepato- and splenomegaly, although with increasing use of serum liver function tests in routine practice, more patients are diagnosed at an early asymptomatic stage. A pronounced fatigue is a common finding in affected individuals, and is sometimes the first symptom of the disease[45]. Diagnosis is based on the presence of anti-mitochondrial antibodies (AMA) and elevation of biochemical markers of cholestasis, especially alkaline phosphatase (ALP). If both AMA is present and ALP is elevated for a period longer than 6 months, it is highly suggestive of a PBC diagnosis[46]. Liver biopsy is no longer mandatory for diagnosis, but aids in the work-up of patients by excluding other causes of cholestasis[47]. Furthermore, it may give useful information on disease activity and stage[46]. The disease does not affect the liver uniformly and as in cirrhosis in general, there is a considerable risk of under-staging on single liver biopsies[48]. Natural history is variable and ranges from stable to rapidly progressive disease. Various attempts have been made to predict the unpredictable clinical course of patients with PBC and several prognostic models have been developed to predict survival[49-53]. Of these models, the Mayo updated natural history model for primary biliary cirrhosis is probably the most widely used. It is based on a Cox proportional hazards model where the regression coefficients for age, serum albumin, bilirubin and prothrombin time in combination with the dichotomous variables oedema and diuretic therapy are used to calculate the short-term survival probability[54]. There is no curative medical treatment for PBC, but liver transplantation is an option in late stages of the disease. Treatment with ursodeoxycholic acid has been shown to improve symptoms, biochemical status and time to liver transplantation, but results regarding its effect on overall survival are contradictory[55]. Patients with PBC have an increased risk for developing HCC, and regular ultrasound screening is recommended[56].

1.4.2 Primary sclerosing cholangitis

Primary sclerosing cholangitis (PSC) is a chronic inflammatory disease characterized by progressive obliterating fibrosis of the intra- and extra-hepatic bile ducts, ultimately leading to liver cirrhosis. The aetiology is largely unknown, but a close association with inflammatory bowel disease, especially ulcerative colitis, has been described. There is a male predominance and the prevalence is approximately 10/100 000 with a clear geographic variability[57]. The diagnosis is based on typical findings on magnetic resonance cholangiography (MRC) or endoscopic retrograde cholangiography (ERC) with beading and strictures seen in the biliary tree[46]. Liver biopsy is not mandatory for diagnosis, but is not infrequently performed in clinical practice, often to rule out overlap between PSC and autoimmune hepatitis (AIH)[46]. The disease does not affect the liver homogeneously and in cases where liver biopsy is deemed necessary, the use

of paired biopsies has been advised[58]. There is no effective medical treatment or cure for PSC. Ursodeoxycholic acid has been used, but the results are contradicting[57]. Liver transplantation is an alternative in advanced disease, but relapse in the transplanted liver is noted in as much as 20% after five years[59]. Palliation of symptoms such as pruritus and perhaps even prolonged survival can be achieved with endoscopic dilatation of dominant bile duct strictures[57, 59]. Defining which biliary strictures are significant, not only as radiologically dominant, but functionally in terms of bile flow obstruction poses a clinical challenge. Although the clinical course in the individual patient is notoriously hard to predict, most patients will be either dead or subject to liver transplantation within 12-17 years from time of diagnosis[60]. On a group level, short-term mortality can be predicted using the revised natural history model for PSC, also known as the Mayo risk score[61]. Like the PBC model, this score is based on the regression coefficients from a Cox proportional hazards model, using the parameters age, bilirubin, albumin, aspartate transaminase (AST) and the dichotomous variable history of variceal bleed. Patients with PSC are at high risk of developing cholangiocarcinoma and gallbladder cancer, and regular ultrasound screening is advocated[46].

1.4.3 Alcohol- and viral-induced liver cirrhosis

Worldwide, the burden of disease inflicted by hepatitis B virus (HBV) and hepatitis C virus (HCV) infection is staggering, accounting for almost 1 million deaths annually. Approximately half of this mortality has been attributed to liver failure and the other half to death from HCC[62]. Even though the incidence of new cases of HCV infection is declining, the number of patients with longstanding infection is still growing, and the peak regarding morbidity due to HCV infection is probably still to come[63]. Approximately one third of infected patients will develop severe liver disease (advanced fibrosis, cirrhosis or HCC) after 30 years of infection[64]. Cirrhosis in itself is a risk factor for developing HCC, but this is even more pronounced in HBV and HCV infection, with a yearly incidence of HCC as high as 8% in patients with HCV and established cirrhosis[56]. It is therefore suggested that patients diagnosed with HBV or HCV infection should regularly be screened for HCC, since diagnosis at an earlier stage is associated with better survival[56]. In northern Europe, where HBV and HCV infection is not as prevalent, alcohol has been identified as the leading cause of liver cirrhosis, with more than 60% of cirrhosis cases in Sweden being attributed to overconsumption of alcohol[65]. Overconsumption of alcohol in combination with HCV infection has been shown to be especially deleterious for the liver parenchyma, and accelerates the progression of fibrosis to cirrhosis[66].

1.5 EVALUATION OF LIVER FUNCTION

As previously mentioned, the liver has a multitude of complex cellular functions with numerous enzyme systems involved. It is futile to think that one single test, no matter how elaborate, could reflect the true functional status of all enzyme systems of this complex organ. Also previously mentioned, liver biopsy can assess the degree of fibrosis and parenchymal inflammation, but with a significant risk of sampling error. Furthermore, liver biopsy is invasive and associated with complications and even mortality[67]. Several inherently different methods to evaluate liver function non-invasively have been developed, including biochemical serum liver function tests, tests

of metabolic functional capacity, clearance tests, imaging-based liver function assessment and scoring models. The most important and frequently used methods are described in further detail below. The rationale to evaluate liver function can be to stage liver disease, prognosticate outcome for a patient or a group of patients or to preoperatively estimate total liver function and predict the postoperative remnant liver function, with the aim to avoid postoperative liver failure or death.

1.5.1 Serum liver function tests

A wide range of biochemical tests derived from serum are used to assess different aspects of liver function, generally being referred to as liver function tests or LFTs. Serum LFTs are usually readily available and inexpensive. However, results must be interpreted with caution and LFTs only give indirect information about the functional capacity of the liver parenchyma, including cellular injury, synthetic capacity and excretory function. Furthermore, serum levels of the most frequently used LFTs are non-specific and influenced by factors other than liver function. AST and alanine aminotransferase (ALT) can be used to assess ongoing hepatocyte injury and necrosis, but give limited information about the extent or severity of cell death[68]. The serum levels of ALP and γ-glutamyltransferase (GGT) usually rise in cases of cholestasis, but increased levels of ALP can also originate from bone and bowel. An isolated elevation of GGT can be indicative of alcohol abuse. Serum albumin and prothrombin time can be used to assess the synthetic capacity of the liver, but decreased levels of serum albumin can be noted in diseases associated with protein loss and inflammatory conditions. Elevated levels of unconjugated bilirubin are indicative of impaired transport into hepatocytes or decreased conjugation ability in the hepatocyte, but can also be seen in conditions with increased production of bilirubin such as hemolysis. Increased levels of conjugated bilirubin are seen in diseases associated with intra- or extrahepatic cholestasis[69]. An elevated ALP is usually seen together with increased serum bilirubin in cases with extrahepatic cholestasis[70].

1.5.2 Scoring models

Serum LFTs alone are not sufficient to stage liver disease, determine its prognosis or to preoperatively assess liver function. LFTs become more applicable when used in combination in scoring models such as the Mayo risk score models used in PBC and PSC, as well as other commonly used scoring models including the Child-Pugh score (CPS) and the Model for End-stage Liver Disease (MELD).

1.5.2.1 Child-Pugh Score

The CPS system (sometimes referred to as Child-Turcotte-Pugh score (CTPS)) was first proposed in 1964 by Child and Turcotte as a way to predict mortality after porto-caval shunt surgery[68]. It was modified by Pugh in 1973 in order to predict operative mortality and long-term outcome after surgery for oesophageal varices[71, 72]. The CPS as it is used today is made up of five variables, two of them being subjective (ascites and encephalopathy) and the other three objective LFTs. The variables used and the points attributed to them are displayed in Table 2.

The total score obtained will stratify a patient into one of three groups, known as Child-Pugh class (CPC). A total score of 5-6 will put a patient in CPC A, a total score of 7-9 will correspond to CPC B and a score of 10 or more (maximum 15) is equivalent to

Table 2: The Child-Pugh scoring system[72]

Points	1	2	3
Ascites	None	Mild	Severe
Encephalopathy	None	Grade I-II	Grade III-IV
Albumin (g/L)	>35	28-35	<28
Bilirubin (μmol/L)	<35	35-51	>51
PK-INR	<1.7	1.7-2.3	>2.3

CPC C. Although this scoring model was originally intended for surgical prognostication, it has gained widespread use in hepatology to predict long-term survival and in surgery to stratify patients in risk groups regarding risk of surgical mortality as summarized in Table 3. In a review of 118 studies CPC was found to be the most consistent and robust predictor of mortality in liver cirrhosis[73]. It has also been shown that CPC predicts mortality and morbidity after liver resection. In general, only patients with CPC A without signs of portal hypertension are candidates for major liver resection[74].

Table 3: Mortality risk in cirrhosis according to CPC

CPC	1-year survival	2-year survival	Surgical mortality(*[75])
A	95%	90%	10%
B	80%	70%	30%
C	45%	38%	82%

(*various abdominal operations, both elective and emergency procedures)

An advantage with the CPS/CPC is its ease of use and it is easily calculated bedside. The CPS model has been challenged, mainly on the basis of its use of the two subjective parameters, rendering it vulnerable to observer bias, and also due to the "floor" and "ceiling" effects inherent in the model[76]. For example, a patient with bilirubin of 51 μmol/L receives the same score as a patient with bilirubin levels at 300 μmol/L. Furthermore, the scoring model fails in separating patients with CPC A that are at high risk for complications, from those with a probable favourable surgical outcome. It is also without predictive value in chronic liver disease without established cirrhosis.

1.5.2.2 MELD

The MELD-score originated from an attempt to predict short-term results after transjugular intrahepatic porto-systemic shunt (TIPS) procedures[77]. It was later slightly modified and in its current form the MELD-score contains the variables bilirubin, creatinine and PK-INR, and is calculated by the formula:

$$MELD = 9.57 * \ln(creatinine) + 3.78 * \ln(bilirubin) + 11.2 * \ln(INR) + 6.43,$$

with bilirubin and creatinine measured in mg/L[78]. The MELD-score is predominantly used for prioritizing patients on the waiting-list for liver transplantation, since it has been shown to accurately predict the 3-month mortality[76, 79]. Allocating organs depending on the patient's MELD-score rather than waiting time has been shown to improve results after liver transplantation[80]. The MELD-score can also predict mortality after liver surgery. In a retrospective study on 82 patients with cirrhosis undergoing liver resection for HCC, it was found that a MELD-score above 8 was associated with a 29% mortality rate, compared to 0% if the MELD-score was 8 or less[81]. Another retrospective study on 154 cirrhotic patients resected for HCC found that if the MELD-score was above 11, there was a high risk of postoperative liver failure, and serious morbidity was seen in patients with a MELD-score ≥ 9[82]. The MELD-score has shown no benefit in predicting outcome in patients without cirrhosis[83].

1.5.3 Quantitative measurement of hepatic uptake, metabolism and elimination capacity

Quantitative estimations of the functional status of one or several liver enzyme systems can be obtained by the measurement of the metabolism or elimination of substances that are solely metabolized or eliminated by the liver. A vast number of such tests have been described in the literature, but few are routinely used in clinical practice[84-86]. The more frequently used or studied tests are summarized below.

1.5.3.1 MEGX

The MEGX-test (monoethylglycinexylidide) uses the conversion of lidocaine to MEGX by the cytochrome p450 system[87]. After intravenous administration of lidocaine, the serum levels of MEGX are usually assessed 15 minutes later, although other time-spans have also been used. Decreased levels of MEGX are found in patients with liver cirrhosis, and serum levels <15 ng/mL have been shown to be associated with an increased complication rate after liver surgery[88].

1.5.3.2 Galactose elimination capacity

The activity of the intracellular hepatic enzyme galactokinase can be assessed by the galactose elimination capacity (GEC) of the liver[89]. Galactose is administered intravenously, followed by repetitive blood and urine sampling. Decreased elimination rates have been shown to be associated with poorer outcome after liver surgery[90, 91].

1.5.3.3 Aminopyrine breath test

After intravenous administration of ^{14}C-labeled aminopyrine, the test relies on the demethylation and metabolism of the substance that will result in the production of radioactive $^{14}CO_2$, which can be measured in the exhaled air. The test provides information on the cytochrome p450 enzyme system, and reduced levels are seen in patients with liver cirrhosis when compared to normal controls[92]. The test has been shown to predict survival in cirrhosis, but was not proven to be superior to the CPS in

this setting[93]. The test is time-consuming and results are influenced by factors other than liver function that induce the cytochrome p450 system.

1.5.3.4 Indocyanine green clearance

Indocyanine green is an organic anionic dye that is exclusively taken up into the hepatocytes through a carrier-mediated system similar to the transport mechanisms of other organic anions and bile. It has been shown that the organic anion transporting polypeptides (OATP), specifically the OATP1B3, and Na^+-taurocholate cotransporting polypeptide (NTCP) are involved in this transmembranous transport[94]. ICG is rapidly extracted from the blood-stream at a rate that is highly dependent on hepatic blood flow, and then excreted in an unchanged form into the bile through an ATP-dependent transport system[95]. The clearance of ICG is thus dependent on hepatic blood flow, the functioning hepatocyte mass and the energy status of the liver. The elimination capacity has been described using a multitude of units, amongst them the retention rate after 15 minutes (ICG R15 (%)), the plasma disappearance rate (ICG PDR (%/min)) or ICG clearance (ICG CL (ml $kg^{-1}min^{-1}$))[85]. The standard procedure for ICG clearance involves intravenous administration of the dye, with either repetitive blood sampling or transcutaneous pulse dye densitometry to assess the serum levels of ICG at time-points dependent on how elimination is reported[95-97]. The ICG elimination capacity is probably the most widely used and studied dynamic test method to quantitatively assess liver function, with several studies showing efficacy in terms of preoperative evaluation of liver function and prediction of postoperative morbidity and mortality[98]. A safety limit of ICG R15 of 14% was found by Fan et al in a study on 54 patients with cirrhosis and HCC undergoing resection of at least two liver segments[99]. In a study on 127 patients with liver cirrhosis undergoing surgery for HCC, Lau et al also found that the safety limit for major resection was an ICG R15 of 14%. However, minor resections were feasible up to an ICG R15 of 23%[100]. A decision algorithm for liver resections in patients with cirrhosis has been proposed by Makuuchi et al, with the extent of resection being dependent on ICG R15[101]. Using this algorithm, Imamura et al presented a series of 1056 liver resections with no mortality[102]. ICG elimination as a liver function test has been questioned on the basis of its high dependency on liver perfusion and perhaps being less dependent on actual hepatocyte function. It has also been criticized for failing to show a substantial advantage for predicting outcome compared to Child-Pugh score alone[86]. Also, a significant overlap in ICG PDR between healthy controls and patients with impaired liver function has been shown[96]. The most frequent clinical use of ICG clearance for preoperative liver function assessment is seen in Asian centres, and less so in Europe and USA[103].

1.5.3.5 LiMax

The LiMax test is based on the liver conversion capacity of ^{13}C-labeled methacetin to paracetamol and $^{13}CO_2$ by the cytochrome p450 isoenzyme CYP1A2[104]. This enzyme is found only in hepatocytes, is not induced by drugs or other substances and does not have significant genetic variations[105]. The metabolite $^{13}CO_2$ can be continuously measured (in µg/kg/h) bedside in the exhaled air, and levels reflect liver functional capacity. Although the LiMax test has been shown to be an independent predictor of postoperative mortality and morbidity, there is still limited experience with this method[106].

1.5.4 Imaging-based liver function analysis

Cross-sectional imaging modalities such as computed tomography (CT) and magnetic resonance imaging (MRI) are invaluable tools for assessing liver anatomy and resectability of primary or secondary liver tumours, giving information on their size, location and number. They are also used for assessing tumour response to oncologic treatment. Furthermore, they can provide information on the status of the liver parenchyma, suggesting steatosis or liver cirrhosis, but give no quantitative information about liver functional capacity[107]. By using imaging modalities in combination with a hepatocyte-specific tracer, non-invasive sampling of the tracer is possible from all compartments visible with the imaging modality used. This usually involves sampling of blood and liver parenchymal tracer concentrations, from which quantitative functional parameters are calculated. Depending on the temporal and spatial resolution of the imaging modality, even sampling from the biliary compartment, bowel and the renal system can be performed.

1.5.4.1 Volumetric assessment

Cross-sectional imaging can be used to assess total liver volume and predict remnant liver volume (RLV) after resection with good reproducibility and low inter-observer variation, and has gained widespread use in hepatobiliary surgery[108, 109]. There is no general consensus or evidence-based limit for what the safe amount for future RLV is, but as could be expected, the risk of postoperative liver failure seems to increase with decrease in liver remnant size. In a worldwide survey of 133 centres performing liver surgery, a median value of 25% (range 15-40%) in healthy livers was regarded as a safe limit for RLV, and 50% (range 25-90%) as the limit in chronic liver disease[103]. Studies assessing the efficacy of liver volumetry to predict postoperative morbidity and mortality are contradictory and many different ways are used to report the future liver remnant, making comparison difficult. In a study on 126 patients undergoing surgery for colorectal liver metastases, Shoup et al found that patients with RLV <25% were at higher risk for postoperative hepatic dysfunction and other postoperative complications, compared to the patients with RLV >25%[110]. Still a significant number of patients with RLV >25% developed hepatic dysfunction, as did a few with >40% RLV. Ferrero et al found that liver resection could be safely performed when the future RLV was >26.5% in healthy livers, and >31% when liver function was impaired[111]. Shirabe et al related the RLV to the body surface area and found in a study on 80 patients with hepatitis undergoing resection for HCC that RLV of <250 ml/m^2 was associated with an increased risk of liver failure (38%)[112]. Another approach was used by Chun et al in a study on 68 non-cirrhotic patients who underwent liver resection after portal vein embolization[113]. In this study, the RLV was estimated from CT images, and the predicted RLV was related to the estimated total liver volume predicted by body surface area, and to body weight[114]. The study showed that safe hepatic resection in non-cirrhotic livers could be performed if the RLV to estimated total liver volume ratio was >20% or future RLV to body weight ratio was >0.4. In an attempt to predict the actual functional capacity of the remnant liver, Stockmann et al combined the LiMax test with volumetric assessment from CT images for a combined volume and function analysis to predict residual LiMax capacity after resection[106]. In a retrospective analysis he found that postoperative LiMax values less than 80µg/kg/h were associated with a 38% risk of mortality. It was also found that mortality was significantly decreased

when prospectively using volumetry and LiMax combined, avoiding resection in patients where the predicted remnant liver function assessed was below this critical value.

1.5.4.2 Scintigraphic assessment of liver function

Hepatobiliary scintigraphy (HBS) utilizes a hepatocyte-specific radioactive tracer often labelled with ^{99}Technetium (^{99}Tm). Most commonly the tracer is derived from the family of iminodiacetic acid (IDA) compounds with ^{99m}Tc-mebrofenin being one of the most widely studied compounds. Mebrofenin is rapidly and almost exclusively (98%) eliminated through the hepatobiliary pathway[115]. Similar to ICG it is taken up into the hepatocyte by the OATP system, specifically OATP1B1 and OATP1B3, the latter a transporter shared with ICG[94]. It is therefore not surprising that ICG clearance has been found to closely correlate with the uptake of ^{99m}Tc-mebrofenin[116]. It is rapidly excreted into the bile in unchanged form without biotransformation. Since the tracer is radioactive, the decay can be registered outside the body with a γ-camera, either using planar scintigraphy or single photon emission computed tomography (SPECT). Planar scintigraphy provides a 2-dimensional image of the object examined, and is especially hampered by low resolution and the artefacts imposed due to differences in thickness of different parts of the liver and the inevitable inclusion of non-hepatic tissues in the planar projections. SPECT has better resolution and the ability to produce true 3D representations and cross-sectional images with a defined slice thickness, allowing identification of anatomical structures, as well as assessment of regional liver function. HBS using IDA compounds has been used in several studies to investigate liver function in the context of hepatology, liver surgery and liver transplantation[116-124].

Liver function can also be assessed using Technetium-99m-galactosyl human serum albumin (^{99m}Tc-GSA). GSA is a glycoprotein with affinity for the liver specific asialoglycoprotein receptor (ASGP). After binding to the receptor, it is internalized into the hepatocyte by means of endocytosis. A decrease in ASGP receptors is seen in chronic liver disease, and results from ^{99m}Tc-GSA have been shown to closely correlate to other liver function tests, liver histology and scoring models[125, 126]. After intravenous administration of ^{99m}Tc-GSA, the liver and heart activity are registered, either using a conventional planar γ-camera or SPECT. At least 14 different parameters that describe various aspects of ^{99m}Tc-GSA hepatic kinetics have been described in the literature, making comparison of studies difficult[127]. The use of ^{99m}Tc-GSA scintigraphy has been evaluated in several studies for preoperative assessment of liver function, for example by Kwon et al who found a correlation between ^{99m}Tc-GSA and ICG clearance, but the ability of ^{99m}Tc-GSA to predict postoperative morbidity and mortality was better than for ICG clearance[128]. ^{99m}Tc-GSA has also been used to assess liver hypertrophy after portal vein embolisation, with the interesting findings that function seems to increase faster than volume, which has also been noted in studies on postoperative liver regeneration[127, 129-131]. A drawback with GSA scintigraphy is that, at present, it is commercially available only in Japan.

1.6 MAGNETIC RESONANCE IMAGING (MRI)

1.6.1 Basic principles of nuclear magnetic resonance

Magnetic resonance imaging is based on the physical properties of the hydrogen atom (^{1}H), with a nucleus that consists of a single proton that carries a positive charge and a fundamental characteristic known as spin. Due to the spin and the positive charge, the proton has a magnetic dipole moment, and in a classical image the hydrogen proton can be seen as a spinning magnetic dipole with a magnetic vector. When the weak magnetic field created by the spinning proton is placed in an external magnetic field (B_0) the proton will align its spin either parallel or anti-parallel to the external field. Slightly more spins will align in the parallel direction, since this is the lower energy state.

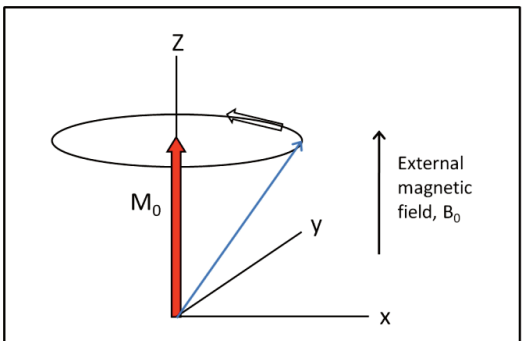

Figure 5: Nuclear precession (blue arrow). Magnetization vector (red arrow) represented by M_0.

The magnetic field of each proton wobbles around the field lines of the external field. The wobbling motion resembles a spinning gyroscope and the spinning motion is called precession and is exemplified in Figure 5. The precession speed, also called the Larmor frequency, is proportional to the strength of the external field and is given by the Larmor equation,

$$\omega_0 = \gamma_0 * B_0 \qquad \text{[Eq 1]}$$

where ω_0 is the Larmor frequency, γ_0 is the gyromagnetic ratio (γ=42.58 /MHz/T for the hydrogen nucleus) and B_0 is the magnetic field strength in Tesla (T). The individual magnetic vectors of the spinning protons will add to a net magnetization vector M_0 that builds up as the system reaches a steady-state. If energy is added to the system through an electromagnetic pulse with the same frequency as the Larmor frequency (the resonance frequency, hence magnetic resonance), a number of protons become excited by the added energy and align anti-parallel to the external field, thus shifting the direction of the net magnetization vector M_0. The electromagnetic energy is induced by a radio transmitter through a radiofrequency (RF) pulse by an external antenna coil, which transmits energy to the hydrogen nuclei, and also causes them to precess in-phase. As more energy is added to the system the magnetization vector will tip further and become more and more perpendicular to the field-lines of the external magnetic field. This way the magnetization vector is split into a longitudinal part M_z, known as the longitudinal magnetization, and a transversal part M_{xy}, known as the transversal magnetization. The direction of the magnetization vector depends on the total energy deposited, if the RF pulse is long and strong enough it will cause the magnetization vector to tip away 90° from the z-axis and the magnetization vector thus only has a transversal component. Such an RF-pulse is known as a 90° pulse, and it is this latter phenomenon that creates the transverse magnetization. The system has now reached a state called excitation. The excitation state of the hydrogen protons is unstable and as soon as the transmission of the RF-pulse ends, the longitudinal magnetization vector

will start to regain its strength whilst the transverse magnetization fades, a phenomenon known as the relaxation of the system. The relaxation consists of two independent but simultaneous processes that lead to the return to the stable system that was present before the excitation. One of these is the longitudinal relaxation, which is caused by the protons precessing anti-parallel to the external magnetic field returning to a parallel spin, since this is the lower energy state. This causes the longitudinal magnetization (M_z) vector to gradually regain its strength. The longitudinal relaxation is also known as the T1-relaxation. The time it takes for the M_z vector to return to 63% of its original strength is known as the longitudinal relaxation time or T1. As the external RF pulse is switched off, the protons that were forced to precess in-phase will gradually lose their phase coherence and thus the transverse net magnetization vector will fade away gradually. This is called the T2-relaxtion and the time it takes for the transverse magnetization vector to fade to 37% of the original (maximum) value is the time-constant called T2. Generally T1 is longer than T2 and generally T1 and T2 are longer in liquids than in fat. The transverse magnetization, created by a by a radiofrequency pulse, in turn creates a radio signal when it decays, and this signal can be detected with an external antenna. The radio signal decays as the transverse magnetization vector fades, and the time this takes is dependent on the T1 and T2 of the tissue placed in the magnetic field.

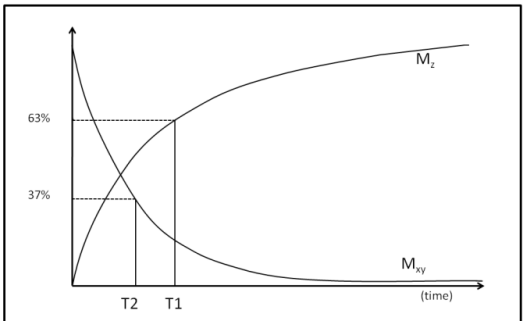

Figure 6: The relationship between T1 and T2, with T2 being shorter than T1.

1.6.2 Magnetic resonance imaging

The principles of nuclear magnetic resonance described above have been used to create images of a body or other objects placed in the magnetic field, as suggested by the Nobel laureates Mansfield and Lauterbur. The process is known as magnetic resonance imaging (MRI). An MRI scanner consists of a large permanent or superconducting magnet that creates a strong magnetic field, typically 1.5 or 3 Tesla (T) for superconductive systems. As a comparison, the field strength of the earth's magnetic field varies between 30 and 60 μT. In addition to the large magnet there are typically three magnetic coils that produce magnetic field gradient in the x, y and z directions, i.e. 3-dimensional (3D) magnetic field strength gradients can be applied. The additional magnetic coils are referred to as gradient coils. By switching on a gradient in the z direction, protons along this axis of the magnetic field will precess with unique Larmor frequencies, a phenomenon referred to as gradient encoding. This will allow spatial information to be coded into and later obtained in the z direction, equivalent to obtaining an image slice, since the RF pulse of a defined frequency will only excite those hydrogen atoms that precess with that same frequency. How "steep" this gradient is will determine the slice thickness, with thinner slices obtained in a steeper gradient. By switching on a magnetic field gradient perpendicular to the z direction, i.e. the x or y directions in the previously selected slice, the already excited protons will start to

precess with slightly different frequencies and with different phases, referred to as frequency encoding. This is repeated in the same direction with a slightly different phase each time, referred to as phase encoding. As a consequence, the RF signals emitted from the system as it relaxes will have slightly different frequencies and phases depending on where the signals originated from. The antenna that produces the RF pulse for the excitation of the protons is usually integrated into the scanner, whereas the receiving antennas or RF coils are usually smaller and designed for the particular part of the body to be examined, e.g. the brain, knee or abdomen. After the weak radio signal emitted from the examined object is detected by the receiving RF coils, the radio signals are converted into images using complex mathematical calculations including Fourier transforms.

1.6.3 Pulse sequences

By repetition of the transmitted RF pulse in combination with changes in the external field gradient strength and direction, the inherent T1 and T2 of a tissue or fluid can be used for tissue characterization in a vast variety of ways. Ultimately, this is what will cause the tissue-tissue contrast in the images obtained in MRI. The order in which the RF pulses are emitted and received and the timing when the magnetic field is turned on and off is referred to as a pulse sequence. There are several parameters that can be altered in a pulse sequence. The time between two excitation RF pulses is referred to as the repetition time (TR) and the time between the excitation RF pulse and the registration of the emitted RF signal is referred to as the echo time (TE). As described above, an RF pulse of sufficient length will tip the magnetization vector 90°. A shorter RF pulse will tip the angle less and this angle is referred to as the flip angle. A typical T1-weighted pulse sequence has a short TR and short TE, and in addition, usually a low flip-angle. When a pulse sequence is designed it will inevitably be a compromise between spatial resolution, total anatomical coverage, signal-to-noise ratio (SNR), acquisition time, artefacts and contrast resolution[132].

Images where the contrast is mainly derived from T1 relaxation are known as T1-weighted and accordingly, images that rely on T2 relaxation are referred to as T2-weighted. In a T1-weighted image, water will appear dark and fat lighter, with the reverse in T2-weighted images. In imaging using repetitive image acquisition, e.g. dynamic imaging, there is often a need for short image acquisition times with preserved spatial and contrast resolution, as well as sufficient SNR. The most frequently used pulse sequences for dynamic T1-weighted imaging are known as gradient echo sequences, allowing for fast image acquisition with sufficient spatial resolution. When MRC is performed, either T2-weighted imaging with long echo times can be applied to generate images of the bile ducts, since the bile is relatively rich in water, which has a long T2. This technique does not require any tracer to be injected. An alternative technique to perform MRC is to obtain T1-weighted images after injection of a hepatocyte-specific contrast agent and to obtain the images in the biliary excretion phase.

1.6.4 Signal intensity and image analysis in MRI

Signal intensity and SNR in MRI depend on inherent tissue properties, magnetic field strength and field inhomogeneity, the pulse sequence used and the hardware of the

scanner, especially the receiving RF coils. The SNR is also dependent on the slice thickness, matrix size and field of view (FOV). Signal intensity can also be influenced by the introduction of a contrast agent into the system.

When the RF signal is received in the receiving RF coils, it is converted into an image made up of elements called pixels (picture elements). Each pixel is a representation of a particular position in the 3D x, y and z space defined by the pulse sequence and predefined imaging parameters. The smaller the pixel, the better resolution the final image will have, but SNR will be lower. The RF signal intensity for a specific pixel is represented on a greyscale going from black to white, and all pixels together form the greyscale image seen in MRI. The pixel is a two-dimensional representation of a 3D volume and is therefore sometimes referred to as a voxel (volume element). When tracer dynamics are to be investigated, repetitive sampling is required and the images obtained will represent a dynamic process over time. This can be described by a graph where the y-axis represents, for example, signal intensity or relative signal intensity compared to native images and the x-axis is the time-line. The resulting graph will be a signal intensity-over-time curve (SI/time-curve) or the relative enhancement/relative signal intensity-over-time (RE/time-curve or SI_r/time-curve), depending on the post-processing. Such curves can either be derived from individual voxels or a group of voxels in a defined area, often referred to as a region-of-interest (ROI). When analyzing these curves, the relationship between contrast agent concentration and the resulting changes in signal intensity also has to be taken into account. Generally, signal intensity changes are proportional to changes in contrast agent concentration.

1.6.5 MRI-derived tissue functional parameters

To evaluate tracer dynamics, different strategies can be applied. For example, a simple way to evaluate liver parenchymal enhancement would be to let an observer judge the enhancement in an image as absent, small, moderate or significant. Another way could be a visual inspection and grading of the SI/time-curves obtained from repetitive sampling in dynamic MRI. In many cases such strategies might be sufficient, but the reproducibility could be questioned. In order to increase reproducibility, more advanced measures to quantify and describe tracer dynamics have been applied by deriving descriptive parameters from the SI/time-curves.

1.6.5.1 Semi-quantitative parameters

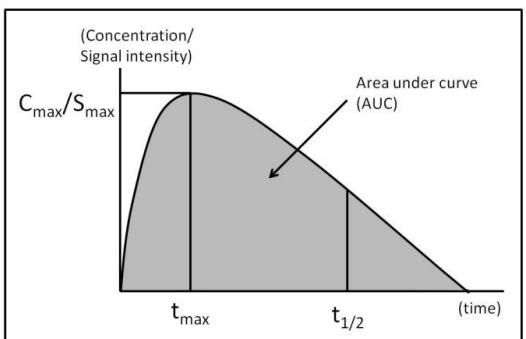

Figure 7: Semi-quantitative parameters describing the characteristics of the SI/time-curve (or SI_r/time-curve).

Parameters can be defined as semi-quantitative when the impact of the input function (i.e. the amount of tracer in the circulating blood-pool) on the resulting SI/time-curve is not accounted for. Basically these parameters are designed to give a description of the parenchymal response function and include maximum signal intensity (S_{max}) or maximum concentration

(C_{max}), time to maximum signal intensity (t_{max}), signal intensity half-time ($t_{1/2}$), and area under the SI/time-curve (AUC), as shown in Figure 7. The semi-quantitative parameters have their advantages in that they are easily accessible, intuitive and require limited post-processing. A semi-quantitative representation of tracer dynamics can also be acquired by dividing the enhancement of one organ by the other, e.g. the liver to muscle or liver to spleen enhancement ratio.

1.6.5.2 Quantitative parameters and compartmental pharmacokinetic modelling

The flow of a contrast agent between compartments such as the plasma compartment and extracellular space can be assessed using compartmental modelling, typically using extracellular contrast agents. This method is often referred to as dynamic contrast-enhanced MRI or DCE-MRI, and typically studies the permeability of the vascular bed[133]. Originally DCE-MRI was utilized in studies of the brain, but it has also been applied in MRI of the liver and other organs to study the vascular permeability in tumours and effects of anti-angiogenic chemotherapy[134]. Compartmental modelling has also been used to study the liver uptake and excretion of the hepatocyte-specific contrast agent Gd-BOPTA in rats[135-137].

1.6.5.3 Quantitative parameters and deconvolutional analysis

The amount and rate of tracer extraction from the vascular compartment by an organ is dependent not only on organ-specific characteristics, but also on the amount of tracer presented to the organ over time, i.e. the input function. The organ-specific characteristics regarding tracer kinetics, in this case the liver, can be represented by the impulse response function. If the input function is ideal, i.e. an infinitely short intravascular bolus directly into the liver without recirculation, the response function *y(t)* will equal the impulse response *h(t),* as shown in Figure 8 (I). In vivo the input function consists of the intravenously injected tracer which will be dispersed over time. The amount of dispersion is dependent on several factors, such as injection speed, site of injection, distribution volume of the tracer, cardiac output and other routes of elimination of the tracer used. The liver will therefore constantly be presented with changing concentrations of tracer. The in vivo input function is therefore not ideal and will greatly affect the response function *y(t)* as shown in Figure 8 (II). Mathematically the response function of an organ can be described as a convolution between the impulse response and the input function,

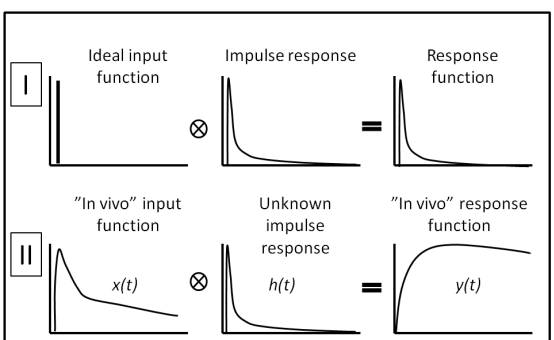

Figure 8: The principle of deconvolution to derive the impulse response curve. ⊗ denotes the mathematical convolution operator.

$$y(t) = h(t) \otimes x(t) \qquad \text{[Eq 2]}$$

where *y(t)* is the response function, *h(t)* the impulse response and *x(t)* the input function. The response function *y(t)* and the input function *x(t)* can be measured, but *h(t)* will remain unknown. However, with knowledge of the input and response functions the impulse response can be estimated by deconvolutional analysis (DA).

From the impulse response curve, several functional characteristics of the system can be derived, such as extraction fraction (EF), peak blood flow relative to the input function (input relative blood flow, irBF), area under the curve (AUC) and mean transit time (MTT), which is equal to AUC/irBF. The use of DA has previously been described in DCE-MRI of the kidneys [138, 139], and also in several studies using scintigraphy to investigate liver function[117, 121, 140-149]. The parameters obtained are sometimes referred to as model-free parameters since their calculation does not require any model-based assumptions, such as in compartmental modelling.

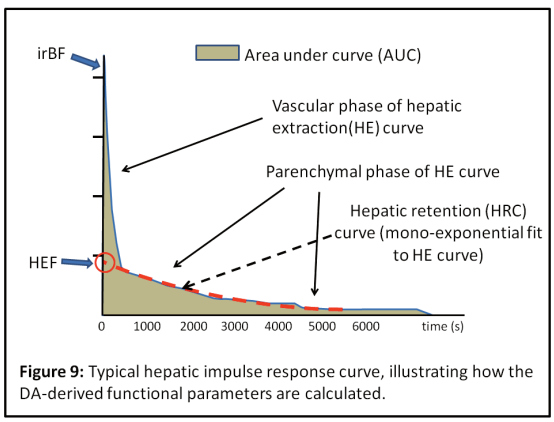

Figure 9: Typical hepatic impulse response curve, illustrating how the DA-derived functional parameters are calculated.

In the previously mentioned liver function studies, the EF was referred to as the hepatic extraction fraction (HEF) [117, 121, 141-144, 150]. Figure 9 shows a typical impulse response curve derived from liver parenchyma after DA using Gd-EOB-DTPA as tracer. The hepatic extraction (HE) curve can be divided into the initial vascular phase and the later hepatocyte retention, or parenchymal phase, as is also demonstrated in Figure 9. In the scintigraphic studies the calculation of HEF was performed by fitting a mono-exponential curve to the HE-curve in the parenchymal phase. The mono-exponential fitted curve, the hepatic retention curve (HRC), is extrapolated back to the time of the vascular peak value (i.e. t=0), and HEF is defined as the ratio between the intersection of the extrapolated HRC curve on the y-axis and the vascular peak of the HE curve, as illustrated in Figure 9 and described by Equation 3,

$$HEF = \frac{HRC(t_0)}{HE_{\max}(t_0)} \qquad \text{[Eq 3]}$$

MTT is the area under the impulse response curve (AUC) from peak value to 0 divided by the peak value of the curve (equal to irBF), and describes the mean time for a unit of the studied substance from entrance into the ROI to exit, which in the case of the liver can be either by excretion into the bile ducts or vascular wash-out.

DA can be performed using several mathematical methods, including Fourier analysis (FA) or matrix inversion. FA is described as shown in Equation 4:

$$h(t) = FT^{-1}\left\{\frac{FT\{y(t)\}}{FT\{x(t)\}}\right\} \qquad \text{[Eq 4]}$$

where FT is the Fourier transform and FT^{-1} the inverse Fourier transform. FA has the advantage of being straightforward, but suffers from high-frequency artefacts resulting from the abrupt end points of *x(t)* and *y(t)*. To avoid this abrupt end of data, a smooth appended curve can be added to the end of *x(t)* and *y(t)* to bring these curves down to zero. This is generally done by appending a cosine function from 0 to π/2 with the initial height of the last point of *x(t)* and *y(t)*[145].

By formulating the convolution in Equation 1 into matrix form, the equation can instead be solved by matrix inversion, using singular value decomposition (SVD) as shown below:

$$\begin{bmatrix} y(t_1) \\ y(t_2) \\ y(t_3) \\ \dots \\ y(t_N) \end{bmatrix} = \begin{bmatrix} x(t_1) & 0 & 0 & \dots & 0 \\ x(t_2) & x(t_1) & 0 & \dots & 0 \\ x(t_3) & x(t_2) & x(t_1) & \dots & 0 \\ \dots & \dots & \dots & \dots & \dots \\ x(t_N) & x(t_{N-1}) & x(t_{N-2}) & \dots & x(t_1) \end{bmatrix} \cdot \begin{bmatrix} h(t_1) \\ h(t_2) \\ h(t_3) \\ \dots \\ h(t_N) \end{bmatrix} \Rightarrow y = A \cdot h \qquad \text{[Eq 5]}$$

Since *A* is a square matrix it will divide into SVD as,

$$A = U \cdot W \cdot V^T = U \cdot \left[diag(w_i) \right] \cdot V^T \qquad \text{[Eq 6]}$$

where *U* and *V* are orthogonal (i.e. their inverses equal their transposes) and *W* is diagonal with the elements w_i such that

$$w_1 \geq w_2 \geq \dots w_N \geq 0 \qquad \text{[Eq 7]}$$

h(t) is solved through matrix inversion:

$$h = A^{-1} \cdot y \Rightarrow h = V \cdot \left[diag(1/w_i) \right] \cdot (U^T \cdot y) \qquad \text{[Eq 8]}$$

If one or more of the w_i are zero or close to zero, the matrix inversion becomes ill-conditioned. Hence, noise in the data becomes magnified in the least square solution (i.e. Equation 8), and makes the result of no practical value. One solution to this problem is the principle of regularization, or more specifically, truncated SVD (TSVD). In TSVD the threshold *c* was defined as *N(1-c)*, where *N* is the total number of singular values and *c* the threshold, ranging from 0 to 1. For singular values beyond this cut-off, $1/w_i$ is not computed, but instead replaced by zero.

1.6.6 Gd-EOB-DTPA (gadoxetic acid)

The first contrast agent for MRI to be approved for clinical use was Gd-DTPA (Magnevist®, Bayer Schering Pharma, Berlin, Germany), which was introduced in 1988. It was followed by a number of other substances and in 2004 Gd-EOB-DTPA (gadolinium ethoxybenzyl diethylenetriaminepentaacetic acid, gadoxetic acid, gadoxetate (Primovist®, Bayer Schering Pharma, Berlin, Germany)), was introduced on the market in Europe. Like other gadolinium-based contrast agents, Gd-EOB-DTPA utilizes the paramagnetic properties of the gadolinium (Gd) atom and the dipole-dipole

interactions it exerts on the hydrogen atoms. Due to these interactions, the presence of Gd in a tissue will induce a shortening of the T1 relaxation. The gadolinium atom is a toxic heavy metal atom and therefore needs to be chelated to other substances to reduce its toxicity. Depending on the pharmacological properties of the Gd ligand, the tumbling rate will differ. The closer this tumbling rate is to the Larmor frequency, the more T1 relaxtion will occur. The capacity of a Gd compound to induce T1 relaxation is referred to as the longitudinal relaxivity (r_1) of the contrast agent and is measured in ($s^{-1}mM^{-1}$). The relaxivity is dependent not only on the magnetic field strength and temperature, but also on the amount of plasma protein binding of the substance[151]. Therefore, a contrast agent does not necessarily have the same relaxivity in blood, plasma or tissue as it has in water or a saline solution[152, 153]. Animal studies have shown that the relaxivity of Gd-EOB-DTPA in liver (r_1=9.3 $s^{-1}mM^{-1}$) differs somewhat from that in blood (r_1=7.3 $s^{-1}mM^{-1}$) at 1.5 T[154].

To distinguish dynamic MRI with a hepatocyte-specific agent used as tracer from conventional DCE-MRI with extracellular agents, the former will in this work be referred to as dynamic hepatocyte-specific contrast-enhanced MRI or DHCE-MRI.

1.6.6.1 Pharmacologic properties of Gd-EOB-DTPA

Gd-DTPA is a highly hydrophilic compound and therefore distributed strictly in the extracellular compartment, and eliminated almost exclusively through the kidneys[155]. Gd-EOB-DTPA on the other hand is slightly more lipophilic due to the addition of the ethoxybenzyl group. After intravenous injection it is distributed in the extracellular space with a relatively low plasma protein binding (10%), and a distribution volume of approximately 0.21 L/kg[155, 156]. It is generally well tolerated with few serious side effects[156, 157]. From the blood stream, Gd-EOB-DTPA is actively taken up into hepatocytes mainly through a carrier-mediated system, but possibly also by passive diffusion. Several studies have suggested the organic anion transporting polypeptides (OATP) and the Na^+/taurocholate cotransporting polypeptide (NTCP) as responsible for the transmembranous transport of Gd-EOB-DTPA [158-161]. It has also been shown that the uptake of Gd-EOB-DTPA and subsequent enhancement of hepatocellular carcinoma cells is highly dependent on the expression of the OATP8/1B3 isoenzyme[162-164].This uptake mechanism is shared in part with ICG and mebrofenin used for liver function assessment as previously mentioned. From the hepatocyte, Gd-EOB-DTPA is excreted in an unchanged form into the bile canaliculi by the ATP dependent multidrug resistance protein (MRP2), also known as ABCC2[165, 166]. The MRP2 enzyme is also involved in the excretion of bilirubin from the hepatocyte. Gd-EOB-DTPA in plasma is also eliminated by glomerular filtration in the kidneys in about equal amounts as by the hepatobiliary pathway (43.1-53.2% and 41.6-51.2% respectively), and the plasma half-life is approximately one hour[156]. As could be expected when liver function is impaired, biliary excretion is decreased and subsequently the proportion eliminated by renal excretion is increased[167].

1.6.6.2 Clinical use

Gd-EOB-DTPA is commercially available in large parts of the world as Primovist® (Europe and Asia) or Eovist® (USA). Gd-EOB-DTPA is provided in a solution of 0.25 mmol/mL, with the normal clinical dose being 0.1mL/kg. In the first phase after

intravenous administration, the major part of the administered dose of Gd-EOB-DTPA is still in the blood stream and can therefore be utilized in the same fashion as extracellular contrast agents, for example for vascular imaging[159]. In later phases, due to the hepatocellular uptake of the contrast agent and subsequent shortening of T1 relaxation, hepatocytes will enhance more on T1-weighted imaging compared to tissue and liver lesions that do not contain hepatocytes. In healthy liver tissue, there is a maximum enhancement about 20 minutes after the intravenous administration[156]. In several studies the hepatocyte-specific properties of the substance have been shown to increase both the detection rate of liver lesions and the ability to characterize these lesions[168-173]. In later phases there is biliary excretion and Gd-EOB-DTPA can be used for T1-weighted MRC, as well as for the detection of bile leaks and bilomas[174-176].

1.6.6.3 Results from animal and human studies on liver function

A early as 1993 it was suggested that the hepatocyte-specific properties of Gd-EOB-DTPA could be used to evaluate liver function[155]. This was followed by several animal studies using experimentally induced hepatocellular damage. Schmitz et al found that elimination half-lives of Gd-EOB-DTPA using both scintigraphy (^{153}Gd-EOB-DTPA) and MRI were significantly prolonged in rats with common bile duct obstruction or chemically induced fatty liver[177]. Kim et al induced hepatocellular injury in rats using intraperitoneal administration of carbon tetrachloride (CCl_4) solution, and found a dose-dependent decrease in maximum liver relative enhancement and relative enhancement half-time. These findings were also significantly correlated to ICG half-time and serum levels of bilirubin and prothrombin time[178]. In a study on regional liver function utilizing a rat ischemia-reperfusion model, Shimizu et al found that when selectively clamping the right liver lobe for 30, 60 and 90 minutes in three groups of rats, there was a significant increase in relative enhancement in late-phase T1-weighted images from the ischemic lobe compared to the non-ischemic liver lobe in the 60 and 90 minutes ischemia rats. Furthermore, a significant correlation between relative enhancement half-time and clamping time was observed. They also analyzed the ATP concentration in the harvested rat livers and found a significant correlation between ATP content and relative enhancement half-time, suggesting that this may reflect the function of the ATP dependent biliary excretion of Gd-EOB-DTPA and hence the energy status of the liver[179]. Using DA to calculate HEF, Ryeom et al showed that after inducing liver injury to rabbits by repetitive administration of CCl_4, the ICG-R15 increased as HEF decreased with an almost linear relationship[180]. In two studies from Tsuda et al, the ability of Gd-EOB-DTPA enhanced MRI to differentiate between liver steatosis and NASH and the progression of fibrosis in NASH were demonstrated. The first study showed significantly later t_{max} and relative enhancement $t_{1/2}$ in the NASH group compared to the steatosis group[181]. The second study found significant correlations between t_{max}, $t_{1/2}$ and liver fibrosis[182].

The first published study that addressed Gd-EOB-DTPA-enhanced MRI and liver function in humans was published in 2008 by Tschirch et al[183]. This study evaluated the visualization of the bile ducts in T1-weighted MRC in patients with liver cirrhosis compared to normal controls. In the control group, the MRC was judged as sufficient after 20 minutes in all subjects, but only in 40% of the cirrhosis group. The study also showed that elevated PK-INR and serum bilirubin correlated to insufficient biliary tree

visualization[183]. In a study on 198 patients with chronic liver disease and cirrhosis, Motosugi et al found that the liver-to-spleen contrast ratio at 10 and 20 minutes correlated to ICG R15 and Child-Pugh class, but not to serum albumin, bilirubin or prothrombin time[184]. Like Tschirch et al, Takao et al also addressed the visualization of bile ducts in patients with chronic liver disease compared to healthy controls. Although the patients in this study had less pronounced liver dysfunction it was found that the signal intensity in the major bile ducts at t_{max} was significantly lower in the patient group and that ICG R15 was a significant predictor of the signal intensity of the major bile ducts[185]. The effects of liver function on parenchymal enhancement after administration of Gd-EOB-DTPA was investigated by Tajima et al in a study where signal-to-noise ratio was measured in a group of 48 patients with either impaired or normal liver function[186]. They found significantly lower signal intensity in the parenchyma of patients with chronic liver disease compared to the group with normal liver function. A significant correlation between parenchymal signal intensity and ICG R15 was also noted[186]. A more advanced way to quantify the hepatic uptake of Gd-EOB-DTPA was applied by Katsube et al in a study where actual T1 relaxation time and not signal intensity in the liver parenchyma was measured before and at different time-points after administration of Gd-EOB-DTPA. The study involved a total of 91 patients who either had normal liver function, chronic hepatitis or liver cirrhosis graded as Child A or B. The reduction in T1 relaxation time was significantly affected by liver function, mirroring the decreased uptake of Gd-EOB-DTPA in liver disease[187]. Significant correlations between parameters obtained by ^{99m}Tc-GSA scintigraphy and those obtained from dynamic Gd-EOB-DTPA enhanced MRI were found in a study on 33 patients by Nishie et al[188].

2 AIMS

2.1.1 Paper I

The aim of the first study was to assess the feasibility of calculating HEF and irBF on a segmental level using DHCE-MRI, and to evaluate two different mathematical strategies for DA: FA and TSVD.

2.1.2 Paper II

The aim of the second study was to compare the results of DHCE-MRI-derived quantitative and semi-quantitative parameters in PBC patients with normal controls. For the patient group, the aim was also to explore the correlation between DHCE-MRI derived parameters and the CPS, MELD and Mayo risk score.

2.1.3 Paper III

The aim of study three was to use DHCE-MRI for global and segmental liver volume assessment and also to quantitatively evaluate global and segmental liver function. A secondary aim was to explore the heterogeneously distributed liver function in PSC by comparing the discrepancies in function and volume in PSC patients with those in a healthy control group. In the patient group, an aim was also to assess the correlations of global functional parameters with the CPS, MELD and Mayo risk scores and to assess the correlations of cholangiographically graded bile duct obstruction with segmental functional parameters.

2.1.4 Paper IV

The primary aim of Paper IV was to investigate patients with liver cirrhosis with DHCE-MRI to detect possible discrepancies in the segmental distribution of liver volume and function and by using a simulation of surgical decision-making, to demonstrate the effect of non-homogeneous dysfunction on predicted residual liver function. A secondary aim was to explore the correlation of DHCE-MRI-derived liver function parameters with the CPS and MELD-score, and to assess the ability of the studied parameters to discriminate between groups with normal and compromised liver function.

3 MATERIAL AND METHODS

3.1 STUDY SUBJECTS

All studies were approved by the Regional Ethical Review Board in Stockholm and informed consent was obtained from all participants prior to examination. All study participants were asked to be fasting for at least four hours prior to the MRI examination.

3.1.1 Paper I

The study was performed on 20 healthy volunteers, 10 men and 10 women, age ranging from 22 to 45 years without history of hepatobiliary disease, previous hepatobiliary surgery or alcohol abuse. No abnormal serum liver function tests or signs of renal insufficiency were found among the participating study subjects. The clinical characteristics of the control group are presented in Table 4.

Table 4: Characteristics of healthy volunteers (control group)

	Controls (n=20)	**(Reference)**
Gender (m/f)	10/10	
Age (years)	33.2 ±6.8 (20)	
Bilirubin (µmol/L)	12.6 ±5 (9)	<26
Albumin (g/L)	42 ±2 (19)	36-48
Creatinine (µmol/L)	83 ±17 (19)	<100(men); <90(women)
PK-INR (INR)	1.1 ±0.1 (19)	<1.2
ALP (µkat/L)	1.04 ±0.46 (19)	<1.9
ALT (µkat/L)	0.41 ±0.26 (20)	<1.20(men); <0.76(women)
AST (µkat/L)	0.32 ±0.08 (20)	<0.76(men); <0.61(women)

Values represent means ± standard deviation (SD)

(Numbers within brackets in the middle column denote number of observations)

3.1.2 Paper II

Twelve patients with PBC were included in the study and the 20 healthy volunteers from the first study were used as controls. For patients, relevant demographic and clinical data were documented, as well as the results of LFTs from the most recent visit documented in their clinical charts. The CPS, MELD and Mayo risk score were calculated for each patient. The patient characteristics are presented in Table 5. Patients in the PBC group were older than the controls and gender-wise an expected female predominance was observed. Liver disease in the patient group as a whole was mild, as can be seen in the relatively low CPS, MELD and Mayo risk scores.

Table 5: PBC patient characteristics

	Patients (n=12)	**(Reference)**
Gender (m/f)	1/11	
Age (years)	62.8 ±7.5	
Bilirubin (μmol/L)	14 ±9	<26
Albumin (g/L)	36 ±4	36-48
Creatinine (μmol/L)	67 ±10	<100(men); <90(women)
PK-INR (INR)	1.0 ±0.2	<1.2
ALP (μkat/L)	3.52 ±3.85	<1.9
ALT (μkat/L)	0.74 ±0.41	<1.20(men); <0.76(women)
AST (μkat/L)	0.77 ±0.48	<0.76(men); <0.61(women)

Values represent means ±SD

Disease characteristics of PBC patients

	Median / proportion	**(Min – Max)**
MELD	6	6 - 14
CPS	5.5	5 - 7
Mayo risk score	5.4	4.0 - 7.8
Ursodeoxycholic acid treatment (yes/no)	11/1	

3.1.3 Paper III

Twelve patients with PSC were included and the 20 healthy volunteers from the first study were again used as controls. For patients, relevant demographic and clinical data were documented, as well as results of serum LFTs from the visit closest to the MRI examination date documented in their clinical charts. The CPS, Mayo risk score and MELD-score were calculated for each patient. The PSC patient characteristics are presented in Table 6.

Table 6: PSC patient characteristics

	Patients (n=12)	**(Reference)**
Gender (m/f)	6/6	
Age (years)	43.8 ±15.8	
Bilirubin (µmol/L)	11 ±6	<26
Albumin (g/L)	37 ±5	36-48
Creatinine (µmol/L)	67 ±16	<100(men); <90(women)
PK-INR (INR)	1.1 ±0.2	<1.2
ALP (µkat/L)	3.52 ±3.90	<1.9
ALT (µkat/L)	1.54 ±1.81	<1.20(men); <0.76(women)
AST (µkat/L)	1.09 ±1.14	<0.76(men); <0.61(women)

Values represent means ±SD

Disease characteristics of PSC patients

	Median / proportion	**(Min – Max)**
MELD	6.5	6 - 13
CPS	5	5 - 7
Mayo risk score	0.06	-1.65 - 0.85
Ursodeoxycholic acid treatment (yes/no)	8/4	
Ascites (yes/no)	0/12	
History of endoscopic sphincterotomy (yes/no)	1/11	
History of variceal bleed? (yes/no)	0/12	

3.1.4 Paper IV

Ten patients with varying degrees of alcohol- and/or viral hepatitis-induced liver cirrhosis were included in the study. The patients were regularly seen as outpatients participating in a screening program for HCC, or had a history of liver decompensation requiring hospitalization. For patients, relevant demographic and clinical data were documented, as well as results of serum liver function tests from the visit closest to the MRI examination date as documented in their clinical charts. The CPS and MELD-score were calculated for each patient. Patient characteristics for the cirrhosis patients are presented in Table 7. The control group again consisted of the healthy volunteers examined in the first study.

Table 7: Cirrhosis patients clinical characteristics

	Patients (n=10)	**(Reference)**
Gender (m/f)	8/2	
Age (years)	55.8 ±5.3	
Bilirubin (μmol/L)	35 ±23	<26
Albumin (g/L)	32 ±8	36-48
Creatinine (μmol/L)	91 ±23	<100(men); <90(women)
PK-INR (INR)	1.4 ±0.3	<1.2
ALP (μkat/L)	2.28 ±1.04	<1.9
ALT (μkat/L)	0.97 ±0.69	<1.20(men); <0.76(women)
AST (μkat/L)	1.47 ±1.13	<0.76(men); <0.61(women)

Values represent means ±SD

Disease characteristics

		Median	**(Min-Max)**
MELD		13	6 -19
CPS		7	5 - 12
CPC	**(n)**		
A	4		
B	5		
C	1		

3.2 MRI PROTOCOL

In all studies, MRI was performed using a Philips Intera 1.5 T scanner (Best, Holland), with a Philips four-channel SENSE body coil. The MRC in Paper III was performed using a heavily T2-weighted half-Fourier single-shot fast spin-echo sequence (8000/800 ms TR/TE). A 40 mm thick section acquired during breath-hold was repeated in 12 different radial projections centred at the common bile duct. The dynamic contrast-enhanced sequence was performed using a T1-weighted 3D spoiled gradient-echo sequence (TR/TE/flip angle = 4.1 ms/2.0 ms/10°, FOV=415 mm, matrix resolution 256x192, 40 slices, slice thickness 10 mm and SENSE factor R=2). The volume was imaged in a single breath-hold at repeated time points (12s scan time per acquired volume) and the subjects were asked to hold their breath at the same depth during each acquisition. Three volumes were acquired pre-contrast for baseline calculations in all studies. This was followed by 38 volumes with step-wise increase in sampling intervals up to a total sampling time of 90 minutes in Paper I, II and III. In Paper IV, the last volume was acquired at 45 minutes after contrast injection, resulting in a total of 35 volumes acquired for the patients. For the controls, the images acquired after 45 minutes post injection were discarded before analysis in the fourth study. Times between sampling volumes were chosen taking into account the subjects' physical capacity, data acquisition requirements and test substance dynamics. A dose of 0.1 mL/kg Gd-EOB-DTPA 0.25 mmol/mL was injected into the anterior cubital vein, coinciding with the start of the fourth acquired volume. The contrast was injected using a power injector (Spectris MR injector System, Medrad, Pittsburgh), at an infusion rate of 2 mL/s, followed immediately by a bolus of 20 mL of saline (NaCl 0.9%) at the same infusion rate.

3.3 IMAGE ANALYSIS AND CALCULATION OF OUTCOME PARAMETERS

In all studies, segments were anatomically defined and the anatomical nomenclature adhered to as proposed by Strasberg and the IHPBA[14, 15]. Segment IV was subdivided into IVa and IVb. The horizontal intersegmental plane was defined as being at the level of the division of the portal vein into the left and right portal branches. From a seed-point placed in the IVC, lines were drawn in the plane of the right hepatic vein, middle hepatic vein and the falciform ligament/umbilical fissure creating the vertical inter-sectional boundaries. Segment I was manually outlined in every slice where it was visible according to the anatomical landmarks as described by Dodds et al [16]. Relative signal intensity in the voxels was calculated as the logarithmic ratio expressed in Equation 9,

$$SI_r(t,\rho) = \ln\left(\frac{S(t,\rho)}{S_0(\rho)}\right) \qquad \text{[Eq 9]}$$

$SI_r(t, \rho)$ is the relative signal intensity at time t in voxel ρ. $S_0(\rho)$ is the mean image intensity in voxel ρ from the pre-contrast images, i.e. baseline signal intensity. $S(t, \rho)$ is the measured image intensity in voxel ρ at time t. The concentration of tracer in the voxel, $C(t,\rho)$, was assumed to be approximately proportional to the relative signal intensity in the voxel as described in Equation 10.

$$C(t,\rho) \propto SI_r(t,\rho) \quad \text{[Eq 10]}$$

For the deconvolution calculations, data points were interpolated to equidistant spacing of 60 s over the entire acquisition time length. To minimize effects of noise, mainly due to patient motion, low pass filtering of data was used by applying a seven-point sliding window filter in both the input and parenchymal response function (SI_r/time) curves. The impulse response curve resulting from DA was not filtered. For deconvolution using FA, an appended tail (FA+tail) was added using a cosine function from *0* to $\pi/2$ with an amplitude of the same height as the last point of $x(t)$ and $y(t)$. The length of the tail was set to be three times the length of the total sampling period of 90 minutes. When TSVD was used, a static truncation threshold was set at $c=0.07$.

In all studies, HEF was calculated as described by Equation 3 with the HRC curve being a mono-exponential fit to the HE curve from 420 s to 1800 s. The initial time-point was chosen by visual inspection of the DA-derived impulse response curves, where it was clear that the vascular phase of the HE curve had ended and the parenchymal phase started. The end time-point was chosen arbitrarily to be 1800 s. The perfusion parameter irBF was calculated as the peak value (initial value at t=0) of the impulse response curve relative to the peak value of the input function normalized to 1. As described above, MTT is the AUC of the impulse response curve divided by the peak value of the same curve, which is equal to irBF. Since image acquisition ended before the impulse response had reached 0, the HE curve had to be extrapolated down to y=0 so that AUC could be calculated. For this purpose, the HE curve was extrapolated by a continuation of the mono-exponential fit to t= 3* the time of the endpoint (in this work 3*1800 s). At this point, the height of the HE-curve was approximately zero.

Image analysis and calculation of functional parameters (both semi-quantitative and DA-derived) were performed using the in-house ELEFANT software (Easy LivEr Function ANalysis Toolkit) written in MATLAB® (MathWorks, Inc., Novi, MI, USA).

3.3.1 Papers I and II

In the first two studies, the input function was defined by a ROI placed in the hilar part of the portal vein. To ensure that the input function ROI was truly representative of the portal vein over the entire acquisition period, it was adjusted manually in each dynamic acquisition when needed. Liver parenchymal response function curves were defined by placing three parenchymal ROIs in each liver segment, avoiding major blood vessels and visible bile ducts. ROI size was chosen arbitrarily by the investigator. For calculation of segmental parameters in Paper I, the mean HEF and irBF of the three segmental ROIs were regarded as the resulting HEF and irBF for that particular segment. In Paper II, the SI_r/time-curves of all voxels in the three ROIs combined were pooled and regarded as the parenchymal response function of that segment, and HEF and irBF were calculated by DA of this response function. In Paper II, global HEF, irBF and MTT for each study subject were calculated by obtaining the median of the segmental results for the studied parameters.

In Paper I, both TSVD and FA were used for DA, whereas in Paper II only TSVD was used.

In Paper II, semi-quantitative parameters were also calculated. Maximum relative signal intensity (C_{max}) and time to maximum relative signal intensity (t_{max}) were calculated directly from the parenchymal SI_r/time-curves in the segmental ROIs. Since the excretion half-time for Gd-EOB-DTPA is much longer than the time-span used (90 minutes), $t_{1/2}$ was calculated using a curve fitting model, given by Equation 11,

$$f = k_1 * e^{(-ln(2)t/\,t_{1/2})} - k_2 * e^{(-\ln(2)t/TU)} \qquad \text{[Eq 11]}$$

where f is the fitted curve, and the fitting parameters k_2 and TU describe contrast uptake, while k_1 and $t_{1/2}$ describe the liver contrast excretion. The starting point for the fit was selected to be t = 240s. Apart from segmental calculations of these parameters, a global C_{max}, t_{max} and $t_{1/2}$ was obtained by calculation of the median values of the segmental results.

3.3.2 Papers III and IV

In these two studies, the input function was not derived from the portal vein, but rather defined by a ROI placed centrally in the parenchyma of the spleen. To ensure that the input function ROI was truly representative of the blood content of the spleen over the entire acquisition period, it was adjusted manually when needed. In hepatobiliary phase images with optimal contrast between liver parenchyma and surrounding tissues, the liver contour was manually outlined in every slice in a caudal-cranial fashion, excluding the major hilar vascular and biliary structures. The volumes of all voxels within these defining borders were added to obtain total liver volumes for each subject. The volume of a liver segment as defined by the liver contour and the inter-sectional and inter-segmental boundaries described above, was obtained by adding the volumes of all voxels within the segmental borders for that particular segment. Fifty percent of the voxels in the intersegmental plane were regarded as representative of the superior segments (II, IVa, VII and VIII), and 50% as part of the inferior segments (III, IVb, V and VI). The voxel volume, determined by the FOV and matrix resolution parameters defined above, was approximately 13 mm^3 (1.62x1.62x5 mm). A response function was obtained from each individual voxel within the liver contour, with the response function being the SI_r/time-curve for the voxel. Both TSVD and FA were used for DA in these two studies.

Based on findings in Paper I and II, voxels with HEF above 0.7 or irBF above 1 were regarded as artefacts and omitted from subsequent analysis regarding functional parameters, but were included for calculation of total liver volume. The voxels representing vascular structures and not liver parenchyma were expected to have high perfusion with high irBF values. Since the study aimed at examining the status of the liver parenchyma, the voxels representing vessels were not wanted in further calculations. Therefore, upon completion of calculation of irBF for all voxels, those with an irBF above a user-defined threshold logically representing vessels, were omitted from subsequent analysis, including the liver parenchymal and segmental volume calculations.

Total liver function was defined as the total hepatocyte extraction capacity of Gd-EOB-DTPA. This parameter was obtained by adding the individual HEF of all remaining (parenchymal) voxels within the liver boundaries and expressed as HEFml. For every segment the functional capacity was obtained in a similar fashion, adding all parenchymal voxels within the predefined segmental borders.

In Paper IV, a semi-quantitative liver function assessment was also obtained by calculating the liver-to-spleen enhancement ratio (LSER) measured at different time-points. The LSER was calculated by placing three ROIs in each liver segment. The sum of all voxels within these three ROIs yielded the parenchymal response curve (SI_r/time-curve) for that particular segment. From these data the SI_r in each liver segment at time-points 10, 20, 30 and 45 minutes post contrast injection was obtained, and divided by the SI_r of the splenic ROI at the corresponding time-point as shown in Equation 12:

$$LSER = \frac{SI_{rL}(t,\rho_L)}{SI_{rS}(t,\rho_{S)}} = \frac{\ln S_L(t,\rho_L) - \ln S_{0,L}(\rho_L)}{\ln S_S(t,\rho_S) - \ln S_{0,S}(\rho_S)} \qquad \text{[Eq 12]}$$

Thus four LSER values (LSER-10, LSER-20, LSER-30 and LSER-45) were obtained for each segment. A global LSER for the liver at each time-point was obtained by calculating the median LSER of all segments for every study subject.

With the aim to explore the heterogeneous distribution of liver function, the differences in segmental contributions to total liver function and volume were calculated, and as a way to describe the discrepancies between these two variables, absolute and relative differences were calculated in every segment. The absolute difference ($A_{diff}\%$) was calculated as described in Equation 13,

$$A_{diff}\% = \left(\left(\frac{Sn_f}{T_f}\%\right) - \left(\frac{Sn_v}{T_v}\%\right)\right) \qquad \text{[Eq 13]}$$

where Sn_f is the functional capacity expressed as HEFml in segment n, T_f is the total liver functional capacity expressed as HEFml, Sn_v is the volume of segment n and T_v is the total liver volume. For every segment, the resulting $A_{diff}\%$ was a negative or positive value distributed around 0%. The relative function-to-volume discrepancy (R_{diff}) for each segment was calculated as expressed in Equation 14 resulting in values distributed around 1.

$$R_{diff} = \left(\frac{\left(\frac{Sn_f}{T_f}\%\right)}{\left(\frac{Sn_v}{T_v}\%\right)}\right) \qquad \text{[Eq 14]}$$

For example, if in a patient segment III contributed 14% total liver volume and 18% to total liver function, then $A_{diff}\%$=4 and R_{diff}=1.29.

3.4 MRC SCORING (PAPER III)

The MRCs for Paper III were evaluated by two observers, a senior consultant radiologist and a senior consultant hepatobiliary surgeon, and reported as consensus. The observers were blinded to the patients clinical parameters and outcome of the DHCE-MRI. The biliary tree, divided into the extrahepatic (CHD and CBD) and intrahepatic ducts (sectional and left and right hepatic ducts), were described and

Table 8: Scoring system for bile duct changes as observed on MRC

Score	Parameter
0	Normal, dilated or isolated stricture <50%
1	Isolated stricture ≥50% or diffuse stricturing
2	Beading
3	Non-visualization

graded as shown in Table 8. This system has previously been used in a scintigraphic study on segmental liver function and bile flow in PSC[124]. Due to the limitations of MRC in depicting fourth generation (segmental) intrahepatic bile ducts in PSC[189, 190], the segmental ducts were not included in these calculations. The bile flow path for each segment was described by adding the scores of the ducts representing the biliary flow path for the specific segment, resulting in a score representative of the total downstream biliary obstruction for that particular segment.

3.5 SIMULATIONS

3.5.1 Paper I: Deconvolution simulations

A numerical simulation comparing FA with appended tail (FA+tail) and TSVD for DA was performed. Ideal input and impulse functions were constructed from gamma variate functions [191]. Curve shapes as similar as possible to those acquired in vivo were achieved by constructing mean input and impulse curves from data obtained in the study, and fitting these with a sum of two gamma variate functions. The input and impulse functions were then convoluted to find the response function, as shown in Equation 2. Different amounts of normal-distributed noise were applied to the response and input function respectively, to simulate different levels of SNR. DA was then applied using the two different techniques. The appended tail in the FA+tail technique was set to be three times the length of the simulation data. The truncation threshold in the TSVD technique was fixed at c=0.07. Simulations were performed 1000 times for each SNR level. HEF was calculated as described above and standard deviations of the results for the two methods were calculated. Simulations were performed using in-house software written in MATLAB® (Mathworks, Michigan, USA).

3.5.2 Paper IV: Hepatectomy simulations

A left-sided hemihepatectomy (segments 2, 3 and 4) was simulated and post-operative remnant liver function (RLF) as predicted by global assessment and segmental assessment compared. This was done for 10 cirrhotic patients and 10 healthy volunteers. The RLF as predicted by an arbitrarily chosen global liver function test was calculated by deducting the percentage of the total hepatocyte extraction capacity (HEFml) equivalent to the percentage of the volume liver resected. For the simulation

of the RLF prediction based on segmental functional assessment, the HEFml of the remaining liver segments as calculated by DHCE-MRI were added. For example, if resection implied removal of 45% of the liver volume, the predicted RLF using global assessment was calculated as being 55% of the total liver function, whereas the measured function in HEFml of segments 1, 5, 6, 7, and 8 was added for the segmental DHCE-MRI-based prediction of RLF.

3.6 STATISTICAL ANALYSES

In all studies, STATA 10 (StataCorp, 4905 Lakeway Drive, College Station, Texas 77845 USA), was used for the statistical analyses. In Paper I, GraphPad Prism 5 (GraphPad Software INC, La Jolla, CA, USA) was used in addition to STATA 10. A two-sided significance threshold was set to $\alpha=0.05$ in all studies.

3.6.1 Paper I

Descriptive statistics were used for presentation of HEF and irBF. The study yielded 180 paired observations for HEF and irBF (20 subjects with 9 segmental registrations each and each subject analysed with both TSVD and FA+tail), and the median HEF and irBF for the two methods of DA were compared using the non-parametric Wilcoxon matched pairs test. The SD of HEF results from the two methods were compared using the variance ratio test (also known as the F-test).

3.6.2 Paper II

The results of the segmental calculations for quantitative and semi-quantitative parameters were presented as medians (with minimum and maximum) together with the global median for all studied parameters. Results were compared using the non-parametric Mann-Whitney U-test. For the parameters where a significant difference in global median was observed, test for trend across ordered groups was used to assess the association between the CPS and MELD-score and the specific parameter. For these calculations, the controls were assigned a dummy value of 4 for CPS, and 5 for the MELD-score. This is one unit less than the lowest possible score in these models. The Mayo risk score was regarded as a continuous variable and the Spearman rank correlation was used instead, without assigning a dummy value for the controls. In those parameters where a significant difference between groups in global median was seen, Spearman rank correlation was also used for correlating the specific parameter to age in the patient group. Likewise, using the Mann-Whitney u-test, the outcome of the same parameters in the control group was compared, using gender as the independent variable.

3.6.3 Papers III and IV

Descriptive statistics were used for presentation of the liver function parameters. The non-parametric Mann-Whitney U-test was used to compare results regarding the liver function parameters and liver volumes, since a normal distribution could not be assumed. When comparing the median HEF of the right and left liver lobes, the Wilcoxon matched-pairs test was used. The distribution of differences between segmental function and volume (Adiff% and Rdiff) for patients and controls was compared using the variance ratio test (F-test). Correlations between liver function

parameters and clinical scores, including the MRC scores in Paper III, were assessed using Spearman rank correlation. In Paper IV, receiver operating characteristic (ROC) analysis was used to identify the optimal discriminating cut-off levels for the liver function parameters.

4 RESULTS

4.1 RESULTS PAPER I

The result of the DA simulation is shown in Table 9 as a SD comparison. TSVD performed significantly better than FA+tail at almost all SNR levels, except at SNR levels 6 and 15.

Table 9: Result of the simulation comparing TSVD and FA+tail

SNR	TSVD SD[1]	FA+tail SD[1]	p-value[2]
6	0.116	0.122	p=0.059
8	0.087	0.100	***p<0.05***
10	0.070	0.078	***p<0.05***
12	0.060	0.067	***p<0.05***
15	0.050	0.051	p=0.27
20	0.035	0.039	***p<0.05***
25	0.027	0.030	***p<0.05***
30	0.024	0.026	***p<0.05***
35	0.020	0.022	***p<0.05***
40	0.018	0.020	***p<0.05***
45	0.016	0.017	***p<0.05***
50	0.014	0.016	***p<0.05***
70	0.010	0.011	***p<0.05***

[1)] n = 1000 in both groups; [2)] Variance ratio test

The mean ROI size was 31.9 (SD 21.6) voxels. Summary statistics of HEF and irBF with the two DA methods are shown in Table 10, and presented graphically in Figure 10, together with the distribution of HEF and irBF on the segmental level.

Table 10: Summary statistics for HEF and irBF

	HEF: TSVD	HEF: FA+tail		irBF: TSVD	irBF: FA+tail	
Mean	0.210	0.214		0.242	0.241	
Median	0.201	0.205	(p=0.086)[1]	0.240	0.239	(p=0.51)[1]
Minimum	0.088	0.081		0.143	0.150	
Maximum	0.443	0.446		0.333	0.351	
Range	0.355	0.365		0.189	0.201	
SD	0.0512	0.0572	(p=0.068)[2]	0.0430	0.0400	(p=0.84)[2]
CV	24.3%	26.7%		17.7%	16.6%	

1) Wilcoxon matched-pairs test 2) Variance ratio test
CV=coefficient of variation

There were no significant differences in the overall median values of HEF or irBF calculated with the two DA methods (p=0.086 for HEF and p=0.51 for irBF). However, TSVD yielded a smaller SD and CV, although the difference in SD was not statistically significant (p=0.068 for HEF and p=0.84 for irBF).

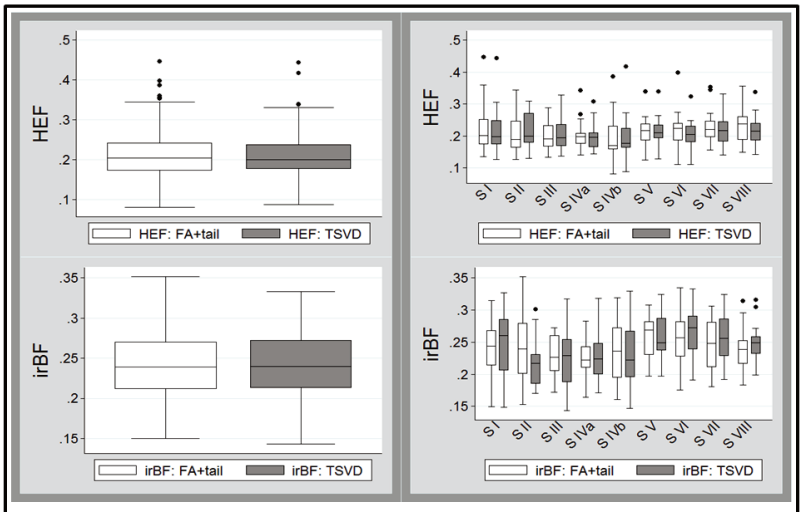

Figure 10: Overall (left) and segmental (right) distribution of HEF and irBF with the two methods for DA.

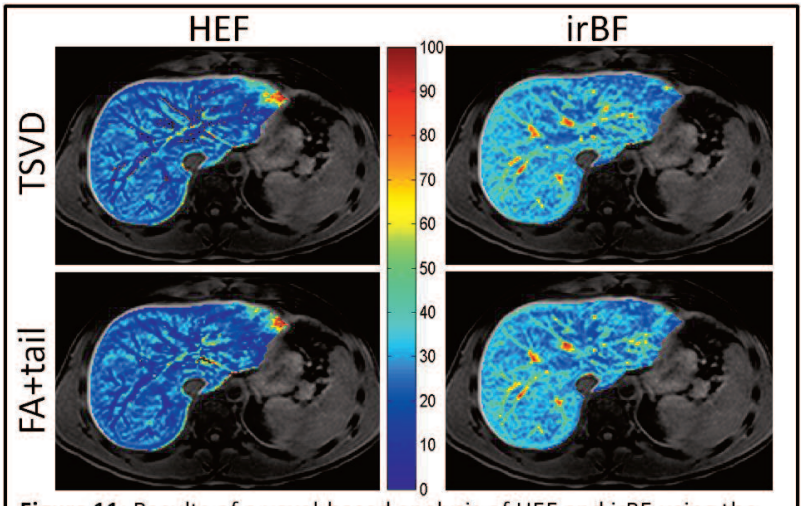

Figure 11: Results of a voxel-based analysis of HEF and irBF using the two methods for DA. Results are presented colour-coded and superimposed on anatomical images.

Parametric maps of HEF and irBF for a slice above the horizontal inter-segmental plane of the liver in one test subject are shown in Figure 11. HEF values above 0.7 and irBF above 1 were regarded as artefacts and excluded. HEF and irBF values are presented as percentages on a scale from 0 to 100%.

4.2 RESULTS PAPER II

The results for the PBC patients compared to the healthy control group regarding median levels of the quantitative functional parameters on a segmental and global level are presented in Table 11. In a majority of segments, median HEF and MTT measurements were significantly lower in PBC patients compared to healthy volunteers. This difference was also observed for the global medians regarding HEF and MTT. With the exception of one segment (IVa), no significant differences between the groups were found in segmental or global medians for irBF.

Table 11: Segmental and global median results for quantitative and semi-quantitative functional parameters

	HEF			**irBF**			**MTT (s)**		
	Controls	**PBC**	***p****	**Controls**	**PBC**	***p****	**Controls**	**PBC**	***p****
S I	0.18	0.16	p=0.14	0.26	0.27	p=0.59	486	368	p=0.06
S II	0.21	0.16	***p<0.05***	0.22	0.23	p=0.20	562	351	***p<0.05***
S III	0.19	0.14	p=0.07	0.23	0.23	p=0.61	494	393	p=0.16
S IVa	0.20	0.16	p=0.07	0.22	0.25	***p<0.05***	485	369	***p<0.05***
S IVb	0.17	0.15	p=0.11	0.22	0.25	p=0.08	524	369	***p<0.05***
S V	0.21	0.16	***p<0.05***	0.25	0.28	p=0.37	521	379	p=0.05
S VI	0.20	0.16	***p<0.05***	0.27	0.28	p=0.31	509	350	***p<0.05***
S VII	0.22	0.19	***p<0.05***	0.26	0.28	p=0.76	479	399	p=0.10
S VIII	0.22	0.17	***p<0.05***	0.25	0.25	p=0.31	536	350	***p<0.05***
Global	0.20	0.16	***p<0.05***	0.24	0.25	p=0.35	503	363	***p<0.05***
	C_{max}			**t_{max} (s)**			**$t_{1/2}$ (s)**		
	Controls	**PBC**	**p***	**Controls**	**PBC**	**p***	**Controls**	**PBC**	**p***
S I	0.533	0.581	p=0.41	1500	2400	***p<0.05***	12591	13305	p=0.57
S II	0.473	0.480	p=0.61	1950	1800	p=0.68	12858	15898	p=0.82
S III	0.451	0.455	p=0.79	1800	2400	p=0.08	11298	9062	p=0.63
S IVa	0.459	0.539	p=0.33	1230	2250	p=0.24	15491	13162	p=0.48
S IVb	0.448	0.526	p=0.12	1800	2550	p=0.07	14018	11902	p=0.96
S V	0.574	0.600	p=0.85	2100	2550	p=0.28	20609	13019	***p<0.05***
S VI	0.574	0.611	p=0.44	2100	2550	p=0.27	18595	22738	p=0.51
S VII	0.557	0.607	p=0.35	1950	2700	p=0.25	20755	15889	p=0.57
S VIII	0.553	0.555	p=0.70	2130	2100	p=0.80	23387	10773	***p<0.05***
Global	0.537	0.570	p=0.64	1950	2250	p=0.16	17697	14133	p=0.41

*Mann-Whitney U-test

The results for the semi-quantitative parameters are shown in Table 11. No significant differences were observed on the global level for any of these parameters. It was noted that the minimum value of t_{max} in the PBC group for all liver segments except segment I occurred as early as 120 s after injection of the tracer (not shown in Table 11). This means that the relative signal intensity in these segments peaked when the intravascular bolus of the tracer passed, and that very little tracer was subsequently extracted.

Since global medians of HEF and MTT, as well as medians for a majority of segmental values for these parameters differed significantly between the patient and control groups, further analyses were performed regarding the impact of disease severity on these parameters. As seen in Figure 12, MTT and HEF decreased significantly with increasing severity of liver disease as estimated with the CPS and MELD-score. There were no significant correlations between HEF and the Mayo risk score (Spearman´s rho = 0.242, p=0.448) or MTT and the Mayo risk score (Spearman´s rho = -0.32, p=0.308).

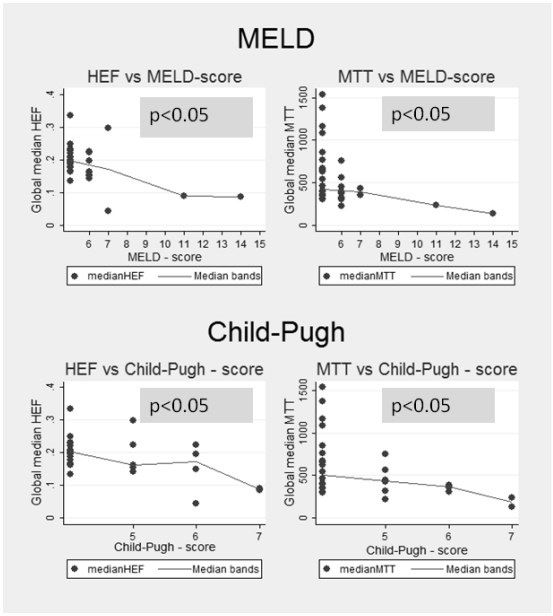

Figure 12: HEF and MTT plotted against MELD-score (above) and CPS (bottom), with both parameters showing a significant decreasing trend with increasing disease severity.

To assess whether age influenced the results in the patient group, HEF and MTT were correlated to age, but no significant associations were found (Spearman rho=0.242, p=0.45 and rho=0.344, p=0.27 respectively). In the control group, gender was not found to be a substantial confounder, since neither the median HEF, nor the median MTT for men and women differed significantly (p=0.11 and p=0.76, Mann-Whitney U-test).

4.3 RESULTS PAPER III

When calculating the DA-derived parameters in the PSC group, TSVD produced artefacts (as previously defined) in 22% of the voxels compared to 2% for the FA+tail method. Among controls, the corresponding numbers were 20% and 1% respectively. Due to these results, only data from the FA+tail method were used in the further analysis of the results. The failure rate for FA+tail did not differ significantly between patients and controls (p=0.17).

The relation between the quantitative functional parameters and liver volume measurements in patients and controls are shown in Table 12, where no statistically significant differences between the groups were found.

Table 12: Results of quantitative liver function and volume analysis

	Controls		**PSC patients**		
	Median	**(Min-Max)**	**Median**	**(Min-Max)**	**p-value***
Total liver volume (ml)	1496	(1037-1934)	1564	(1101-1800)	0.59
Total hepatocyte volume (ml)	1321	(958-1664)	1386	(985-1629)	0.31
HEFml (Total liver function)	289	(191-475)	270	(182-425)	0.85
Median global HEF	0.23	(0.16-0.29)	0.21	(0.09-0.29)	0.24
Median global irBF	0.52	(0.43-0.64)	0.48	(0.34-0.59)	0.07
Median global MTT	789	(483-2292)	596	(351-1109)	0.07

* Mann-Whitney U-test

A significantly larger variance for $A_{diff}\%$ (3.82 versus 0.66) and R_{diff} (0.032 versus 0.006) was noted among patients compared to controls ($p<0.05$ for both parameters), indicating a more non-homogeneous distribution of function in the liver parenchyma in the PSC group compared to healthy controls. The uneven distribution of function in one patient with segmental disease is illustrated in the parametric maps presented in Figure 13. This particular patient showed non-visualization of the sectional ducts to segments II-III-IVa-IVb, and also non-visualization of the left main hepatic duct.

The variations in function and volume inflicted by disease are also illustrated in Figure 14, where the function and volume of the right and left hemilivers in the two groups are presented.

Cholangiographic findings indicated diffuse intrahepatic disease in all patients and 8 (67%) patients had combined intra- and extrahepatic disease. The correlations between the cholangiographic findings and segmental functional parameters are displayed in Table 13. There was a statistically significant negative correlation between the added biliary scores and the segmental median HEF and irBF.

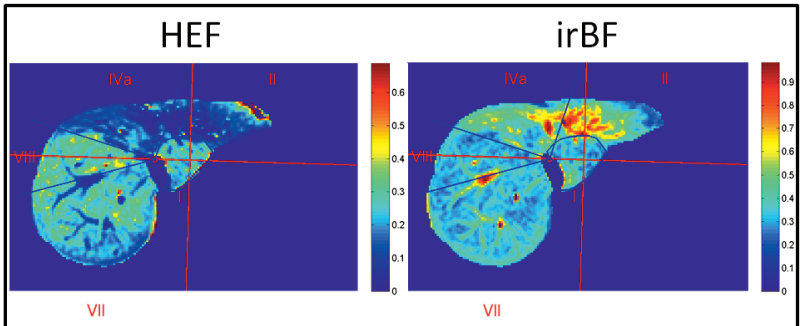

Figure 13: Parametric maps of function (HEF) and perfusion (irBF). Note the marked segmental differences between segments VII and VIII compared to segments IVa and II. Note also the sparing of segment I. In the representation of perfusion (right), the vascular structures are easily identified with a markedly higher irBF compared to parenchymal voxels.

Table 13: Correlation between clinical and cholangiographic scores and liver functional parameters

		Segmental median HEF	Segmental median irBF	Segmental median MTT
Sectional ducts	*rho*	-0.16	-0.16	0.01
	p	0.11	0.12	0.93
Main hepatic ducts (left & right)	*rho*	-0.21	-0.51	-0.20
	p	***<0.05***	***<0.05***	***<0.05***
CHD	*rho*	-0.20	-0.43	-0.34
	p	***<0.05***	***<0.05***	***<0.05***
CBD	*rho*	-0.04	-0.10	0.25
	p	0.72	0.31	***<0.05***
Sum of downstream obstruction (sectional to CBD)	*rho*	-0.24	-0.45	-0.07
	p	***<0.05***	***<0.05***	0.48

		HEFml	Global median HEF	Global median irBF	Global median MTT
Child-Pugh score	*rho*	0.02	-0.14	0.21	0.07
	p	0.96	0.67	0.52	0.83
MELD	*rho*	-0.03	-0.14	0.37	0.55
	p	0.92	0.67	0.24	0.06
Mayo risk score	*rho*	-0.85	-0.80	-0.68	-0.20
	p	***<0.05***	***<0.05***	***<0.05***	0.53

rho=Spearman rho, p=p-value

CHD=common hepatic duct
CBD=common bile duct

The correlations between the CPS, MELD and Mayo risk scores and global liver function parameters are presented in Table 13. A strong and significant negative correlation between the Mayo risk score and the total liver function expressed as HEFml, global median HEF and global median irBF was found. No significant correlation between Mayo risk score and global median MTT was found, nor were there any significant correlations between the global liver function parameters and the CPS and MELD-scores.

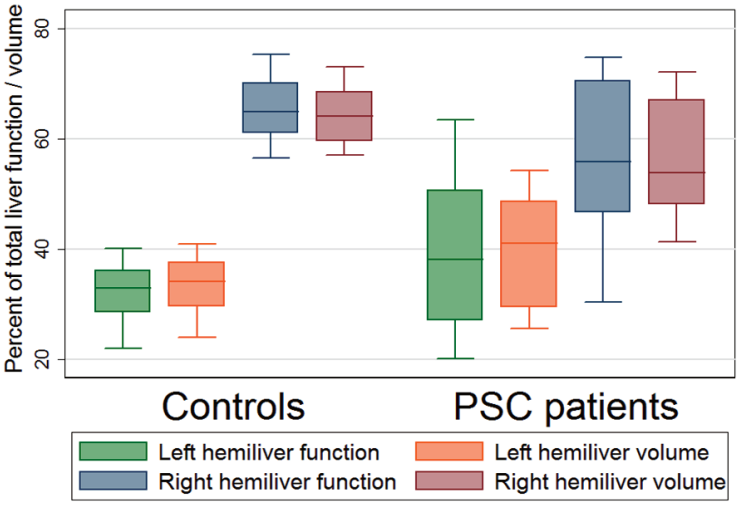

Figure 14: Distribution of function and volume in the right and left hemilivers, showing marked differences between the groups.

4.4 RESULTS PAPER IV

The results of liver volume measurements and functional parameters in the two groups are shown in Table 14. There were no significant differences regarding total liver volume, but when vascular voxels were subtracted, the patient group had a significantly larger parenchymal volume, despite the fact that the overall parenchymal function expressed in HEFml was significantly lower. Also, the median liver HEF was significantly lower among patients, indicating lower parenchymal functional capacity per volume unit. The median MTT was significantly shorter in the patient group but perfusion assessed as irBF did not differ significantly between the groups. The semi-quantitative parameter LSER was also significantly lower in the patient group at all studied time-points as illustrated in Figure 15, where the results are presented according to Child-Pugh class, and compared to controls.

Table 14: Results of liver function and volume analysis

	Controls		**Patients**		
	Median	*(min-max)*	**Median**	*(min-max)*	**p-value***
Total liver volume (ml)	1496	*(1037-1934)*	1577	*(1357-1886)*	p=0.29
Parenchymal volume (ml)	1256	*(915-1692)*	1435	*(1225-1774)*	***p<0.05***
Total functional capacity (HEFml)	283	*(112-412)*	171	*(53-341)*	***p<0.05***
Global median HEF	0.22	*(0.11-0.28)*	0.09	*(0.02-0.20)*	***p<0.05***
Global median irBF	0.52	*(0.43-0.63)*	0.48	*(0.31-0.74)*	p=0.17
Global median MTT	789	*(477-1318)*	453	*(203-686)*	***p<0.05***
LSER (10min)	2.3	*(1.5-3.1)*	1.3	*(0.8-1.6)*	***p<0.05***
LSER (20min)	3.4	*(2.4-5.0)*	1.8	*(1.0-2.6)*	***p<0.05***
LSER (30min)	5.7	*(4.0-24.6)*	2.0	*(1.2-3.3)*	***p<0.05***
LSER (45min)	7.2	*(3.1-18.8)*	2.4	*(1.3-4.2)*	***p<0.05***

*=Mann-Whitney U-test; LSER=liver-spleen enhancement ratio at corresponding time-points

Table 15 displays the correlations between the liver function parameters obtained and liver disease grade as assessed by the CPS and MELD-score. Total liver functional capacity, median HEF, irBF and LSER at all studied time-points had significant correlations with the CPS. The MELD-score had negative and significant correlations with total liver function, median HEF and LSER at 45 min, but the LSER at the other time-points did not correlate with MELD. MTT did not correlate significantly with the scoring models used in this study.

The distributions of absolute and relative differences (A_{diff}% and R_{diff}) in segmental function and volume of the two groups differed significantly with a larger variance for A_{diff}% (7.1 vs. 0.61) and R_{diff} (0.052 vs. 0.006) among patients compared to controls ($p<0.05$ for both parameters). The distributions are presented in Figure 16.

Table 15: Correlation of scoring models and liver function parameters

	CPS		MELD	
	Spearman rho	**p-value**	**Spearman rho**	**p-value**
Total functional capacity (HEFml)	-0.72	***p<0.05***	-0.76	***p<0.05***
Global median HEF	-0.80	***p<0.05***	-0.73	***p<0.05***
Global median irBF	0.76	***p<0.05***	0.55	*p=0.10*
Global median MTT	-0.26	*p=0.46*	0.05	*p=0.88*
LSER (10min)	-0.74	***p<0.05***	-0.58	*p=0.10*
LSER (20min)	-0.76	***p<0.05***	-0.63	*p=0.07*
LSER (30min)	-0.72	***p<0.05***	-0.55	*p=0.12*
LSER (45min)	-0.79	***p<0.05***	-0.75	***p<0.05***

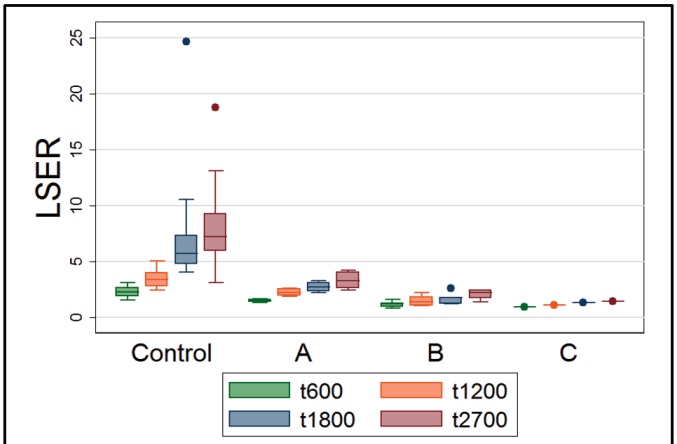

Figure 15: The LSER at four different time-points in the control group and in Child-Pugh class A, B and C.

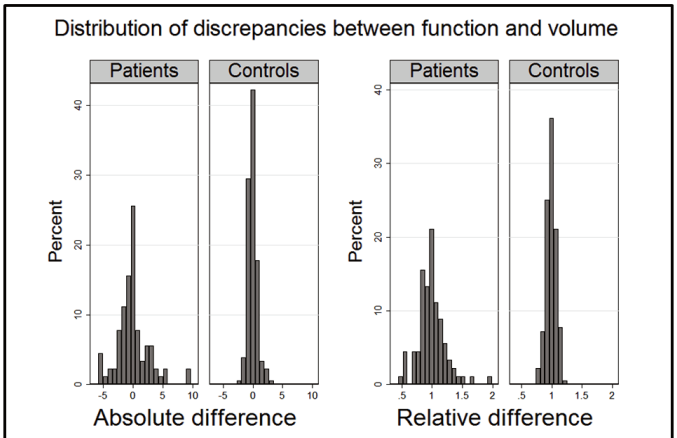

Figure 16: Histograms showing the distribution of A_{diff}% (left) and R_{diff} (right), indicating inhomogeneous liver function in the cirrhosis group.

The results of the simulated hemi-hepatectomy are presented in Table 16. Global liver function assessment overestimated the remnant liver function in 9 out of 10 patients by as much as 9.3% in absolute numbers (median -3.5% (range -9.3–3.5%)).

Table 16: Results of simulated left-sided hemihepatectomy

Patient / CPC	**1A**	**2A**	**3B**	**4A**	**5B**	**6B**	**7C**	**8A**	**9B**	**10B**
Total liver function (HEFml)	341	210	174	330	82	169	115	262	53	168
Volume of resection (%)	55	52	46	37	56	51	48	46	45	30
Predicted RLF (HEFml)	155	102	93	208	36	83	60	142	29	118
Actual RLF (HEFml)	142	94	93	220	29	69	57	140	27	115
Predicted RLF (%)	45.4	48.5	53.6	63.1	44.4	49.3	52.4	54.3	54.7	70.3
Actual RLF (%)	41.6	44.7	53.3	66.6	35.2	40.8	50.0	53.5	50.6	68.6
Difference (actual-predicted)	*-3.8*	*-3.8*	*-0.3*	*3.5*	*-9.3*	*-8.5*	*-2.4*	*-0.8*	*-4.1*	*-1.7*
Control	**1**	**2**	**3**	**4**	**5**	**6**	**7**	**8**	**9**	**10**
Total liver function (HEFml)	229	266	353	269	383	219	215	381	260	345
Volume of resection (%)	40	26	37	35	28	38	32	32	37	31
Predicted RLF (HEFml)	138	196	220	175	274	137	146	258	165	239
Actual RLF (HEFml)	139	201	228	178	275	139	149	259	171	236
Predicted RLF (%)	60.2	73.8	62.5	64.9	71.5	62.4	67.7	67.7	63.2	69.3
Actual RLF (%)	60.8	75.7	64.6	66.0	71.8	63.2	69.5	67.9	65.7	68.5
Difference (actual-predicted)	*0.6*	*1.9*	*2.1*	*1.2*	*0.3*	*0.8*	*1.8*	*0.2*	*2.5*	*-0.7*

CPC = Child-Pugh class RLF = remnant liver function

The cut-off levels and their ability to discriminate between patients and controls in this study are presented in Table 17 with generally good or excellent accuracy for all the studied parameters.

Table 17: ROC analysis

Controls and Child Pugh A versus Child Pugh B and C

	AUROC	Cut-off	Sensitivity	Specificity	Accuracy	LR+	LR-
Liver function (HEFml)	0.97	209	95.8%	100.0%	96.7%		0.04
Global median HEF	1	0.11	100.0%	100.0%	100.0%		
LSER 10	0.97	1.31	100.0%	83.3%	96.7%	6.00	
LSER 20	0.99	1.88	100.0%	83.3%	96.7%	6.00	
LSER30	0.99	2.22	100.0%	83.3%	96.7%	6.00	
LSER 45	1	2.43	100.0%	100.0%	100.0%		

Controls versus patient group

	AUROC	Cut-off	Sensitivity	Specificity	Accuracy	LR+	LR-
Liver function (HEFml)	0.79	215	90.0%	70.0%	83.3%	3.00	0.14
Global median HEF	0.94	0.18	95.0%	80.0%	90.0%	4.75	0.06
LSER 10	0.99	1.67	95.0%	100.0%	96.7%		0.05
LSER 20	0.98	2.48	95.0%	90.0%	93.3%	9.50	0.06
LSER 30	1	4.01	100.0%	100.0%	100.0%		
LSER 45	0.98	4.63	90.0%	100.0%	93.1%		0.10

AUROC= area under receiver operator characteristic curve

5 DISCUSSION

This thesis presents the concept of an imaging-based liver function test with a hepatocyte-specific MRI contrast agent as tracer, and dynamic MRI as the sampling tool. The tracer used, Gd-EOB-DTPA or gadoxetic acid, is actively taken up by functioning hepatocytes through the OATP and NTCP enzyme systems. This is a property shared at least in part with ICG and the IDA compounds currently used in clinical practice for assessing liver function. Conceptually, the uptake of Gd-EOB-DTPA into the hepatocyte should therefore correspond to the same aspects of liver function that can be assessed by ICG clearance and functional HBS. That the uptake of Gd-EOB-DTPA actually reflects aspects of liver function has been shown in several previous studies, both in human and animal subjects[167, 178-188, 192, 193].

In this work, a method is proposed where the sampling of contrast agent concentrations is done in the blood pool and liver parenchyma. The resulting SI_r-curves are used to quantify tracer kinetics for assessment of regional and global liver perfusion and hepatocellular tracer extraction capacity. It utilizes the concept of DA to correct the liver parenchymal enhancement response for the constantly changing concentration of tracer in the inflow to the liver. DA has earlier been described as a tool for quantification of tracer kinetics in quantitative studies of the brain and kidney, as well as in scintigraphic assessment of liver function[117, 121, 138, 139, 142, 144, 145, 147, 148, 194-197]. There is only one previously published animal study where MRI and DA were used to assess the hepatic uptake of Gd-EOB-DTPA.[180].

The studies presented here show that DHCE-MRI with or without DA can be used in human subjects to calculate several liver function parameters on both a global and segmental level, as well as global and segmental liver volumes.

Traditional semi-quantitative parameters (C_{max}, t_{max}, $t_{1/2}$) were found to be of limited value and they failed to distinguish patients from normal volunteers. Being easily accessible, without the need for advanced post-processing for calculation, they are often used to describe the pharmacokinetic properties of a system. These parameters are perhaps more intuitive and more easily understood than the DA-derived parameters, but they have to be interpreted with caution. A high C_{max} is usually regarded as a good extraction capacity of the parenchyma, but can also be the result of virtually non-functioning liver parenchyma with arterialization due to cirrhosis or inflammation and a quick and high vascular peak. Furthermore, failure to transport a test substrate into the bile canaliculi or stasis in the intrahepatic bile ducts might also give a high C_{max}, giving the notion of a well-functioning parenchyma. A short $t_{1/2}$, calculated from a time-enhancement curve generated by a parenchymal ROI or voxel is generally interpreted as good tracer excretion. However, in parenchyma with no extraction capacity, where the tracer-derived signal is mainly from the intrahepatic blood pool, a short $t_{1/2}$ will be observed if the serum half-life of the tracer is short. Furthermore, a long $t_{1/2}$ that generally would be interpreted as decreased parenchymal function could be the result of activity measured in obstructed bile ducts or intracellular sequestration of tracer in a patient with normal tracer uptake but abnormal biliary excretion.

With liver segmentation and a voxel-based approach, segmental results for HEF, irBF and MTT, as well as total parenchymal and segmental liver volumes could be calculated. Furthermore, both the total hepatic and segmental extraction capacities of Gd-EOB-DTPA assessed in HEFml could be obtained. The lower HEF and HEFml observed in PBC and cirrhotics compared to the healthy controls can be explained either by a reduced functional hepatocyte mass or hepatocytes with less capacity to transport Gd-EOB-DTPA across the hepatocyte membrane. The shorter MTT seen among cirrhotics and in the PBC group is probably due to a lower hepatic extraction and a larger proportion of the tracer being washed out of the system through the vascular outflow. In healthy livers, the MTT is probably longer due to uptake into hepatocytes, intracellular transport and subsequent biliary excretion, a process that doubtless is more time-consuming. There were no significant differences regarding irBF between controls and patients with PBC, PSC or cirrhosis. The significant positive correlation between irBF and CPS observed in cirrhotics could possibly be the result of increasing arterialization of perfusion in cirrhotic parenchyma, known to increase with increasing disease severity[198]. Conversely, irBF showed a significant negative correlation with the Mayo risk score in PSC patients.

Total segmental "downstream" bile duct obstruction as defined by the scoring system used was also found to negatively correlate with HEF and irBF, but not with MTT. This finding indicates that segments with a more pronounced biliary stasis had less extraction capacity and thus less function as defined by this method. This finding also replicates earlier findings from scintigraphic studies on biliary obstruction in PSC where the same scoring system was used, but segmental liver function was semi-quantitatively assessed[124]. On a total liver level it has been shown that uptake of Gd-EOB-DTPA is impaired in patients with impaired liver function[167, 183-188]. This work suggests that DHCE-MRI also has the capability to detect segmental variations in function.

The ROC analysis performed in cirrhotics yielded cut-off values for total liver function, median HEF and median LSER at all time-points that showed good to excellent accuracy regarding separation of the groups in the analysis. It was possible both to distinguish controls from the entire patient group, as well as patients with severely impaired liver function (CPC B and C) from those with normal or mild liver disease (controls and CPC A). The rationale behind this latter way to categorize the groups was that the life expectancy in CPC A is marginally less than in healthy controls, whereas in CPC B and C it is markedly worse.

In the fourth study the less computationally demanding semi-quantitative parameter LSER was also studied, and it was shown to differ significantly between controls and the cirrhosis group. LSER at all studied time points correlated with CPS, and performed well in the ROC analysis. It should be noted that a significant difference in LSER was evident as early as 10 minutes post contrast injection.

5.1 DISTRIBUTION OF LIVER FUNCTION

There is ample data showing that liver function is heterogeneously distributed within the liver, both in healthy as well as in diseased parenchyma. This work supports these earlier results.

5.1.1 Normal liver

Scintigraphic studies assessing liver function have suggested an inherently different uptake capacity of tracers in the left and right hemilivers in healthy subjects, a finding that was replicated in this work[199, 200]. When using voxel-based analysis, the median HEF for the left and right hemiliver voxels among healthy controls was 0.21 and 0.23 respectively, which was statistically significant ($p<0.05$). This difference was also observed in the ROI-based analysis of Paper I (results not shown). Also presented here are the RE/time-curves- (equivalent to SI_r/time curves) of the individual segments for the healthy volunteers of Paper I, showing a substantial difference in the uptake pattern of Gd-EOB-DTPA between the left (S II, III, IV) and right hemilivers (S V, VI, VII, VIII).

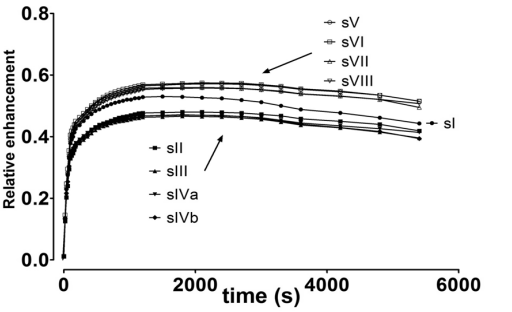

Figure 17: RE/time-curves from each liver segment for the 20 healthy volunteers. Note the difference between the segments of the left and right hemilivers, and segment I.

5.1.2 Diseased liver

In case of liver parenchyma being affected by disease, the situation regarding distribution of function might be even more complex. Histopathological studies of liver biopsies from diseased parenchyma have repeatedly shown non-homogeneous distribution of disease, be it fibrosis, cirrhosis, steatohepatitis or steatosis[34, 35, 201-204]. Several studies where HBS with IDA and GSA were used to evaluate regional liver function have confirmed that not only are histopathologic findings variable within the liver but as could be expected, function also seems to be non-homogeneously distributed[120, 124, 205-208]. It is also well-known that the cirrhotic liver parenchyma undergoes morphologic changes with hypertrophy of the left hemiliver and caudate lobe, and hypotrophy of the right hemiliver. Using ^{99m}Tc-GSA, Matsuzaki et al found that in liver cirrhosis the parenchyma of the left hemiliver seems to be less functionally affected by injury with a more preserved function per volume unit compared to the right hemiliver[207].

The results of the voxel-based analysis of liver function in PSC and cirrhotics confirmed these earlier findings of significantly more heterogeneous distribution of liver function in patients with liver disease, and a relative hypertrophy of the left hemiliver. Furthermore, in the cirrhosis group median HEF was found to be higher in the left liver (0.08 for the right liver and 0.11 in the left ($p=0.06$)), suggesting that the

quality of the hypertrophied left liver is slightly superior to that of the right, replicating the findings of Matsuzaki et al[207].

In healthy controls, the left hemiliver accounted for approximately 34% of the volume and 33% of the function, and the right hemiliver accounted for 64% of the volume and 65% of the function, with volume and function being quite closely related. In this situation with normal liver parenchyma, prediction of post-operative RLF using a segmental liver function test probably offers no major advantage compared to the current clinical practice of using a combination of volumetry and a global liver function test. In our simulation of a left-sided hemihepatectomy in this group of healthy controls, the differences in predicted liver function were negligible.

In patients with diseased liver parenchyma the situation is different. Global liver function tests, such as ICG clearance or the LiMax test cannot account for regional differences in liver function, making prediction of postoperative RLF of diseased liver parenchyma uncertain. This was also shown to be the case in this work when a left hemihepatectomy was simulated. The observed maximum difference between predicted and actual remnant liver function assessed with DHCE-MRI was 9.3%. If this had been a real case and these figures were true, such an error in prediction could be the difference between an uneventful postoperative course and postoperative liver failure with a possible fatal outcome.

5.2 LIMITATIONS AND ARTEFACTS

5.2.1 Study subjects

5.2.1.1 Controls

The same control group was used in all studies. The images were re-analyzed and the DHCE-MRI derived parameters were recalculated for each study as described in the Materials and Methods sections. No quantitative liver function test was performed to confirm normal liver function. However, none of the participants had a history of hepatobiliary disease, liver surgery or overconsumption of alcohol, and no abnormal serum LFTs were detected. One can therefore with reasonable confidence conclude that the reference group consists of subjects with liver function that can be regarded as normal.

One concern regarding the DHCE-MRI derived quantitative liver function parameters studied is the relatively large range in the results that was observed among healthy controls. The variation was substantial both intra- and interindividually, which in part could reflect actual inter-individual differences in the hepatic elimination capacity of Gd-EOB-DTPA, since it is known that hepatic elimination of pharmacological agents has a large variation even among healthy individuals[190]. In addition, inter-individual variation in ICG clearance among healthy individuals has been shown to be substantial, and since Gd-EOB-DTPA and ICG to some extent have the same hepatocellular uptake mechanism, this normal inter-individual variation could also be the case for Gd-EOB-DTPA[96, 209]. Furthermore, differences in diet or other life-style related factors prior to the examination could have influenced the results. Adjustments for confounders such as age, gender or body weight were not made, but previous studies of biliary excretion of

Gd-EOB-DTPA have not found age, gender or BMI to significantly influence the hepatobiliary transit time of Gd-EOB-DTPA[210]. The intra-individual variation is probably to a substantial extent also due to imaging-related artefacts and imperfections in the method, as will be further discussed.

5.2.1.2 Patients

Patients with PBC, PSC and alcohol- and/or HCV-induced cirrhosis were used to study the effects of chronic and segmental liver disease on the outcome of DHCE-MRI. In all studies, the numbers of participating patients were relatively low, and especially scarce were patients with advanced disease. Both PBC and PSC are relatively rare diseases and patients with advanced disease generally undergo liver transplantation. In the PBC and PSC groups, designated scoring models were used to stage liver disease, but also the CPS and MELD-scores. The latter two have been shown to be of no prognostic value when applied in the absence of cirrhosis, and it is not clear how many of the participants had histological signs of cirrhosis, since no biopsies were performed. The usefulness and accuracy of the MELD and CPS in this setting can therefore be questioned.

A major limitation in this work is that liver function was not quantitatively assessed using a reference method in the participating patients. Even though no particular test stands out as a generally accepted golden standard, ICG clearance is widely used and studied, especially in the context of liver surgery and is perhaps as close to a golden standard as one can get today. An obvious step will be to include ICG clearance or another quantitative liver function test in future studies applying DHCE-MRI.

5.2.2 Image acquisition and parameter calculations

5.2.2.1 Segmentation

The way in which the liver was divided into segments in this work followed the generally accepted anatomical landmarks for segmentation. Defining segmental volumes by the drawing of straight lines through the liver volume is a method that could be regarded as crude. Segmentation using the actual vascular territories of the portal vein by following the division of its branches in the liver parenchyma gives a more functionally correct segmentation of the liver. Such a method has been developed by Fraunhofer MEVIS (Bremen, Germany)[211]. An example where the Fraunhofer MEVIS method to define the liver segments has been applied to dynamic acquisitions from this work is presented in Figure 18. The combination of this method for segmentation

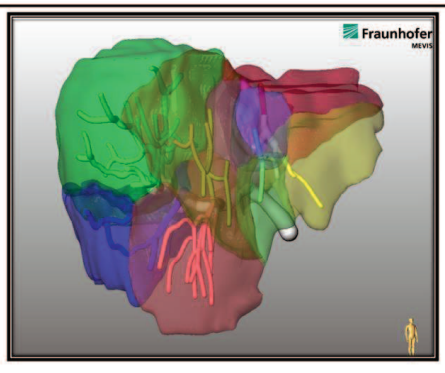

Figure 18: The liver segments as defined by the actual portal vein branching (published with kind permission from Fraunhofer MEVIS).

together with a method for voxel-based liver function analysis could give a more realistic estimation of segmental volumes and function, and possibly more accurately predict postoperative RLF, if applied in the preoperative evaluation of candidates for liver surgery.

5.2.2.2 Motion artefacts

In dynamic imaging-based studies of abdominal organs, motion artefacts are known to be a challenge, mainly due to breathing. These artefacts can be reduced by acquisitions being obtained during breath-hold, or by using a way of triggering of the scanner so that images are always obtained at the same time-point in the respiratory cycle. In this work patient motion in the MRI scanner over time and inability of the participating subjects to hold their breath at exactly the same depth during each acquisition could have induced substantial artefacts in the images obtained. Motion artefacts were indeed noted, which could have the effect that a ROI placed in the parenchyma in one of the acquired volumes may not represent liver parenchyma in the volumes acquired at other time-points. Of course this is true also in a voxel-based analysis, and it is evident that motion artefacts will impact the results of the quantitative analysis. The use of triggering devices or post-processing with image registration algorithms for motion correction is a logical next step in the pursuit of improving the method and stability of the results.

5.2.2.3 Partial volume effects

Some of the variations in the functional parameters described in this work could be attributed to what is known as partial volume effects. Even though individual voxels are small, they will inevitably include varying volumes of non-hepatocyte tissue. Conceptually, a ROI or voxel containing a higher proportion of vessels would yield a higher irBF due to higher perfusion and a lower HEF since extraction only takes place in hepatocytes. The reverse would be the case in a voxel or ROI containing a higher proportion of hepatocytes. This is illustrated in Figure 19 showing the ROI results from Paper I (TSVD derived), where HEF is plotted as a function of irBF (dotted lines denote the 95% confidence interval). A significant linear relationship between these parameters was observed.

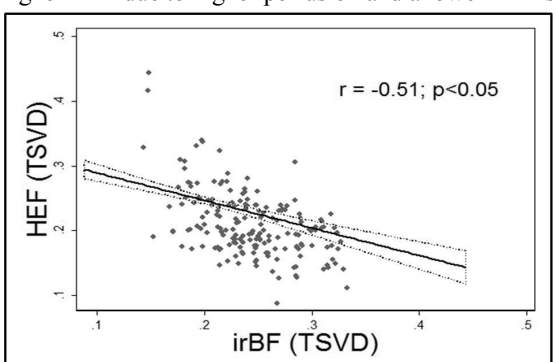

Figure 19: HEF plotted as a function of irBF, showing a significant negative association, probably explained by partial volume effects.

In an attempt to reduce the influence of partial volume effects, ROIs were placed avoiding major vascular structures and bile ducts as far as possible. In the voxel-based analysis, voxels with irBF above a user-defined threshold were omitted from analysis since they were regarded as mainly representing vascular tissue.

5.2.2.4 Choice of input function

In studies where DA is applied, a well-defined and accurate input function is crucial for obtaining reliable results. As previously mentioned, the liver has a dual vascular supply with venous inflow from the portal vein contributing approximately 75% and arterial blood from the hepatic artery contributing the remaining 25%. In principle, an input function should be defined close to the organ studied. In the case of the liver, ideally a dual input function model representing the dual arterial and venous inflow should be used. The placement of the input function ROI is usually done manually, making it user or observer dependent, adding a factor of subjective decision-making to the method. Ideally, the input function should be automatically defined in the images, thereby eliminating a source of bias.

In the first two studies, a ROI in the hilar part of the portal vein was used to define the input function. In terms of vascular flow a portal vein input function is more representative of the inflow of tracer than a ROI in the hepatic artery. Furthermore, the motion artefacts and limited image resolution in the studies made it impossible to define the hepatic artery in images other than the one or two acquired during the arterial phase. The aorta was not used to define the input function for two reasons. The first reason was that since the images were obtained in the transverse plane, inflow artefacts would have affected the input function. The second reason was that the short arterial peak with the first passage of contrast bolus would not have been optimally assessed with the temporal resolution used. This could have resulted in disturbing differences between subjects regarding maximum peak values in the input functions obtained. The portal inflow peak is somewhat more dispersed over time and the differences in the peak values observed were small. In the case of liver assessment, there is probably an advantage in using the portal vein, since the portal vein blood-flow is slower and with a direction in the x, y and z magnetic gradient field that makes it less susceptible to inflow artefacts compared to the aortic blood flow. A further disadvantage of using a hepatic artery input function is that approximately 50% of the arterial inflow of blood does not reach the hepatocytes, but rather supply the biliary tree with oxygenated blood, with a venous drainage into the hepatic veins and not the sinusoidal system[26].

In Papers III and IV the input function was defined by a ROI placed in the spleen. The strategy of using the spleen has shown an increase in the stability of the input function in conventional DCE-MRI using extracellular contrast agents [212]. This is most likely due to the fact that the spleen is substantially larger and less prone to respiratory and patient movement artefacts compared to the portal vein. There might even be a physiological advantage in using the spleen to define the input function in DHCE-MRI. In the majority of subjects the spleen and the liver both receive their arterial supply from the celiac trunc [20, 213]. Furthermore, the venous drainage of the spleen contributes significantly to the portal flow. Although not a perfect model, the spleen might to some extent represent the dual arterial and venous components of the blood supply to the liver. A theoretical disadvantage with this approach could be the effects on splenic blood flow from subclinical or manifest portal hypertension that could possibly influence the input function when patients with chronic liver disease are examined, and this method would also obviously not be possible in patients after splenectomy.

5.2.2.5 Signal intensity and contrast agent concentration

Many would argue that the use of the words "quantitative liver function analysis with MRI" is a contradiction of terms, since the signal that generates images in MRI is inherently non-quantitative but rather relative. For example, the same concentration of Gd-EOB-DTPA in liver and blood will result in different signal intensities due to inherently different native T1 of these tissues, as well as different r_1 for Gd-EOB-DTPA in blood and liver as previously described. For example, native T1 in liver has been reported to be 586 ms, T1 in the spleen 1057 ms and in blood 1262 ms[214, 215]. The signal intensity in a T1-weighted pulse sequence is proportional to the longitudinal relaxation rate (R_1) that is given by Equation 15, where T10 denotes the native pre-contrast T1 in the tissue:

$$R_1 = \frac{1}{T_1} = \frac{1}{T_{10}} + r_1[Gd] \qquad \text{[Eq 15]}$$

From this equation and the T10 and r_1 values from the literature previously described, the T1, at increasing concentrations of Gd-EOB-DTPA in blood, liver and spleen, can be calculated as shown in Figure 20. The maximum concentration in this figure, 0.12 mmol/L (mM), is the theoretical maximum plasma concentration in vivo, if the usual clinical dose of 0.1 ml/kg of Gd-EOB-DTPA with the concentration 0.25 mmol/ml is administered, and the distribution volume is 0.21 L/kg. As illustrated, T1 in the different tissues is not the same at equivalent concentration of Gd-EOB-DTPA, and therefore R_1 and signal intensity will not be the same either. Signal intensity in a T1-weighted steady-state spoiled gradient-echo pulse sequence can be calculated using Equation 16:

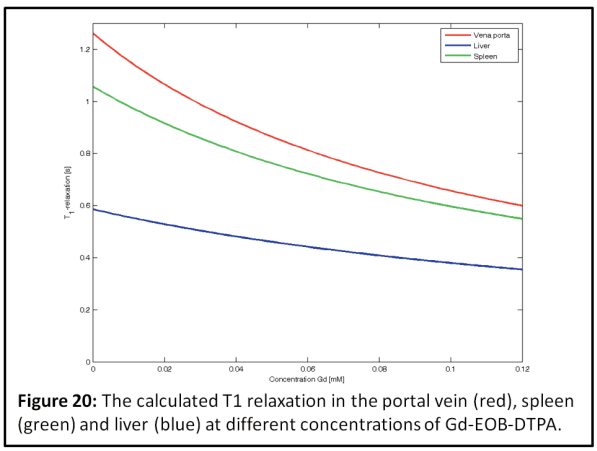

Figure 20: The calculated T1 relaxation in the portal vein (red), spleen (green) and liver (blue) at different concentrations of Gd-EOB-DTPA.

$$S(t) = S_0 \frac{(1-e^{-R(t)TR})\sin(\alpha)}{1-e^{-R(t)TR}\cos(\alpha)} \qquad \text{[Eq 16]}$$

where *S(t)* is the signal at time *t*, S_0 is the signal intensity from the fully relaxed system, *TR* is the repetition time and α is the flip angle. *R(t)* is the relaxation rate at time *t*, given that the concentration of tracer can be seen as a function of time, which is the case in dynamic MRI with Gd-based tracers. In this work, the concentration of Gd-EOB-DTPA in a voxel or ROI was assumed to be proportional to the SI_r as described in Equation 10. It has been shown that the relationship between signal intensity and contrast agent concentration is non-linear for gradient-echo pulse sequences used in T1-weighted imaging. However, when T1-relaxation is within the range of 40 ms to 2600 ms, the MRI signal using Gd-DTPA was shown to increase approximately

exponentially with shortened T1-relaxation[216]. Given the data from Figure 20, it can be assumed that T1 in all acquisitions in this work were within this range, making Equation 10 a reasonable approximation of contrast agent concentration. In this work the logarithmic relationship of Equation 9 was used to calculate the SI_r as a surrogate for contrast agent concentration. In many studies the relationship between pre- and post-contrast signal intensity and contrast agent concentration is instead calculated as described in Equation 17:

$$SI_r = \frac{(S_{(t)} - S_{(0)})}{S_{(0)}} \qquad \text{[Eq 17]}$$

Equations 16 and 9 and Equations 16 and 17 in combination can be used to calculate the SI_r as a function of the concentration of Gd-EOB-DTPA in liver, spleen and blood, as shown in Figure 21.

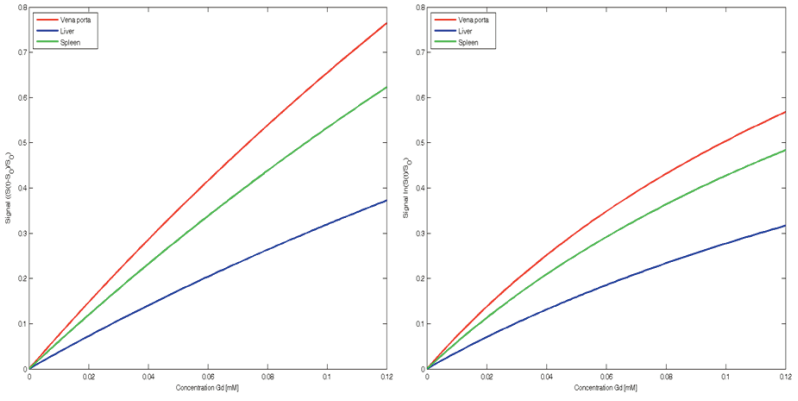

Figure 21: The graphs illustrate the relative signal intensity (SI_r)as a function of Gd-EOB-DTPA concentration (0 mmol/ml to 0.25 mmol/ml) in different tissues (portal vein (red), liver (blue) and spleen (green)). In the left, SI_r is calculated as $SI_r=((S_{(t)}-S_{(0)})/S_{(0)})$ and the right graph illustrates the method used in this work, $SI_r=\ln(S_{(t)}/S_{(0)})$.

From this figure it can be assumed that the method chosen for this work (Equation 9) probably makes the relationship between contrast agent concentration and SI_r slightly less linear than Equation 17. On the other hand, the difference in SI_r for the same concentrations of tracer in different tissues of interest seems to be slightly less.

5.2.2.6 DA-related matters

The high failure rate of the TSVD method for DA in Papers III and IV seemingly contradicts the results from the simulations described in Paper I. Based on this paper DHCE-MRI using TSVD was regarded as the preferred method due to superior stability of the simulation results compared to the FA, and for being less computationally demanding. In that context, only standard deviations and not the

failure rates were assessed. In this material as a whole, FA+tail turned out to be superior to TSVD for DA in vivo.

A static truncation threshold of c=0.07 was used in all deconvolutions where TSVD was applied. This threshold was arbitrarily chosen, but when other thresholds were applied, a larger variance was noted (unpublished material) and therefore the original threshold was used in the further studies. There are studies discussing the use of an automatically defined threshold, c, which has been shown to improve the performance of TSVD when used to assess brain perfusion[196, 217].

5.2.2.7 Acquisition time-frame

The research protocol used in the first three studies was primarily designed to examine the liver enhancement well into the excretory phase of the contrast agent. Therefore an investigation time of at least 90 minutes was needed. Such a time-frame for image acquisition makes the method unpractical in terms of logistics and from a patient point of view. However, the mathematical model (DA) used to calculate the functional parameters only uses acquisitions obtained during the first 30 minutes (420-1800s). Therefore, the protocol in Paper IV was shortened to a total sampling time of 45 minutes. Further shortening of the protocol seems feasible and a preliminary estimation is that a dynamic acquisition time of 30 minutes should suffice. If only the LSER is to be calculated, findings in this work indicate that image acquisition after 10 minutes is sufficient to detect differences between healthy controls and cirrhotic patients. Whether this is the case also in patients with mild chronic liver disease has not been evaluated in this work. One can note that imaging after 10-15 minutes, i.e. the hepatobiliary phase, is a common procedure in clinical practice when Gd-EOB-DTPA is used as the tracer. At this time-point sufficient tracer has usually been extracted by the liver parenchyma to allow characterization between lesions containing functioning hepatocytes and those that are devoid of hepatocellular function and tracer uptake.

5.2.2.8 Pulse sequence and choice of tracer

The pulse sequence used in the presented studies is a volumetric heavily T1-weighted standard clinical gradient-echo pulse sequence called THRIVE® (Philips), which was introduced in 2003. There are other commercially available pulse sequences from other manufacturers with similar performance, such as FAME®, LAVA® (GE Healthcare) and VIBE® (Siemens). Since the start of this project there has been further development in image acquisition techniques, and there are now pulse sequences with even faster volume acquisition available. The use of a more up-to-date pulse sequence would probably allow for better temporal and/or spatial resolution in the acquired volumes than was obtained in this work.

There are other hepatocyte-specific contrast agents for liver MRI apart from Gd-EOB-DTPA, one of them being Gd-BOPTA (MultiHance®, Bracco Imaging, Milano, Italy). Gd-BOPTA shows less liver uptake compared to Gd-EOB-DTPA with only about 2-4% being eliminated through the biliary pathway, the rest being via renal excretion. Furthermore, it has substantially slower hepatic kinetics with a maximum enhancement in the liver parenchyma after 40-120 minutes compared to about 20 minutes for Gd-EOB-DTPA, making it less suitable for tracer kinetics estimation[157]. Mangafodipir

trisodium, Mn-DPDP (Teslascan®, GE Healthcare, Milwaukee, USA) is a manganese (Mn) chelate developed for hepatobiliary imaging. The hepatocellular uptake is probably through the vitamin B6 system, and approximately 60% of the administered dose is excreted through the hepatobiliary pathway. The maximum signal intensity from the start of injection occurs after about 20 minutes[218]. Mn-DPDP is usually administered as a slow intravenous infusion over about 20 minutes, making it unsuitable for dynamic imaging. At present, Teslascan® is not commercially available in Sweden.

There are also MRI contrast agents designed for the RES of the liver, such as Endorem® (Guerbet, France) and Resovist® (Bayer Schering Pharma, Berlin, Germany). They consist of small iron particles that are phagocytised by Kupffer-cells and since they are not extracted by hepatocytes, they cannot be used to assess hepatocellular function.

5.3 CLINICAL SIGNIFICANCE

Although the literature describes a multitude of methods for dynamic assessment of liver function, invasive as well as non-invasive, no single test stands out as a generally accepted golden standard. This is probably due to the fact that all tests described have their particular shortcomings, and no method has proven to be of undisputable benefit compared to others. Furthermore, the results of studies on liver function tests are often not using unanimously approved units of measurement and are not reported in a standardized fashion, and different definitions of outcome such as liver failure are frequent. This lack of agreement makes comparison between different studies difficult or impossible. The absence of a golden standard makes it hard to evaluate the possible benefits of a new method to assess liver function, since there is no generally agreed reference method to be used for comparison.

In current practice MRI plays an important role in the management of PSC patients. For example, the diagnosis is frequently based on MRC findings and imaging-based screening of the PSC population is advised for the early detection of gallbladder carcinoma[46]. DHCE-MRI can be performed as an add-on to already existing MRI protocols with a moderate increase in total imaging time. According to current diagnostic criteria liver biopsy is not mandatory for the diagnosis of PSC or PBC. Nevertheless, it is frequently used for confirming the diagnosis and to rule out overlap between these diseases and AIH. The non-homogeneous nature of chronic cholestatic disease results in a significant risk of sampling error for grading of cirrhosis and fibrosis[46, 219]. Segmental functional data that identify the most affected parts of the liver could direct biopsies, thereby making histology more representative of disease activity and grade. Segmental DA-derived functional parameters were shown to correlate with the quantitative bile duct scores in PSC patients. That could open up the possibility of assessing the impact of radiologically detected biliary strictures on actual liver function, allowing more judicious selection of strictures for intervention. Furthermore, the result of endoscopic or percutaneous intervention aimed at strictures could be quantified, and the effect of novel medical treatments on parenchymal function and bile flow could be assessed.

Liver surgery has seen an unparalleled expansion and evolution during the last decades. Despite the tremendous advances in operative technique and perioperative care, postoperative liver failure continues to be a major cause of postoperative morbidity and mortality. In current clinical practice there is no consensus regarding the necessity of preoperative liver functional analysis, nor is there a unanimously preferred method. Decision-making is not infrequently based on a subjective judgment of what is regarded as a sufficient RLV, often incorrectly seen as being directly proportional to RLF. What the critical RLV is has not been scientifically evaluated, but in a recent survey of hepato-pancreato-biliary and transplant centres large variations in what was regarded as critical RLV after liver resection were found [103]. For normal livers the critical RLV was 25% (range 15-40%) and for patients with cirrhosis 50% (range 25-90%). The large range in what respondents regard as the critical RLV in patients with cirrhosis is striking and probably indicative of a wide spectrum in disease severity in the cirrhosis population, but also uncertainty regarding the state of the parenchyma, reflecting lack of confidence in the existing clinical and metabolic methods to evaluate liver function. The survey also showed large differences in the use of pre-operative quantitative metabolic tests to assess liver function. In the United States clinical assessment was favoured, often using scoring systems such as the CPS and Okuda classification [220]. In the same study only 11% of North American centres used pre-operative metabolic assessment, compared to 76% of Asian and 43% of European centres.

Historically, underlying parenchymal liver disease in patients considered for liver resection was almost exclusively limited to cirrhosis in patients with resectable HCC. In current practice parenchymal dysfunction is encountered with increasing frequency in non-cirrhotic patients. Colorectal cancer liver metastases have, at least in Western countries, become the most common indication for liver resection. Chemotherapy is used with increasing frequency for down-staging or in the neo-adjuvant setting. Although not all agents have been studied, some have shown to be hepatotoxic, resulting in sinusoidal obstruction syndrome (SOS) and chemotherapy-associated steatohepatitis (CASH), associated with a higher morbidity and even higher mortality after surgery [7, 221, 222]. Probably due to what is known as the obesity epidemic, NAFLD has become the most common chronic liver disease in the Western world. Between 10% and 20% of the patients with NAFLD will progress to NASH, which may in turn lead to liver cirrhosis and HCC[223, 224]. Both chemotherapy-induced liver injury and metabolic syndrome-associated hepatic disease have been shown to be non-homogeneously distributed within the liver [34, 201-203].

Certainly, not all the patients included in this work would be candidates for liver resection, should an indication arise. The hepatectomy simulation does however demonstrate the potential danger of trusting the results of a global liver function test in patients with non-homogeneous parenchymal liver disease. Even if global tests are likely to become more sophisticated, maybe even giving information on multiple metabolic pathways, the results in this study argue strongly in favour of incorporating data on segmental liver function in the preoperative assessment of postoperative RLF. Patients considered for liver resection should not be subjected to unnecessary risks by overestimating RLF. Nor should patients that are in fact eligible for surgery be

excluded from potential curative treatment due to underestimation of their postoperative remnant functional capacity.

With DHCE-MRI, one might have the long sought after "one stop shop" for liver function assessment close at hand. MRI can provide detailed anatomical information on the biliary and vascular anatomy of the liver, oncological information including characterization of liver lesions, their number, size, and location as well as functional information regarding these lesions. From MR images, total and segmental liver volumes can be obtained for accurate volumetry. Furthermore, MRI can give information about fat and iron content of the liver parenchyma and theoretically, a MRI scan can be repeated an infinite number of times without known risk to the patient. With the addition of DHCE-MRI to the above applications, total and regional liver function can be added to the list of what is possible to achieve with MRI.

To gain wide acceptance, a liver function test should not only be safe, accurate and reproducible, but also it needs to carry a reasonable cost and be readily available. Most importantly, a test must provide added information which will impact clinical decision-making. DHCE-MRI fulfils at least some of these criteria. It is safe and non-invasive and MRI scanners are often available at larger hepatology institutions and in centres where liver surgery is performed. This work was done on a standard 1.5T scanner with a standard clinical pulse sequence. Gd-EOB-DTPA is commercially available as Primovist® in large parts of the world, including most countries in Europe, Asia and USA. There are data showing that Gd-EOB-DTPA-enhanced MRI is superior to contrast-enhanced CT in detecting small colorectal cancer metastases, and also superior regarding characterization of small HCC nodules, and that the use of MRI in this context is probably cost-efficient[225]. How accurate and reproducible DHCE-MRI is in preoperative liver function assessment and other clinical settings, and what the added value might be, has to be clarified in future studies.

5.4 FUTURE STUDIES

The aim of future studies in the area of DHCE-MRI for liver function assessment can be foreseen to have two major directions. The first will deal with the method itself, and there are numerous unanswered questions that have to be further addressed. These include issues like:

- Is the temporal resolution in the acquisition of the input function sufficient for a correct estimation of the DA-derived functional parameters?
- Is the method for correlation between signal intensity and contrast agent concentration sufficient, or can it be improved?
- What would the impact be on the stability and reproducibility of the studied parameters if image registration for motion correction was employed?
- Can pharmacokinetic compartmental modelling be used to assess the hepatic kinetics of Gd-EOB-DTPA, and how do they relate to the parameters that have already been studied?
- Could the performance of TSVD be improved with an algorithm to automatically determine the optimal truncation threshold c?

- How much can the protocol be shortened and how few acquisitions can we make and still have acceptable stability in DHCE-MRI derived parameters?
- Can the spatial or temporal resolution (or both) be improved by using more sophisticated pulse sequences?
- How will the use of a 3T MRI scanner influence the possibilities to improve data acquisition in DHCE-MRI?
- How does total extraction capacity of Gd-EOB-DTPA expressed as HEFml correlate to more established ways of quantitative liver function analysis, such as ICG clearance or the LiMax test?
- Can DHCE-MRI be used to assess segmental and total bile flow?

The other main direction regarding future studies will have to deal with the clinical usefulness of the method. Several such studies could be performed, for example:

- Can results from DHCE-MRI improve the diagnostic yield of liver biopsies if they are directed to segments that seem more affected by disease?
- Can DHCE-MRI be used to complement and improve the accuracy of currently used scoring models in PSC and PBC?
- Can DHCE-MRI be used to predict which patients with chronic liver disease will progress rapidly and develop liver failure, thereby aiding in selection of the optimal time-point for liver transplantation?
- Is there a cut-off value for the predicted post-operative HEFml that will predict post-operative liver failure, morbidity or mortality?
- Can the prospective use of DHCE-MRI decrease postoperative morbidity and mortality in liver resections?
- Can DHCE-MRI be used to monitor the progression of liver damage when neo-adjuvant chemotherapy is used in the multimodality treatment of colorectal cancer liver metastasis?
- Can DHCE-MRI be used to assess not only the volume increase, but also the increase in liver function when portal vein embolisation/ligation is performed?

6 CONCLUSIONS

To conclude, this work presents a method for liver function and volume assessment, DHCE-MRI, using MRI for sampling and Gd-EOB-DTPA as tracer. The studies in this work have shown that:

- The quantitative parameters HEF, irBF and MTT derived from DA can be determined on a global and segmental level in the liver, either using a voxel-based or ROI-based method.

- TSVD for DA performs marginally better in a computer simulation than FA, but in vivo TSVD seems to be substantially inferior to FA in the setting of DA and DHCE-MRI.

- Traditional semi-quantitative parameters, such as C_{max}, t_{max} and $t_{1/2}$ fail in separating controls from patients with mild PBC.

- Global HEF and MTT significantly differ between patients with PBC and healthy controls.

- The segmental results of the quantitative parameters HEF and irBF correlate with downstream biliary obstruction for the corresponding segment in patients with PSC.

- Using a voxel-based analysis in DHCE-MRI, total and segmental liver extraction capacity of Gd-EOB-DTPA expressed in HEFml can be determined, as well as total and segmental liver volumes.

- Total hepatic extraction capacity in HEFml, global median HEF and global median MTT differ significantly between healthy controls and patients with liver cirrhosis induced by alcohol and/or HCV.

- DHCE-MRI derived quantitative liver function parameters and the LSER show good to excellent capacity in separating groups with preserved liver function from a group with impaired liver function.

- DHCE-MRI derived quantitative liver function parameters and the LSER correlate with established scoring models for chronic liver disease and liver cirrhosis.

- In liver cirrhosis and in patients with mild to moderate PSC, liver function is significantly more heterogeneously distributed than in healthy controls.

- This heterogeneous distribution of liver function could have significant impact on the accuracy regarding prediction of postoperative RLF in patients with parenchymal disease.

7 SUMMARY IN SWEDISH

Avhandlingen består av fyra delarbeten, och beskriver en metod där magnetkameraundersökning (MR) används för att mäta upptaget av ett kontrastmedel i levern. Levern är funktionellt indelad i åtta leversegment med separat blodtillförsel och separat gallavflöde. Vid sjukdomar som ger levercirros vet man att sjukdomsgraden kan variera mellan olika delar av levern, och det finns idag ingen etablerad metod för att bedöma funktionen i de olika segmenten separat.

Sedan några år tillbaka finns ett kontrastmedel för MR, Primovist® (Gd-EOB-DTPA) som tas upp av fungerande leverceller, och utsöndras i gallan. Dessa egenskaper hos kontrastmedlet har väckt tanken att det skulle kunna användas för bedömning av leverfunktionen. Tanken är att om upptaget av Primovist i leverceller kan kvantifieras så skulle detta upptag avspegla leverfunktion i det område av levern där upptaget studerats. I djurförsök med experimentellt inducerad leverskada har man funnit en med MR detekterbar skillnad i upptag av Primovist mellan sjuk och frisk levervävnad. Ett antal studier har gjorts på människa där det också kunde konstateras att upptaget av Primovist hos leversjuka är lägre än hos friska och att skillnaden ökar med ökande sjukdomsgrad.

I det första delarbetet inkluderades 20 friska försökspersoner som undersöktes med MR efter att ha erhållit en dos kontrastmedel intravenöst. Kontrasmedelsupptaget i varje leversegment kvantifierades genom att signalintensiteten i blodbanan och levern registrerades under en sammanlagd tid av 90 minuter. De kurvor över signalintensiteten över tid (SI/tid)som erhölls analyserades genom en matematisk modell (dekonvoluering). Två olika matematiska metoder användes för dekonvolueringen och utfallet av dessa två metoder jämfördes. De parametrar som studerades var hepatocytextraktionsfraktionen (HEF) och en pefusionsparmeter (irBF) som beskriver lokalt blodflöde i levern. Dessutom genomfördes en datorsimulering där motsvarande SI/tid-kurvor försågs med olika mängd störande brus och de två matematiska modellernas resultat vid olika signal/brusförhållanden analyserades. Det första delarbetets resultat visade att kvantifiering av kontrastmedelsupptag och blodflöde gick att göra på segmentnivå i levern, att bägge matematiska metoder gav likvärdiga resultat avseende medianvärde på HEF och irBF, men den ena gav lägre standardavvikelse i resultaten och bedömdes som en stabilare metod.

I det andra delarbetet undersöktes tolv patienter med primär biliär cirros (PBC) med samma MR-metod som de friska försökspersonerna i första delarbetet. Målsättningen med studien var att undersöka huruvida upptaget av kontrastmedlet Gd-EOB-DTPA skiljde sig åt mellan patienter med leversjukdom och friska försökspersoner, och om denna skillnad gick att kvantifiera med den i det första delarbetet använda metoden. Som kontrollgrupp användes de friska försökspersonerna från första delarbetet. Upptaget kvantifierades dels genom samma matematiska modeller som i det första arbetet, dels genom traditionella farmakokinetiska parametrar (C_{max}, t_{max}, $t_{1/2}$). Resultaten visade att HEF var signifikant lägre och den genomsnittliga passagetiden för konttrasmtedlet (MTT) var signifikant kortare hos de leversjuka, och att skillnaden

ökade med ökande sjukdomsgrad. Studien visade också att de traditionella farmakokinetiska parametrarna inte kunda användas för att skilja grupperna åt.

I det tredje delarbetet inkluderades 12 patienter med primär skleroserande kolangit (PSC) som undersöktes på samma sätt som försökspersonerna och patienterna i delarbete ett och två. Sjukdomen PSC drabbar gallgångarna och leder till gallgångsskrumpning (gallgångsstriktur), och vid avancerad sjukdom även skrumplever (cirros). Kontrollgruppen var även här försökspersonerna från den första studien. Målsättningen var att mäta segmentell och total levervolym med utgångspunkt i bildmaterialet. Genom att använda metoden från de två första delarbetena med skillnanden att beräkningarna genomfördes i varje voxel (bildmaterialets minsta beståndsdelar) separat kunde varje segments och hela leverns extraktionsförmåga beräknas. Även information om funktionella aspekter av levervävnaden i övrigt, såsom HEF, irBF och MTT, kunde beräknas. Studien visade att resultaten av den totala leverfunktionsbedömningen korrelerade med sjukdomsgrad hos patienterna och att den segmentella funktionen korrelerade med graden av gallgångsskrumpning. Studien visade även att leverfunktionen var betydligt mer ojämnt fördelad inom levern hos patienter med PSC jämfört med friska försökspersoner.

Det fjärde delarbetet syftade till att undersöka om de skillnader i total leverfunktion som borde finnas mellan friska och leversjuka går att detektera och kvantifiera med den i delarbete tre använda metoden. Syftet var också att undersöka om leverfunktionen även hos patienter med cirros är oregelbundet fördelat i levern, och vad detta skulle kunna innebära vid en leveroperation. I denna studie undersöktes 10 patienter med olika grad av levercirros. Även i detta arbete undersöktes total och segmentell leverfunktion och samma kontrollgrupp som i tidigare arbeten fick tjäna som referens. Resultaten visade att leverfunktionen även hos cirrospatienter är mer ojämnt fördelad i levern än hos friska, och att den förväntade skillnaden i leverfunktion gick att detektera och kvantifiera. Den totala leverfunktionen mätt som den totala extraktionskapaciteten av Gd-EOB-DTPA för hela levern korrelerade väl med etablerade scoringsystem för leversjukdom. Studien visade också att den ojämna fördelningen av funktion i levern som kan ses vid leversjukdomar kan ha en avgörande betydelse vid leveroperationer, då den förväntade kvarvarande funktionen inte kan beräknas på ett tillförlitligt sätt om inte regionala skillnader i leverfunktion tas med i kalkylen.

En metod för bedömning av segmentell leverfunktion skulle kunna komplettera de nuvarande överlevnadsmodellerna för PSC och PBC, och leverbiopsier skulle kunna riktas mot de mest angripna delarna av levern och därigenom ge bättre information om sjukdomsgrad. En funktionell bedömning av gallgångsstrikturer hos patienter med PSC skulle kunna visa vilka strikturer som är mest lämpade för endoskopisk behandling och dessutom utvärdera resultatet av sådan behandling. Även effekten av medicinsk behandling och nya medicinska metoder skulle kunna bedömas på ett objektivt sätt. I en förlängning skulle en fungerande metod för bedömning av segmentell leverfunktion erbjuda en ny möjlighet att följa leverfunktionen över tid under till exempel cytostatikabehandling inför kirurgi, underlätta planeringen av leverresektioner och göra dessa säkrare, samt följa leverfunktionen hos levertransplanterade.

8 ACKNOWLEDGEMENTS

I wish to express my deepest gratitude to all who have been involved in this project, one way or another. You have helped me realize this work, and without you this would not have happened. In particular, my thoughts go to:

My main supervisor Eduard Jonas for his never-ending optimism, his enormous energy and rock-hard belief in this project. You are the epitome of perseverance and working with you is never dull. Whatever the subject, your experience provides new dimensions!

My co-supervisor Lennart Blomqvist for guiding me through the mysteries of MRI, and for providing such a fantastic support, for funding, for encouraging me and for your never-ending belief in me and in this project.

My co-supervisor Erik Näslund for your support, both financially and intellectually, and for guiding me through the administrative hassles of research. You are the Master!

The present head of Department of Surgery and Urology, Danderyd Hospital, Johanna Albert and her predecessor Staffan Gröndal, for providing me the opportunity to do this research project alongside my clinical work as a surgeon, and for the job that pays my bills.

MRI physicists and co-authors Lena Douglas and Anders Nordell for your invaluable support regarding the MRI pulse sequences, mathematical calculations and last but not least, for the development of the ELEFANT software for image analysis. Anders, you gave birth to the ELEFANT, and Lena, you made the ELEFANT fly!

MRI technicians Roberto Vargas, Tord Jigbrant and Yvonne Eriksson-Alm for helping me acquire all the MRI scans and for good times while doing it!

Co-authors Annika Bergquist, Karin Hagen, Hans Jacobsson and Izabella Janczewska for helping me recruit patients, and for your expertise and intellectual input into this project.

Piet Jonas for great hospitality during my visit to South Africa, but most of all for your invaluable help with making the English language of the papers and thesis less flawed.

All colleagues at the upper GI-surgery unit for their patience with me and my frequent absence for research. You have filled in for me so many times, and now it is pay-back time!

Lars Granström, head of the upper GI-surgery unit, for taking me into the team and providing me such an inspiring and challenging work environment. There could be no better!

My present and former room-mates Jacob Freedman and Martin Sundelöf for encouraging me when things did not go as well as one had hoped, and for numerous talks about work, life, wine and food.

All colleagues at the Department of Surgery and Urology, Danderyd Hospital for making the department a good place to be!

My former colleagues at the Department of Surgery, Bollnäs Hospital for guiding me on my first steps into the field of surgery, in particular Jörgen Block for being such a tremendous role model and teacher.

All patients and volunteers who willingly entered the quite confined space of the MRI scanner for such an extended time, just for the good of science. There would definitely not have been a thesis without you!

All my friends from long ago that still stick with me, even though I don't keep in touch as I should (you know who you are). You all mean the world to me, and you also contributed to this thesis!

My mother Inger and my father Nils-Göran for having such an enormous belief in me and for your never-ending love and support no matter what.

Last but definitely not least, Ingeli, Eric and Sarah for putting up with me being so absent so often, both mentally and physically. Thank you for your support and love!

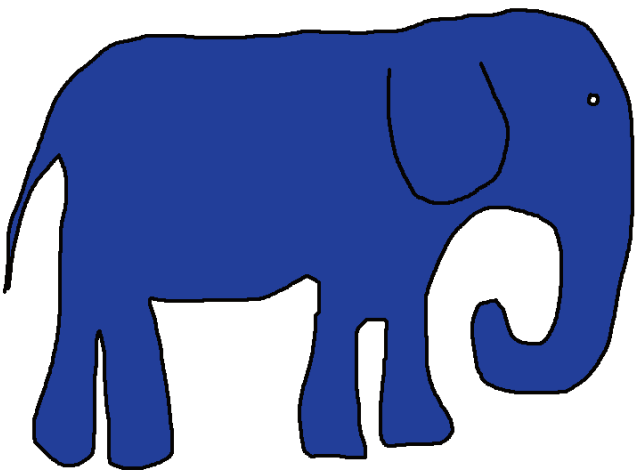

9 REFERENCES

1. Glisson F. Anatomia Hepatis. London: Dugard; 1654.

2. Foster JH. History of liver surgery. *Arch Surg.* Mar 1991;126(3):381-387.

3. National Board of Health and Welfare S. Statistics. 2011; http://www.socialstyrelsen.se/statistics. Accessed 2011-03-27, 2011.

4. van den Broek MA, van Dam RM, Malago M, Dejong CH, van Breukelen GJ, Olde Damink SW. Feasibility of randomized controlled trials in liver surgery using surgery-related mortality or morbidity as endpoint. *Br J Surg.* Sep 2009;96(9):1005-1014.

5. Capussotti L, Vigano L, Giuliante F, Ferrero A, Giovannini I, Nuzzo G. Liver dysfunction and sepsis determine operative mortality after liver resection. *Br J Surg.* Jan 2009;96(1):88-94.

6. Balzan S, Belghiti J, Farges O, et al. The "50-50 criteria" on postoperative day 5: an accurate predictor of liver failure and death after hepatectomy. *Ann Surg.* Dec 2005;242(6):824-828, discussion 828-829.

7. Mullen JT, Ribero D, Reddy SK, et al. Hepatic insufficiency and mortality in 1,059 noncirrhotic patients undergoing major hepatectomy. *J Am Coll Surg.* May 2007;204(5):854-862; discussion 862-854.

8. Cantlie J. On a new arrangement of the right and left lobes of the liver. *Proc. Anat. Soc. Great Britain Ireland.* 1897(32):4-9.

9. Rex H. Beitrage zur Morphologie der Saugerleber. *Morphol. Jahrb.* 1888(14):517-615.

10. Hjortsjö CH. The topography of the intrahepatic duct systems. *Acta Anat (Basel).* 1951;11(4):599-615.

11. Healey JE, Jr., Schroy PC. Anatomy of the biliary ducts within the human liver; analysis of the prevailing pattern of branchings and the major variations of the biliary ducts. *AMA Arch Surg.* May 1953;66(5):599-616.

12. Healey JE, Jr., Schroy PC, Sorensen RJ. The intrahepatic distribution of the hepatic artery in man. *J Int Coll Surg.* Aug 1953;20(2):133-148.

13. Couinaud C. *Le foie; études anatomiques et chirurgicales*. Paris,: Masson; 1957.

14. Strasberg SM. Terminology of liver anatomy and liver resections: coming to grips with hepatic Babel. *J Am Coll Surg.* Apr 1997;184(4):413-434.

15. Strasberg SM. Nomenclature of hepatic anatomy and resections: a review of the Brisbane 2000 system. *J Hepatobiliary Pancreat Surg.* 2005;12(5):351-355.

16. Dodds WJ, Erickson SJ, Taylor AJ, Lawson TL, Stewart ET. Caudate lobe of the liver: anatomy, embryology, and pathology. *AJR Am J Roentgenol.* Jan 1990;154(1):87-93.

17. Skandalakis JE, Skandalakis LJ, Skandalakis PN, Mirilas P. Hepatic surgical anatomy. *Surg Clin North Am.* Apr 2004;84(2):413-435, viii.

18. Chiandussi L, Greco F, Sardi G, Vaccarino A, Ferraris CM, Curti B. Estimation of hepatic arterial and portal venous blood flow by direct catheterization of the vena porta through the umbilical cord in man. Preliminary results. *Acta Hepatosplenol.* May-Jun 1968;15(3):166-171.

19. Schenk WG, Jr., Mc DJ, Mc DK, Drapanas T. Direct measurement of hepatic blood flow in surgical patients: with related observations on hepatic flow dynamics in experimental animals. *Ann Surg.* Sep 1962;156:463-471.

20. Song SY, Chung JW, Yin YH, et al. Celiac axis and common hepatic artery variations in 5002 patients: systematic analysis with spiral CT and DSA. *Radiology.* Apr 2010;255(1):278-288.
21. Hiatt JR, Gabbay J, Busuttil RW. Surgical anatomy of the hepatic arteries in 1000 cases. *Ann Surg.* Jul 1994;220(1):50-52.
22. Abdel-Misih SR, Bloomston M. Liver anatomy. *Surg Clin North Am.* Aug 2010;90(4):643-653.
23. Kawarada Y, Das BC, Taoka H. Anatomy of the hepatic hilar area: the plate system. *J Hepatobiliary Pancreat Surg.* 2000;7(6):580-586.
24. Bernard C. Leçon de physiologie expérimentale. Paris: Baillieres; 1855.
25. Sherlock S, Dooley J. *Diseases of the liver and biliary system*. 11th ed: Blackwell Science; 2002.
26. Deltenre P, Valla DC. Ischemic cholangiopathy. *Semin Liver Dis.* Aug 2008;28(3):235-246.
27. Rappaport AM. The microcirculatory acinar concept of normal and pathological hepatic structure. *Beitr Pathol.* May 1976;157(3):215-243.
28. Jungermann K, Kietzmann T. Oxygen: modulator of metabolic zonation and disease of the liver. *Hepatology.* Feb 2000;31(2):255-260.
29. Argo CK, Caldwell SH. Epidemiology and natural history of non-alcoholic steatohepatitis. *Clin Liver Dis.* Nov 2009;13(4):511-531.
30. Bataller R, Brenner DA. Liver fibrosis. *J Clin Invest.* Feb 2005;115(2):209-218.
31. Batts KP, Ludwig J. Chronic hepatitis. An update on terminology and reporting. *Am J Surg Pathol.* Dec 1995;19(12):1409-1417.
32. Bedossa P, Poynard T. An algorithm for the grading of activity in chronic hepatitis C. The METAVIR Cooperative Study Group. *Hepatology.* Aug 1996;24(2):289-293.
33. Regev A, Berho M, Jeffers LJ, et al. Sampling error and intraobserver variation in liver biopsy in patients with chronic HCV infection. *Am J Gastroenterol.* Oct 2002;97(10):2614-2618.
34. Ratziu V, Charlotte F, Heurtier A, et al. Sampling variability of liver biopsy in nonalcoholic fatty liver disease. *Gastroenterology.* Jun 2005;128(7):1898-1906.
35. Maharaj B, Maharaj RJ, Leary WP, et al. Sampling variability and its influence on the diagnostic yield of percutaneous needle biopsy of the liver. *Lancet.* Mar 8 1986;1(8480):523-525.
36. Shreiner DP, Barlai-Kovach M. Diagnosis of alcoholic cirrhosis with the right-to-left hepatic lobe ratio: concise communication. *J Nucl Med.* Feb 1981;22(2):116-120.
37. Harbin WP, Robert NJ, Ferrucci JT, Jr. Diagnosis of cirrhosis based on regional changes in hepatic morphology: a radiological and pathological analysis. *Radiology.* May 1980;135(2):273-283.
38. Blomquist L, Wang Y, Kimiaei S, Jacobsson H. Change in size, shape and radiocolloid uptake of the alcoholic liver during alcohol withdrawal, as demonstrated by single photon emission computed tomography. *J Hepatol.* Sep 1994;21(3):417-423.
39. Torres WE, Whitmire LF, Gedgaudas-McClees K, Bernardino ME. Computed tomography of hepatic morphologic changes in cirrhosis of the liver. *J Comput Assist Tomogr.* Jan-Feb 1986;10(1):47-50.
40. Crosignani A, Battezzati PM, Invernizzi P, Selmi C, Prina E, Podda M. Clinical features and management of primary biliary cirrhosis. *World J Gastroenterol.* Jun 7 2008;14(21):3313-3327.
41. Invernizzi P, Gershwin ME. The genetic basis of primary biliary cirrhosis: premises, not promises. *Gastroenterology.* Oct 2008;135(4):1044-1047.

42. Invernizzi P, Miozzo M, Battezzati PM, et al. Frequency of monosomy X in women with primary biliary cirrhosis. *Lancet.* Feb 14 2004;363(9408):533-535.
43. Nguyen DL, Juran BD, Lazaridis KN. Primary biliary cirrhosis. *Best Pract Res Clin Gastroenterol.* Oct 2010;24(5):647-654.
44. Zein CO, Lindor KD. Latest and emerging therapies for primary biliary cirrhosis and primary sclerosing cholangitis. *Curr Gastroenterol Rep.* Feb 2010;12(1):13-22.
45. Prince MI, Chetwynd A, Craig WL, Metcalf JV, James OF. Asymptomatic primary biliary cirrhosis: clinical features, prognosis, and symptom progression in a large population based cohort. *Gut.* Jun 2004;53(6):865-870.
46. EASL Clinical Practice Guidelines: management of cholestatic liver diseases. *J Hepatol.* Aug 2009;51(2):237-267.
47. Hohenester S, Oude-Elferink RP, Beuers U. Primary biliary cirrhosis. *Semin Immunopathol.* Sep 2009;31(3):283-307.
48. Scheuer PJ. Primary biliary cirrhosis: diagnosis, pathology and pathogenesis. *Postgrad Med J.* 1983;59 Suppl 4:106-115.
49. Christensen E, Neuberger J, Crowe J, et al. Beneficial effect of azathioprine and prediction of prognosis in primary biliary cirrhosis. Final results of an international trial. *Gastroenterology.* Nov 1985;89(5):1084-1091.
50. Dickson ER, Grambsch PM, Fleming TR, Fisher LD, Langworthy A. Prognosis in primary biliary cirrhosis: model for decision making. *Hepatology.* Jul 1989;10(1):1-7.
51. Goudie BM, Burt AD, Macfarlane GJ, et al. Risk factors and prognosis in primary biliary cirrhosis. *Am J Gastroenterol.* Jul 1989;84(7):713-716.
52. Roll J, Boyer JL, Barry D, Klatskin G. The prognostic importance of clinical and histologic features in asymptomatic and symptomatic primary biliary cirrhosis. *N Engl J Med.* Jan 6 1983;308(1):1-7.
53. Rydning A, Schrumpf E, Abdelnoor M, Elgjo K, Jenssen E. Factors of prognostic importance in primary biliary cirrhosis. *Scand J Gastroenterol.* Feb 1990;25(2):119-126.
54. Murtaugh PA, Dickson ER, Van Dam GM, et al. Primary biliary cirrhosis: prediction of short-term survival based on repeated patient visits. *Hepatology.* Jul 1994;20(1 Pt 1):126-134.
55. Kaplan MM, Gershwin ME. Primary biliary cirrhosis. *N Engl J Med.* Sep 22 2005;353(12):1261-1273.
56. Bruix J, Sherman M. Management of hepatocellular carcinoma. *Hepatology.* Nov 2005;42(5):1208-1236.
57. Karlsen TH, Schrumpf E, Boberg KM. Update on primary sclerosing cholangitis. *Dig Liver Dis.* Jun 2010;42(6):390-400.
58. Olsson R, Hägerstrand I, Broome U, et al. Sampling variability of percutaneous liver biopsy in primary sclerosing cholangitis. *J Clin Pathol.* 1995;48(10):933-935.
59. Wiesner RH. Liver transplantation for primary sclerosing cholangitis: timing, outcome, impact of inflammatory bowel disease and recurrence of disease. *Best Pract Res Clin Gastroenterol.* Aug 2001;15(4):667-680.
60. Karlsen TH, Schrumpf E, Boberg KM. Primary sclerosing cholangitis. *Best Pract Res Clin Gastroenterol.* Oct 2010;24(5):655-666.
61. Kim WR, Therneau TM, Wiesner RH, et al. A revised natural history model for primary sclerosing cholangitis. *Mayo Clin Proc.* Jul 2000;75(7):688-694.
62. Perz JF, Armstrong GL, Farrington LA, Hutin YJ, Bell BP. The contributions of hepatitis B virus and hepatitis C virus infections to cirrhosis and primary liver cancer worldwide. *J Hepatol.* Oct 2006;45(4):529-538.

63. Armstrong GL, Alter MJ, McQuillan GM, Margolis HS. The past incidence of hepatitis C virus infection: implications for the future burden of chronic liver disease in the United States. *Hepatology.* Mar 2000;31(3):777-782.
64. Ferenci P, Ferenci S, Datz C, Rezman I, Oberaigner W, Strauss R. Morbidity and mortality in paid Austrian plasma donors infected with hepatitis C at plasma donation in the 1970s. *J Hepatol.* Jul 2007;47(1):31-36.
65. Gunnarsdottir SA, Olsson R, Olafsson S, et al. Liver cirrhosis in Iceland and Sweden: incidence, aetiology and outcomes. *Scand J Gastroenterol.* 2009;44(8):984-993.
66. Poynard T, Ratziu V, Charlotte F, Goodman Z, McHutchison J, Albrecht J. Rates and risk factors of liver fibrosis progression in patients with chronic hepatitis c. *J Hepatol.* May 2001;34(5):730-739.
67. Piccinino F, Sagnelli E, Pasquale G, Giusti G. Complications following percutaneous liver biopsy. A multicentre retrospective study on 68,276 biopsies. *J Hepatol.* 1986;2(2):165-173.
68. Pratt DS, Kaplan MM. Evaluation of abnormal liver-enzyme results in asymptomatic patients. *N Engl J Med.* Apr 27 2000;342(17):1266-1271.
69. Astegiano M, Sapone N, Demarchi B, Rossetti S, Bonardi R, Rizzetto M. Laboratory evaluation of the patient with liver disease. *Eur Rev Med Pharmacol Sci.* Jan-Feb 2004;8(1):3-9.
70. Burke MD. Liver function: test selection and interpretation of results. *Clin Lab Med.* Jun 2002;22(2):377-390.
71. Child CG, Turcotte JG. Surgery and portal hypertension. *Major Probl Clin Surg.* 1964;1:1-85.
72. Pugh RN, Murray-Lyon IM, Dawson JL, Pietroni MC, Williams R. Transection of the oesophagus for bleeding oesophageal varices. *Br J Surg.* Aug 1973;60(8):646-649.
73. D'Amico G, Garcia-Tsao G, Pagliaro L. Natural history and prognostic indicators of survival in cirrhosis: a systematic review of 118 studies. *J Hepatol.* Jan 2006;44(1):217-231.
74. Schroeder RA, Marroquin CE, Bute BP, Khuri S, Henderson WG, Kuo PC. Predictive indices of morbidity and mortality after liver resection. *Ann Surg.* Mar 2006;243(3):373-379.
75. Mansour A, Watson W, Shayani V, Pickleman J. Abdominal operations in patients with cirrhosis: still a major surgical challenge. *Surgery.* Oct 1997;122(4):730-735; discussion 735-736.
76. Kamath PS, Wiesner RH, Malinchoc M, et al. A model to predict survival in patients with end-stage liver disease. *Hepatology.* Feb 2001;33(2):464-470.
77. Malinchoc M, Kamath PS, Gordon FD, Peine CJ, Rank J, ter Borg PC. A model to predict poor survival in patients undergoing transjugular intrahepatic portosystemic shunts. *Hepatology.* Apr 2000;31(4):864-871.
78. Kamath PS, Kim WR. The model for end-stage liver disease (MELD). *Hepatology.* Mar 2007;45(3):797-805.
79. Wiesner R, Edwards E, Freeman R, et al. Model for end-stage liver disease (MELD) and allocation of donor livers. *Gastroenterology.* Jan 2003;124(1):91-96.
80. Saab S, Wang V, Ibrahim AB, et al. MELD score predicts 1-year patient survival post-orthotopic liver transplantation. *Liver Transpl.* May 2003;9(5):473-476.
81. Teh SH, Christein J, Donohue J, et al. Hepatic resection of hepatocellular carcinoma in patients with cirrhosis: Model of End-Stage Liver Disease

(MELD) score predicts perioperative mortality. *J Gastrointest Surg.* Dec 2005;9(9):1207-1215; discussion 1215.

82. Cucchetti A, Ercolani G, Vivarelli M, et al. Impact of model for end-stage liver disease (MELD) score on prognosis after hepatectomy for hepatocellular carcinoma on cirrhosis. *Liver Transpl.* Jun 2006;12(6):966-971.

83. Teh SH, Sheppard BC, Schwartz J, Orloff SL. Model for End-stage Liver Disease score fails to predict perioperative outcome after hepatic resection for hepatocellular carcinoma in patients without cirrhosis. *Am J Surg.* May 2008;195(5):697-701.

84. Brockmöller J, Roots I. Assessment of liver metabolic function. Clinical implications. *Clin Pharmacokinet.* 1994;27(3):216-248.

85. Morris-Stiff G, Gomez D, Prasad R. Quantitative assessment of hepatic function and its relevance to the liver surgeon. *J Gastrointest Surg.* Feb 2009;13(2):374-385.

86. Schneider PD. Preoperative assessment of liver function. *Surg Clin North Am.* Apr 2004;84(2):355-373.

87. Imaoka S, Enomoto K, Oda Y, et al. Lidocaine metabolism by human cytochrome P-450s purified from hepatic microsomes: comparison of those with rat hepatic cytochrome P-450s. *J Pharmacol Exp Ther.* Dec 1990;255(3):1385-1391.

88. Ercolani G, Grazi GL, Calliva R, et al. The lidocaine (MEGX) test as an index of hepatic function: its clinical usefulness in liver surgery. *Surgery.* Apr 2000;127(4):464-471.

89. Goresky CA, Bach GG, Nadeau BE. On the uptake of materials by the intact liver. The transport and net removal of galactose. *J Clin Invest.* May 1973;52(5):991-1009.

90. Zoedler T, Ebener C, Becker H, Roeher HD. Evaluation of liver function tests to predict operative risk in liver surgery. *HPB Surg.* 1995;9(1):13-18.

91. Redaelli CA, Dufour JF, Wagner M, et al. Preoperative galactose elimination capacity predicts complications and survival after hepatic resection. *Ann Surg.* Jan 2002;235(1):77-85.

92. Galizzi J, Long RG, Billing BH, Sherlock S. Assessment of the (14C) aminopyrine breath test in liver disease. *Gut.* Jan 1978;19(1):40-45.

93. Merkel C, Gatta A, Zoli M, et al. Prognostic value of galactose elimination capacity, aminopyrine breath test, and ICG clearance in patients with cirrhosis. Comparison with the Pugh score. *Dig Dis Sci.* Sep 1991;36(9):1197-1203.

94. de Graaf W, Hausler S, Heger M, et al. Transporters involved in the hepatic uptake of (99m)Tc-mebrofenin and indocyanine green. *J Hepatol.* Oct 1 2010.

95. Faybik P, Hetz H. Plasma disappearance rate of indocyanine green in liver dysfunction. *Transplant Proc.* Apr 2006;38(3):801-802.

96. Reekers M, Simon MJ, Boer F, et al. Pulse dye densitometry and indocyanine green plasma disappearance in ASA physical status I-II patients. *Anesth Analg.* Feb 1 2010;110(2):466-472.

97. Sheng QS, Lang R, He Q, Yang YJ, Zhao DF, Chen DZ. Indocyanine green clearance test and model for end-stage liver disease score of patients with liver cirrhosis. *Hepatobiliary Pancreat Dis Int.* Feb 2009;8(1):46-49.

98. Garcea G, Ong SL, Maddern GJ. Predicting liver failure following major hepatectomy. *Dig Liver Dis.* Nov 2009;41(11):798-806.

99. Fan ST, Lai EC, Lo CM, Ng IO, Wong J. Hospital mortality of major hepatectomy for hepatocellular carcinoma associated with cirrhosis. *Arch Surg.* Feb 1995;130(2):198-203.

100. Lau H, Man K, Fan ST, Yu WC, Lo CM, Wong J. Evaluation of preoperative hepatic function in patients with hepatocellular carcinoma undergoing hepatectomy. *Br J Surg.* 1997;84(9):1255-1259.
101. Makuuchi M, Kosuge T, Takayama T, et al. Surgery for small liver cancers. *Semin Surg Oncol.* Jul-Aug 1993;9(4):298-304.
102. Imamura H, Seyama Y, Kokudo N, et al. One thousand fifty-six hepatectomies without mortality in 8 years. *Arch Surg.* Nov 2003;138(11):1198-1206; discussion 1206.
103. Breitenstein S, Apestegui C, Petrowsky H, Clavien PA. "State of the art" in liver resection and living donor liver transplantation: a worldwide survey of 100 liver centers. *World J Surg.* Apr 2009;33(4):797-803.
104. Stockmann M, Lock JF, Riecke B, et al. Prediction of postoperative outcome after hepatectomy with a new bedside test for maximal liver function capacity. *Ann Surg.* Jul 2009;250(1):119-125.
105. Jiang Z, Dragin N, Jorge-Nebert LF, et al. Search for an association between the human CYP1A2 genotype and CYP1A2 metabolic phenotype. *Pharmacogenet Genomics.* May 2006;16(5):359-367.
106. Stockmann M, Lock JF, Malinowski M, Niehues SM, Seehofer D, Neuhaus P. The LiMAx test: a new liver function test for predicting postoperative outcome in liver surgery. *HPB (Oxford).* Mar 2010;12(2):139-146.
107. Marsman HA, van der Pool AE, Verheij J, et al. Hepatic steatosis assessment with CT or MRI in patients with colorectal liver metastases after neoadjuvant chemotherapy. *J Surg Oncol.* Mar 4 2011.
108. Sandrasegaran K, Kwo PW, DiGirolamo D, Stockberger SM, Jr., Cummings OW, Kopecky KK. Measurement of liver volume using spiral CT and the curved line and cubic spline algorithms: reproducibility and interobserver variation. *Abdom Imaging.* Jan-Feb 1999;24(1):61-65.
109. Vauthey JN, Chaoui A, Do KA, et al. Standardized measurement of the future liver remnant prior to extended liver resection: methodology and clinical associations. *Surgery.* May 2000;127(5):512-519.
110. Shoup M, Gonen M, D'Angelica M, et al. Volumetric analysis predicts hepatic dysfunction in patients undergoing major liver resection. *J Gastrointest Surg.* Mar-Apr 2003;7(3):325-330.
111. Ferrero A, Vigano L, Polastri R, et al. Postoperative liver dysfunction and future remnant liver: where is the limit? Results of a prospective study. *World J Surg.* Aug 2007;31(8):1643-1651.
112. Shirabe K, Shimada M, Gion T, et al. Postoperative liver failure after major hepatic resection for hepatocellular carcinoma in the modern era with special reference to remnant liver volume. *J Am Coll Surg.* Mar 1999;188(3):304-309.
113. Chun YS, Ribero D, Abdalla EK, et al. Comparison of two methods of future liver remnant volume measurement. *J Gastrointest Surg.* Jan 2008;12(1):123-128.
114. Vauthey JN, Abdalla EK, Doherty DA, et al. Body surface area and body weight predict total liver volume in Western adults. *Liver Transpl.* Mar 2002;8(3):233-240.
115. Krishnamurthy S, Krishnamurthy GT. Technetium-99m-iminodiacetic acid organic anions: review of biokinetics and clinical application in hepatology. *Hepatology.* Jan 1989;9(1):139-153.
116. Erdogan D, Heijnen BH, Bennink RJ, et al. Preoperative assessment of liver function: a comparison of 99mTc-Mebrofenin scintigraphy with indocyanine green clearance test. *Liver Int.* Apr 2004;24(2):117-123.

117. Brown PH, Juni JE, Lieberman DA, Krishnamurthy GT. Hepatocyte versus biliary disease: a distinction by deconvolutional analysis of technetium-99m IDA time-activity curves. *J Nucl Med.* May 1988;29(5):623-630.
118. de Graaf W, van Lienden KP, Dinant S, et al. Assessment of future remnant liver function using hepatobiliary scintigraphy in patients undergoing major liver resection. *J Gastrointest Surg.* Feb 2010;14(2):369-378.
119. de Graaf W, van Lienden KP, van Gulik TM, Bennink RJ. (99m)Tc-mebrofenin hepatobiliary scintigraphy with SPECT for the assessment of hepatic function and liver functional volume before partial hepatectomy. *J Nucl Med.* Feb 2010;51(2):229-236.
120. Dinant S, de Graaf W, Verwer BJ, et al. Risk assessment of posthepatectomy liver failure using hepatobiliary scintigraphy and CT volumetry. *J Nucl Med.* May 2007;48(5):685-692.
121. Doo E, Krishnamurthy GT, Eklem MJ, Gilbert S, Brown PH. Quantification of hepatobiliary function as an integral part of imaging with technetium-99m-mebrofenin in health and disease. *J Nucl Med.* Jan 1991;32(1):48-57.
122. Gambhir SS, Hawkins RA, Huang SC, Hall TR, Busuttil RW, Phelps ME. Tracer kinetic modeling approaches for the quantification of hepatic function with technetium-99m DISIDA and scintigraphy. *J Nucl Med.* Sep 1989;30(9):1507-1518.
123. Heyman S. Hepatobiliary scintigraphy as a liver function test. *J Nucl Med.* Mar 1994;35(3):436-437.
124. Jonas E, Näslund E, Freedman J, et al. Measurement of parenchymal function and bile duct flow in primary sclerosing cholangitis using dynamic 99mTc-HIDA SPECT. *J Gastroenterol Hepatol.* Apr 2006;21(4):674-681.
125. Kwon AH, Ha-Kawa SK, Uetsuji S, Kamiyama Y, Tanaka Y. Use of technetium 99m diethylenetriamine-pentaacetic acid-galactosyl-human serum albumin liver scintigraphy in the evaluation of preoperative and postoperative hepatic functional reserve for hepatectomy. *Surgery.* Apr 1995;117(4):429-434.
126. Sasaki N, Shiomi S, Iwata Y, et al. Clinical usefulness of scintigraphy with 99mTc-galactosyl-human serum albumin for prognosis of cirrhosis of the liver. *J Nucl Med.* Oct 1999;40(10):1652-1656.
127. de Graaf W, Bennink RJ, Veteläinen R, van Gulik TM. Nuclear imaging techniques for the assessment of hepatic function in liver surgery and transplantation. *J Nucl Med.* May 2010;51(5):742-752.
128. Kwon AH, Ha-Kawa SK, Uetsuji S, Inoue T, Matsui Y, Kamiyama Y. Preoperative determination of the surgical procedure for hepatectomy using technetium-99m-galactosyl human serum albumin (99mTc-GSA) liver scintigraphy. *Hepatology.* Feb 1997;25(2):426-429.
129. Hirai I, Kimura W, Fuse A, Suto K, Urayama M. Evaluation of preoperative portal embolization for safe hepatectomy, with special reference to assessment of nonembolized lobe function with 99mTc-GSA SPECT scintigraphy. *Surgery.* May 2003;133(5):495-506.
130. Nishiyama Y, Yamamoto Y, Hino I, Satoh K, Wakabayashi H, Ohkawa M. 99mTc galactosyl human serum albumin liver dynamic SPET for pre-operative assessment of hepatectomy in relation to percutaneous transhepatic portal embolization. *Nucl Med Commun.* Jul 2003;24(7):809-817.
131. Tanaka A, Shinohara H, Hatano E, et al. Perioperative changes in hepatic function as assessed by asialoglycoprotein receptor indices by technetium 99m galactosyl human serum albumin. *Hepatogastroenterology.* Jan-Feb 1999;46(25):369-375.

132. Jackson A, Buckley DL, Parker GJ, eds. *Dynamic Contrast-Enhanced Magnetic Resonance Imaging in Oncology*: Springer; 2003.
133. Tofts PS, Brix G, Buckley DL, et al. Estimating kinetic parameters from dynamic contrast-enhanced T(1)-weighted MRI of a diffusable tracer: standardized quantities and symbols. *J Magn Reson Imaging.* Sep 1999;10(3):223-232.
134. Padhani AR. Functional MRI for anticancer therapy assessment. *Eur J Cancer.* Nov 2002;38(16):2116-2127.
135. Planchamp C, Gex-Fabry M, Becker CD, Pastor CM. Model-based analysis of Gd-BOPTA-induced MR signal intensity changes in cirrhotic rat livers. *Invest Radiol.* Jul 2007;42(7):513-521.
136. Planchamp C, Gex-Fabry M, Dornier C, et al. Gd-BOPTA transport into rat hepatocytes: pharmacokinetic analysis of dynamic magnetic resonance images using a hollow-fiber bioreactor. *Invest Radiol.* Aug 2004;39(8):506-515.
137. Planchamp C, Pastor CM, Balant L, Becker CD, Terrier F, Gex-Fabry M. Quantification of Gd-BOPTA uptake and biliary excretion from dynamic magnetic resonance imaging in rat livers: model validation with 153Gd-BOPTA. *Invest Radiol.* Nov 2005;40(11):705-714.
138. Dujardin M, Sourbron S, Luypaert R, Verbeelen D, Stadnik T. Quantification of renal perfusion and function on a voxel-by-voxel basis: a feasibility study. *Magn Reson Med.* Oct 2005;54(4):841-849.
139. Michoux N, Vallee JP, Pechere-Bertschi A, Montet X, Buehler L, Van Beers BE. Analysis of contrast-enhanced MR images to assess renal function. *MAGMA.* Sep 2006;19(4):167-179.
140. Daniel GB, Bahr A, Dykes JA, DeNovo R, Young K, Smith GT. Hepatic extraction efficiency and excretion rate of technetium-99m-mebrofenin in dogs. *J Nucl Med.* Nov 1996;37(11):1846-1849.
141. Daniel GB, DeNovo R, Bahr A, Smith GT. Evaluation of heart time-activity curves as a predictor of hepatic extraction of 99mTc-mebrofenin in dogs. *Vet Radiol Ultrasound.* Mar-Apr 2001;42(2):162-168.
142. Daniel GB, DeNovo R, Schultze AE, Schmidt D, Smith GT. Validation of deconvolutional analysis for the measurement of hepatic function in dogs with toxic-induced liver disease. *Vet Radiol Ultrasound.* Jul-Aug 1998;39(4):375-383.
143. Howman-Giles R, Moase A, Gaskin K, Uren R. Hepatobiliary scintigraphy in a pediatric population: determination of hepatic extraction fraction by deconvolution analysis. *J Nucl Med.* Feb 1993;34(2):214-221.
144. Juni JE, Reichle R. Measurement of hepatocellular function with deconvolutional analysis: application in the differential diagnosis of acute jaundice. *Radiology.* Oct 1990;177(1):171-175.
145. Juni JE, Thrall JH, Froelich JW, Wiggins RC, Campbell DA, Jr., Tuscan M. The appended curve technique for deconvolutional analysis--method and validation. *Eur J Nucl Med.* 1988;14(7-8):403-407.
146. Lieberman DA, Brown PH, Krishnamurthy GT. Improved scintigraphic assessment of severe cholestasis with the hepatic extraction fraction. *Dig Dis Sci.* Nov 1990;35(11):1385-1390.
147. Murase K, Tsuda T, Mochizuki T, Ikezoe J. Hepatic extraction fraction of hepatobiliary radiopharmaceuticals measured using spectral analysis. *Nucl Med Commun.* Nov 1999;20(11):1041-1045.
148. Tagge EP, Campbell DA, Jr., Reichle R, et al. Quantitative scintigraphy with deconvolutional analysis for the dynamic measurement of hepatic function. *J Surg Res.* Jun 1987;42(6):605-612.

149. Tolia V, Kottamasu SR, Tabassum D, Simpson P. The use of hepatocyte extraction fraction to evaluate neonatal cholestasis. *Clin Nucl Med.* Sep 1999;24(9):655-659.
150. Broome U, Olsson R, Lööf L, et al. Natural history and prognostic factors in 305 Swedish patients with primary sclerosing cholangitis. *Gut.* 1996;38(4):610-615.
151. Lin SP, Brown JJ. MR contrast agents: physical and pharmacologic basics. *J Magn Reson Imaging.* May 2007;25(5):884-899.
152. Shuter B, Tofts PS, Wang SC, Pope JM. The relaxivity of Gd-EOB-DTPA and Gd-DTPA in liver and kidney of the Wistar rat. *Magn Reson Imaging.* 1996;14(3):243-253.
153. Rohrer M, Bauer H, Mintorovitch J, Requardt M, Weinmann HJ. Comparison of magnetic properties of MRI contrast media solutions at different magnetic field strengths. *Invest Radiol.* Nov 2005;40(11):715-724.
154. Shuter B, Wang SC, Roche J, Briggs G, Pope JM. Relaxivity of Gd-EOB-DTPA in the normal and biliary obstructed guinea pig. *J Magn Reson Imaging.* Jul-Aug 1998;8(4):853-861.
155. Schuhmann-Giampieri G. Liver contrast media for magnetic resonance imaging. Interrelations between pharmacokinetics and imaging. *Invest Radiol.* Aug 1993;28(8):753-761.
156. Hamm B, Staks T, Muhler A, et al. Phase I clinical evaluation of Gd-EOB-DTPA as a hepatobiliary MR contrast agent: safety, pharmacokinetics, and MR imaging. *Radiology.* Jun 1995;195(3):785-792.
157. Bellin MF, Webb JA, Van Der Molen AJ, Thomsen HS, Morcos SK. Safety of MR liver specific contrast media. *Eur Radiol.* Aug 2005;15(8):1607-1614.
158. Clement O, Muhler A, Vexler V, Berthezene Y, Brasch RC. Gadolinium-ethoxybenzyl-DTPA, a new liver-specific magnetic resonance contrast agent. Kinetic and enhancement patterns in normal and cholestatic rats. *Invest Radiol.* Aug 1992;27(8):612-619.
159. Schuhmann-Giampieri G, Schmitt-Willich H, Press WR, Negishi C, Weinmann HJ, Speck U. Preclinical evaluation of Gd-EOB-DTPA as a contrast agent in MR imaging of the hepatobiliary system. *Radiology.* Apr 1992;183(1):59-64.
160. Leonhardt M, Keiser M, Oswald S, et al. Hepatic uptake of the magnetic resonance imaging contrast agent Gd-EOB-DTPA: role of human organic anion transporters. *Drug Metab Dispos.* Jul 2010;38(7):1024-1028.
161. van Montfoort JE, Stieger B, Meijer DK, Weinmann HJ, Meier PJ, Fattinger KE. Hepatic uptake of the magnetic resonance imaging contrast agent gadoxetate by the organic anion transporting polypeptide Oatp1. *J Pharmacol Exp Ther.* Jul 1999;290(1):153-157.
162. Kitao A, Zen Y, Matsui O, et al. Hepatocellular carcinoma: signal intensity at gadoxetic acid-enhanced MR Imaging--correlation with molecular transporters and histopathologic features. *Radiology.* Sep 2010;256(3):817-826.
163. Narita M, Hatano E, Arizono S, et al. Expression of OATP1B3 determines uptake of Gd-EOB-DTPA in hepatocellular carcinoma. *J Gastroenterol.* 2009;44(7):793-798.
164. Tsuboyama T, Onishi H, Kim T, et al. Hepatocellular carcinoma: hepatocyte-selective enhancement at gadoxetic acid-enhanced MR imaging--correlation with expression of sinusoidal and canalicular transporters and bile accumulation. *Radiology.* Jun 2010;255(3):824-833.
165. Schuhmann-Giampieri G, Schmitt-Willich H, Frenzel T, Schitt-Willich H. Biliary excretion and pharmacokinetics of a gadolinium chelate used as a liver-

specific contrast agent for magnetic resonance imaging in the rat. *J Pharm Sci.* Aug 1993;82(8):799-803.
166. Pascolo L, Petrovic S, Cupelli F, et al. Abc protein transport of MRI contrast agents in canalicular rat liver plasma vesicles and yeast vacuoles. *Biochem Biophys Res Commun.* Mar 23 2001;282(1):60-66.
167. Tamada T, Ito K, Sone T, Kanki A, Sato T, Higashi H. Gd-EOB-DTPA enhanced MR imaging: Evaluation of biliary and renal excretion in normal and cirrhotic livers. *Eur J Radiol.* Sep 23 2010.
168. Halavaara J, Breuer J, Ayuso C, et al. Liver tumor characterization: comparison between liver-specific gadoxetic acid disodium-enhanced MRI and biphasic CT--a multicenter trial. *J Comput Assist Tomogr.* May-Jun 2006;30(3):345-354.
169. Hammerstingl R, Huppertz A, Breuer J, et al. Diagnostic efficacy of gadoxetic acid (Primovist)-enhanced MRI and spiral CT for a therapeutic strategy: comparison with intraoperative and histopathologic findings in focal liver lesions. *Eur Radiol.* Mar 2008;18(3):457-467.
170. Huppertz A, Balzer T, Blakeborough A, et al. Improved detection of focal liver lesions at MR imaging: multicenter comparison of gadoxetic acid-enhanced MR images with intraoperative findings. *Radiology.* Jan 2004;230(1):266-275.
171. Raman SS, Leary C, Bluemke DA, et al. Improved characterization of focal liver lesions with liver-specific gadoxetic acid disodium-enhanced magnetic resonance imaging: a multicenter phase 3 clinical trial. *J Comput Assist Tomogr.* Mar-Apr 2010;34(2):163-172.
172. Shimada K, Isoda H, Hirokawa Y, Arizono S, Shibata T, Togashi K. Comparison of gadolinium-EOB-DTPA-enhanced and diffusion-weighted liver MRI for detection of small hepatic metastases. *Eur Radiol.* Jun 20 2010.
173. Zech CJ, Herrmann KA, Reiser MF, Schoenberg SO. MR imaging in patients with suspected liver metastases: value of liver-specific contrast agent Gd-EOB-DTPA. *Magn Reson Med Sci.* 2007;6(1):43-52.
174. Dahlström N, Persson A, Albiin N, Smedby Ö, Brismar TB. Contrast-enhanced magnetic resonance cholangiography with Gd-BOPTA and Gd-EOB-DTPA in healthy subjects. *Acta Radiol.* May 2007;48(4):362-368.
175. Seale MK, Catalano OA, Saini S, Hahn PF, Sahani DV. Hepatobiliary-specific MR contrast agents: role in imaging the liver and biliary tree. *Radiographics.* Oct 2009;29(6):1725-1748.
176. Lee NK, Kim S, Lee JW, et al. Biliary MR imaging with Gd-EOB-DTPA and its clinical applications. *Radiographics.* Oct 2009;29(6):1707-1724.
177. Schmitz SA, Muhler A, Wagner S, Wolf KJ. Functional hepatobiliary imaging with gadolinium-EOB-DTPA. A comparison of magnetic resonance imaging and 153gadolinium-EOB-DTPA scintigraphy in rats. *Invest Radiol.* Mar 1996;31(3):154-160.
178. Kim T, Murakami T, Hasuike Y, et al. Experimental hepatic dysfunction: evaluation by MRI with Gd-EOB-DTPA. *J Magn Reson Imaging.* Jul-Aug 1997;7(4):683-688.
179. Shimizu J, Dono K, Gotoh M, et al. Evaluation of regional liver function by gadolinium-EOB-DTPA-enhanced MR imaging. *Dig Dis Sci.* Jul 1999;44(7):1330-1337.
180. Ryeom HK, Kim SH, Kim JY, et al. Quantitative evaluation of liver function with MRI Using Gd-EOB-DTPA. *Korean J Radiol.* Oct-Dec 2004;5(4):231-239.
181. Tsuda N, Okada M, Murakami T. Potential of gadolinium-ethoxybenzyl-diethylenetriamine pentaacetic acid (Gd-EOB-DTPA) for differential diagnosis

of nonalcoholic steatohepatitis and fatty liver in rats using magnetic resonance imaging. *Invest Radiol.* Apr 2007;42(4):242-247.

182. Tsuda N, Okada M, Murakami T. New proposal for the staging of nonalcoholic steatohepatitis: Evaluation of liver fibrosis on Gd-EOB-DTPA-enhanced MRI. *Eur J Radiol.* Nov 19 2008.

183. Tschirch FT, Struwe A, Petrowsky H, Kakales I, Marincek B, Weishaupt D. Contrast-enhanced MR cholangiography with Gd-EOB-DTPA in patients with liver cirrhosis: visualization of the biliary ducts in comparison with patients with normal liver parenchyma. *Eur Radiol.* Aug 2008;18(8):1577-1586.

184. Motosugi U, Ichikawa T, Sou H, et al. Liver parenchymal enhancement of hepatocyte-phase images in Gd-EOB-DTPA-enhanced MR imaging: which biological markers of the liver function affect the enhancement? *J Magn Reson Imaging.* Nov 2009;30(5):1042-1046.

185. Takao H, Akai H, Tajima T, et al. MR imaging of the biliary tract with Gd-EOB-DTPA: Effect of liver function on signal intensity. *Eur J Radiol.* Aug 31 2009.

186. Tajima T, Takao H, Akai H, et al. Relationship between liver function and liver signal intensity in hepatobiliary phase of gadolinium ethoxybenzyl diethylenetriamine pentaacetic acid-enhanced magnetic resonance imaging. *J Comput Assist Tomogr.* May-Jun 2010;34(3):362-366.

187. Katsube T, Okada M, Kumano S, et al. Estimation of Liver Function Using T1 Mapping on Gd-EOB-DTPA-Enhanced Magnetic Resonance Imaging. *Invest Radiol.* Apr 2011;46(4):277-283.

188. Nishie A, Ushijima Y, Tajima T, et al. Quantitative analysis of liver function using superparamagnetic iron oxide- and Gd-EOB-DTPA-enhanced MRI: Comparison with Technetium-99m galactosyl serum albumin scintigraphy. *Eur J Radiol.* Mar 22 2011.

189. Fulcher AS, Turner MA, Franklin KJ, et al. Primary sclerosing cholangitis: evaluation with MR cholangiography-a case-control study. *Radiology.* Apr 2000;215(1):71-80.

190. Berstad AE, Aabakken L, Smith HJ, Aasen S, Boberg KM, Schrumpf E. Diagnostic accuracy of magnetic resonance and endoscopic retrograde cholangiography in primary sclerosing cholangitis. *Clin Gastroenterol Hepatol.* Apr 2006;4(4):514-520.

191. Davenport R. The derivation of the gamma-variate relationship for tracer dilution curves. *J Nucl Med.* Oct 1983;24(10):945-948.

192. Murakami T, Kim T, Gotoh M, et al. Experimental hepatic dysfunction: evaluation by MR imaging with Gd-EOB-DTPA. *Acad Radiol.* Apr 1998;5 Suppl 1:S80-82.

193. Ni Y, Marchal G, Lukito G, Yu J, Muhler A, Baert AL. MR imaging evaluation of liver enhancement by Gd-EOB-DTPA in selective and total bile duct obstruction in rats: correlation with serologic, microcholangiographic, and histologic findings. *Radiology.* Mar 1994;190(3):753-758.

194. Ostergaard L, Weisskoff RM, Chesler DA, Gyldensted C, Rosen BR. High resolution measurement of cerebral blood flow using intravascular tracer bolus passages. Part I: Mathematical approach and statistical analysis. *Magn Reson Med.* Nov 1996;36(5):715-725.

195. Wirestam R, Andersson L, Ostergaard L, et al. Assessment of regional cerebral blood flow by dynamic susceptibility contrast MRI using different deconvolution techniques. *Magn Reson Med.* May 2000;43(5):691-700.

196. Murase K, Yamazaki Y, Miyazaki S. Deconvolution analysis of dynamic contrast-enhanced data based on singular value decomposition optimized by generalized cross validation. *Magn Reson Med Sci.* 2004;3(4):165-175.
197. Ostergaard L. Principles of cerebral perfusion imaging by bolus tracking. *J Magn Reson Imaging.* Dec 2005;22(6):710-717.
198. Pandharipande PV, Krinsky GA, Rusinek H, Lee VS. Perfusion imaging of the liver: current challenges and future goals. *Radiology.* Mar 2005;234(3):661-673.
199. Jacobsson H, Hellström PM, Kogner P, Larsson SA. Different concentrations of I-123 MIBG and In-111 pentetreotide in the two main liver lobes in children: persisting regional functional differences after birth? *Clin Nucl Med.* Jan 2007;32(1):24-28.
200. Jacobsson H, Jonas E, Hellström PM, Larsson SA. Different concentrations of various radiopharmaceuticals in the two main liver lobes: a preliminary study in clinical patients. *J Gastroenterol.* Jul 2005;40(7):733-738.
201. Arun J, Jhala N, Lazenby AJ, Clements R, Abrams GA. Influence of liver biopsy heterogeneity and diagnosis of nonalcoholic steatohepatitis in subjects undergoing gastric bypass. *Obes Surg.* Feb 2007;17(2):155-161.
202. Larson SP, Bowers SP, Palekar NA, Ward JA, Pulcini JP, Harrison SA. Histopathologic variability between the right and left lobes of the liver in morbidly obese patients undergoing Roux-en-Y bypass. *Clin Gastroenterol Hepatol.* Nov 2007;5(11):1329-1332.
203. Merriman RB, Ferrell LD, Patti MG, et al. Correlation of paired liver biopsies in morbidly obese patients with suspected nonalcoholic fatty liver disease. *Hepatology.* Oct 2006;44(4):874-880.
204. Vuppalanchi R, Unalp A, Van Natta ML, et al. Effects of liver biopsy sample length and number of readings on sampling variability in nonalcoholic Fatty liver disease. *Clin Gastroenterol Hepatol.* Apr 2009;7(4):481-486.
205. Bennink RJ, Dinant S, Erdogan D, et al. Preoperative assessment of postoperative remnant liver function using hepatobiliary scintigraphy. *J Nucl Med.* Jun 2004;45(6):965-971.
206. Imaeda T, Kanematsu M, Asada S, Seki M, Doi H, Saji S. Utility of Tc-99m GSA SPECT imaging in estimation of functional volume of liver segments in health and liver diseases. *Clin Nucl Med.* Apr 1995;20(4):322-328.
207. Matsuzaki S, Onda M, Tajiri T, Kim DY. Hepatic lobar differences in progression of chronic liver disease: correlation of asialoglycoprotein scintigraphy and hepatic functional reserve. *Hepatology.* Apr 1997;25(4):828-832.
208. Mitsumori A, Nagaya I, Kimoto S, et al. Preoperative evaluation of hepatic functional reserve following hepatectomy by technetium-99m galactosyl human serum albumin liver scintigraphy and computed tomography. *Eur J Nucl Med.* Oct 1998;25(10):1377-1382.
209. Rowland M, Tozer T. *Clinical pharmacokinetics, Concepts and Applications*. 3rd ed ed. Philadelphia PA: Lea&Febiger; 1995.
210. Ringe KI, Husarik DB, Gupta RT, Boll DT, Merkle EM. Hepatobiliary transit times of gadoxetate disodium (Primovist((R))) for protocol optimization of comprehensive MR imaging of the biliary system-What is normal? *Eur J Radiol.* Mar 26 2010.
211. Selle D, Preim B, Schenk A, Peitgen HO. Analysis of vasculature for liver surgical planning. *IEEE Trans Med Imaging.* Nov 2002;21(11):1344-1357.

212. van Laarhoven HW, Rijpkema M, Punt CJ, et al. Method for quantitation of dynamic MRI contrast agent uptake in colorectal liver metastases. *J Magn Reson Imaging.* Sep 2003;18(3):315-320.
213. Pandey SK, Bhattacharya S, Mishra RN, Shukla VK. Anatomical variations of the splenic artery and its clinical implications. *Clin Anat.* Sep 2004;17(6):497-502.
214. Tadamura E, Hatabu H, Li W, Prasad PV, Edelman RR. Effect of oxygen inhalation on relaxation times in various tissues. *J Magn Reson Imaging.* Jan-Feb 1997;7(1):220-225.
215. de Bazelaire CM, Duhamel GD, Rofsky NM, Alsop DC. MR imaging relaxation times of abdominal and pelvic tissues measured in vivo at 3.0 T: preliminary results. *Radiology.* Mar 2004;230(3):652-659.
216. Rusinek H, Lee VS, Johnson G. Optimal dose of Gd-DTPA in dynamic MR studies. *Magn Reson Med.* Aug 2001;46(2):312-316.
217. Sourbron S, Luypaert R, Van Schuerbeek P, Dujardin M, Stadnik T. Choice of the regularization parameter for perfusion quantification with MRI. *Phys Med Biol.* Jul 21 2004;49(14):3307-3324.
218. Reimer P, Schneider G, Schima W. Hepatobiliary contrast agents for contrast-enhanced MRI of the liver: properties, clinical development and applications. *Eur Radiol.* Apr 2004;14(4):559-578.
219. Nakanuma Y, Zen Y, Harada K, et al. Application of a new histological staging and grading system for primary biliary cirrhosis to liver biopsy specimens: Interobserver agreement. *Pathol Int.* Mar 2010;60(3):167-174.
220. Bennett JJ, Blumgart LH. Assessment of hepatic reserve prior to hepatic resection. *J Hepatobiliary Pancreat Surg.* 2005;12(1):10-15.
221. Pawlik TM, Olino K, Gleisner AL, Torbenson M, Schulick R, Choti MA. Preoperative chemotherapy for colorectal liver metastases: impact on hepatic histology and postoperative outcome. *J Gastrointest Surg.* Jul 2007;11(7):860-868.
222. Vauthey JN, Pawlik TM, Ribero D, et al. Chemotherapy regimen predicts steatohepatitis and an increase in 90-day mortality after surgery for hepatic colorectal metastases. *J Clin Oncol.* May 1 2006;24(13):2065-2072.
223. Pessaux P, Chenard MP, Bachellier P, Jaeck D. Consequences of chemotherapy on resection of colorectal liver metastases. *J Visc Surg.* Aug 2010;147(4):e193-201.
224. Wieckowska A, McCullough AJ, Feldstein AE. Noninvasive diagnosis and monitoring of nonalcoholic steatohepatitis: present and future. *Hepatology.* Aug 2007;46(2):582-589.
225. Zech CJ, Grazioli L, Jonas E, et al. Health-economic evaluation of three imaging strategies in patients with suspected colorectal liver metastases: Gd-EOB-DTPA-enhanced MRI vs. extracellular contrast media-enhanced MRI and 3-phase MDCT in Germany, Italy and Sweden. *Eur Radiol.* Jun 2009;19 Suppl 3:S753-763.